DESIGN OF LOSSY ANTENNAS - OPTICAL CRESCENT NANOANTENNAS AND RADIO FREQUENCY IMPLANTABLE ANTENNAS

by

Miguel Rodriguez

A dissertation submitted to the faculty of
The University of Utah
in partial fulfillment of the requirements for the degree of

Doctor of Philosophy

Department of Electrical and Computer Engineering

The University of Utah

May 2015

The University of Utah Graduate School

STATEMENT OF DISSERTATION APPROVAL

The dissertation of **Miguel A Rodriguez**

has been approved by the following supervisory committee members:

Cynthia M. Furse	, Chair	**01/07/2015** Date Approved
Steven Blair	, Co-Chair	**01/07/2015** Date Approved
Jennifer Shumaker-Parry	, Adviser	**01/07/2015** Date Approved
Om P. Gandhi	, Member	**01/07/2015** Date Approved
David Schurig	, Member	**01/07/2015** Date Approved

and by **Gianluca Lazzi** , Chair of

the Department of **Electrical and Computer Engineering**

and by David B. Kieda, Dean of The Graduate School.

ABSTRACT

The invention of antennas has revolutionized the world by enabling fast communications over long distances. Since their invention in the 1800s, antennas have been extensively studied at RF and microwave frequencies. The high conductivity of metals coupled with operation in a relatively loss-free environment has fueled the rapid development of antennas designed to operate at particular frequency ranges. Evolution of science and technology has now led to the study of lossy antennas. The ability to create nanometer scale structures has allowed for the creation of antennas for operation at very high (optical) frequencies. At these frequencies, metals are no longer excellent conductors, and their lossiness must be considered in order to effectively design and create resonant antennas. In the RF, the fast development of applications for antennas has led to an artificial allocation of frequency bands to prevent interference. In the nanoworld, electromagnetic spectrum allocation is more natural and is dictated by the particular application. In both cases, the ability to apply antennas relies upon control of their resonances. Lossy materials contribute an additional variable to the creation and control of resonant structures.

The purpose of this research is to study the effect of material losses in RF and optical antennas. The investigation is done via the study of implantable spiral antennas at RF frequencies and crescent nanoantennas at optical wavelengths.

TABLE OF CONTENTS

ABSTRACT……iii

ACKNOWLEDGMENTS……vi

Chapters

1 INTRODUCTION 1

1.1 Background 1
1.2 Contributions 3

2 REVIEW OF LOSSY MATERIALS FOR ANTENNAS 9

2.1 Propagation and Decay of Fields 9
2.2 Radiating Element 10
2.3 Dielectric Elements 14

3 AN IMPLANTABLE ANTENNA DESIGNED FOR EASE OF MANUFACTURING 20

3.1 Abstract 20
3.2 Introduction 20
3.3 Design for Manufacturability 22
3.3.1 Ground Plane 22
3.3.2 Superstrate 23
3.3.3 Radiating Spiral 23
3.3.4 Feed 23
3.3.5 Ground Pin 24
3.3.6 Substrate 24
3.4 Simulation and Design 24
3.4.1 Effect of Spiral Shape 25
3.4.2 Effect of Shorting Tab versus Shorting Pin 26
3.4.3 Effect of Substrate and Superstrate Shape 26
3.4.4 Effect of Material Properties 27
3.5 Measurements 28
3.6 Conclusion 29

4 REVIEW OF CRESCENT ANTENNAS 39

4.1 Crescent Types 39
4.2 RF versus Plamonic Antennas 42
4.3 Materials 44
4.4 Investigations on Crescent Antennas 46
4.4.1 Ultraviolet 46
4.4.2 Visible 47
4.4.3 Near-IR 50
4.4.4 Mid-IR 57
4.4.5 Microwaves 58

5 SCALING THE RESPONSE OF NANOCRESCENT ANTENNAS INTO THE ULTRAVIOLET[1] 78

5.1 Abstract 78
5.2 Introduction 79
5.3 Simulation Model 80
5.4 Results 83
5.4.1 Scaling with Crescent Diameter 84
5.4.2 Scaling with Deposition Angle 85
5.4.3 Scaling with Crescent Height 86
5.4.4 Effect of Native Oxide Shell 86
5.5 Conclusions 89

6 CONCLUSION 100

6.1 Contributions 101
6.1.1 Implatable Antenna Designed for Ease of Manufacture 101
6.1.2 Scaling the Response of Crescent Nanoantennas into the UV 101
6.1.3 Polarization Anisotropy of Crescent Nanoantennas 102
6.1.4 Plasmonic Gold and Silver Nanocrescent Arrays 103
6.1.5 Mid-IR LSPR of Gold and Silver Nanocrescents 103

REFERENCES 104

ACKNOWLEDGMENTS

The work reported in this document was possible thanks to the help and contribution of various people and institutions. I gained professionally and personally and so would like to acknowledge and thank them for their support.

I would first like to thank my advisor, Dr. Cynthia Furse. The constant guidance, help and encouragement she offered very much helped ease the weight of the problems I encountered and greatly impacted my professional growth.

I would also like to thank my advisor, Dr. Steve Blair, whose advice and guidance helped me maneuver and grow in the field of optics.

Thanks also to my committee members, Dr. Jennifer Shumaker-Parry, Dr. Om Gandhi, and Dr. David Schurig, whose advice and constructive criticism helped me better define and polish my work, and to my friends whose encounters enriched my work and my life.

Finally, I would like to thank the Wayne-Brown fellowship, IGERT, and MRSEC, whose generous contributions supported and helped me in completing the work.

CHAPTER 1

INTRODUCTION

1.1 Background

Investigation of radio antennas dates back to 1888 with the work of Heinrich Hertz in which he sought to prove the existence of electromagnetic waves predicted by Maxwell. His experiments consisted of dipole antennas placed at the focal point of parabolic reflectors for both transmitting and receiving [1]. Successive experiments by Guglielmo Marconi in 1895 demonstrated wireless transmission of antennas up to a kilometer away when placing a plate on the ground and a second plate at a high altitude [2]. Since then, antennas for communications have been widely studied, and many antenna geometries have been developed. Optical antennas, on the other hand, date back to 1985 when John Wessel referred to particles acting as antennas that receive incoming electromagnetic fields. In contrast to RF antennas, optical antennas were invented for microscopy in order to replace conventional lenses to focus external laser radiation to dimensions smaller than the diffraction limit. Similar to RF antennas, optical antennas can be defined as devices designed to efficiently convert free-propagating optical radiation to localized energy and vice versa [2]. Localization of optical radiation in this manner has led to a plethora of possible applications for these antennas. In addition to telecommunication applications, optical antennas can be used in spectroscopy, photovoltaics, biological and chemical

sensing, and thermal and many other applications. In spectroscopy applications, radiation from molecules efficiently couples to nanoantennas that can be easily detected. Since molecules have particular spectral signatures, they can be identified [3]. Biological or chemical sensing works on the principle that the resonance of an antenna is sensitive to its environment. A molecule placed in close vicinity to an antenna will therefore shift its resonant wavelength resulting in its detection [4]. Antennas in photovoltaic applications can be used to efficiently receive free-space radiation. This radiation can then be coupled to solar cells for energy conversion [5],[6]. In thermal applications, the lossiness of optical antennas is exploited by converting electromagnetic radiation to thermal energy. This energy can then be used in medical therapies to destroy cancer tumors for instance [7].

In the RF regime, and for most practical applications, the concern with material losses is marginal. In this frequency range, metals are excellent conductors resulting in low penetration depth of fields and consequently low losses [8]. There are, however, applications in which antennas operate in lossy environments, such as for instance the human body or the ionosphere surrounding the planet. In these applications materials play an important role in isolating and optimizing an antenna for operation in such environments. In the optical regime, material losses are of common concern, resulting from the increased penetration depth of fields caused by decreased conductivity of metals at these frequencies [9].

The effect of material losses in RF and optical antennas is considered in this dissertation. This is accomplished by means of two types of antennas: implantable spiral antennas in the RF and crescent nanoantennas at optical wavelengths [10], [11].

1.2 Contributions

The contributions of this research pertain to creating resonant antennas when lossy materials are considered. The investigations show that resonant structures can be created over different frequency ranges by properly considering materials' properties. The contributions of this dissertation include **1)** creating an implantable spiral antenna using biocompatible materials (discussed in Chapter 3, and presented at [12]), **2)** showing the feasibility of aluminum nanocrescent antennas for application in the ultraviolet (discussed in Chapter 5 and section 4.4.2.2, published in [10], and presented at [13]–[15]), **3)** controlling resonant modes by suppressing them as desired by means of rotating the polarization of the source (discussed in section 4.4.3.3 and published in [11]), **4)** demonstrating the similarity in response between arrays of crescent antennas when compared to single isolated antennas (discussed in section 4.4.3.4), and **5)** demonstrating resonant properties of gold and silver nanocrescent antennas in the mid-IR (discussed in section 4.4.4.1).

The first contribution pertains to manufacturing RF antennas with nonconventional RF materials (Chapter 3). The feasibility of using spiral antennas in implantable applications was first demonstrated in [16] with antennas manufactured using typical RF materials. The investigation included a parametric evaluation to study the effect of changing variable parameters on antenna performance. The antenna parameters considered in the study included shape, length, and size of radiating element, location of feed and ground, substrate and superstrate materials, and their thickness. In this study, we expand on that investigation by considering the effects of biocompatible materials and fulfilling actual requirements needed for their implementation. The complete study from design to testing

was done using atypical biocompatible materials for the components of the antenna. The results demonstrate a design that is resonant and biocompatible and meets stringent manufacturing requirements for implementation. Testing of these antennas was simplified by submersing the antenna in saline solution to simulate the lossy environment of the body. The effect of changing the operating environment can be determined through simulation. The results of this investigation inch closer to possible implementation.

In regard to optical antennas, planar gold and silver crescent antennas have been widely studied in the near-infrared. Investigations on this structure initially started with the introduction of nanosphere template lithography (NTL) as a new fabrication method for fabricating crescent nanostructures. Using this method a high degree of control on the physical features of the antenna, including its diameter, height, width, and separation between the tips, was demonstrated [17]. This was followed by numerous investigations in experimental, theoretical, and application aspects of the structure. The research contributions reported in this document focus on characterization of aluminum, silver, and gold crescent nanoantennas, demonstrating their near- and far-field response and tunability over various wavelength ranges. As is typical of optical antennas, the ability to control their resonance leads to many possible applications that are most times wavelength dependent.

The first contribution in optical antennas addresses the feasibility of creating crescent nanoantennas that are resonant in the ultraviolet (UV) wavelength range (sections 4.4.1.1, 4.4.2.2, and Chapter 5). This wavelength range is relatively untouched in research activities due to the poor performance in metals and difficulty of obtaining resonance in the UV. The study shows that the key to attaining resonance in this wavelength range is

the materials used for the antenna. Most metals typically used in fabrication of nanoantennas are very lossy in this wavelength range and hinder resonance. Aluminum, however, improves at these shorter wavelengths. The results show that although it is difficult to shift dipole resonances into the UV using antenna dimensions that are easily manufacturable, a wealth of higher order resonant modes are observed for easily realizable structures. Although the emphasis of this activity was in the UV, strong dipole resonances were observed in the visible, which could enable implementation of these structures to applications such as improving efficiency of photovoltaics.

The next contribution relates to the ability to induce or suppress resonance modes of gold and silver crescent antennas at infrared wavelengths (section 4.4.3.3). The peculiar geometry of crescent antennas enables two distinct dipole resonances. A longer wavelength resonance is induced when the source polarization is oriented along the longest dimension of the crescent and a second resonance at a shorter wavelength is induced for a source polarized along the shortest dimension of the structure. The strength of each resonance and accompanying near-fields can be controlled in degrees from its highest intensity to complete suppression by merely rotating the polarization of the source. This is a valuable find that could help in single molecule detection.

The fourth contribution is in the infrared and relates to maximizing the use of crescent antennas by creating closed-packed arrays (section 4.4.3.4). This increases the usable area by increasing the density of antennas and can result in improvement in applications such as sensing by enhancing the probability of enhancing signals.

The last contribution pertains to the creation of resonant structures in the mid-infrared. In wavelength range the electrical properties of metals transition from being good

conductors to the more lossy properties encountered at optical frequencies. Similarly to the ultraviolet, this region is relatively untouched due to the difficulty of creating resonant structures. The study shows that crescent antennas are very good candidates for resonance in this range because of the great degree of control that can be independently exerted on the different features of the antennas. The benefits of these structures in the mid-IR relate to improving thermal systems in the IR and extending the use of spectroscopy techniques from the near-IR into the mid-IR.

In order to illustrate the importance of nanoantennas, a possible application is described here. A possible application of item aluminum crescent antennas in the ultraviolet is in the detection of intrinsic fluorescence of biomolecules for biomedical research and diagnosis. Fluorescence is widely used in medical applications such as DNA analysis, clinical chemistry, drug discovery, and biochemical research. The usefulness of this method lies in the fact that a fluorophore emits at a longer wavelength that the wavelength used to excite it, thus reducing interference from background. Currently fluorescence detection is almost always accomplished through the use of extrinsic fluorophores. The additional step of tagging a molecule with a fluorophore introduces complexity, inefficiency, and cost to the process, especially in cases when hundreds of molecules need to be tested. Providing a self-contained platform, where the sample under test does not need special preparation before testing, will therefore prove very beneficial for medical and biological applications.

Biomolecules such as peptides and proteins contain three intrinsic fluorophores: phenylalanine, tyrosine, and tryptophan. These aromatics absorb at wavelengths between 220 nm and 280 nm and emit at wavelengths between 320 nm and 370 nm. Their

fluorescence quantum efficiency is very low, however. The use of antennas can be very useful in exciting the fluorophore more efficiently, thus improving its fluorescence. This can be achieved by exciting an antenna with a UV laser source. Resonance of the antenna will then result in field enhancement in some volume around the structure, coupling this energy to a molecule, and enhancing its fluorescence. It has been reported that the intrinsic fluorescence of proteins is enhanced in the proximity of silver and aluminum nanostructures. A further advantage of using nanoantennas to improve intrinsic fluorescence is that by not using labels, these molecules can be studied without affecting their binding properties. This is useful in determining a molecule's natural behavior. The motivation of extending the response of optical antennas into the UV range stems from the fact that biomolecules naturally fluoresce at UV wavelengths. This fluorescence and hence the presence of the molecules can be detected if they are stimulated with UV radiation as depicted in Figure 1.1. A fluorescent label therefore will not be needed as in current detection systems.

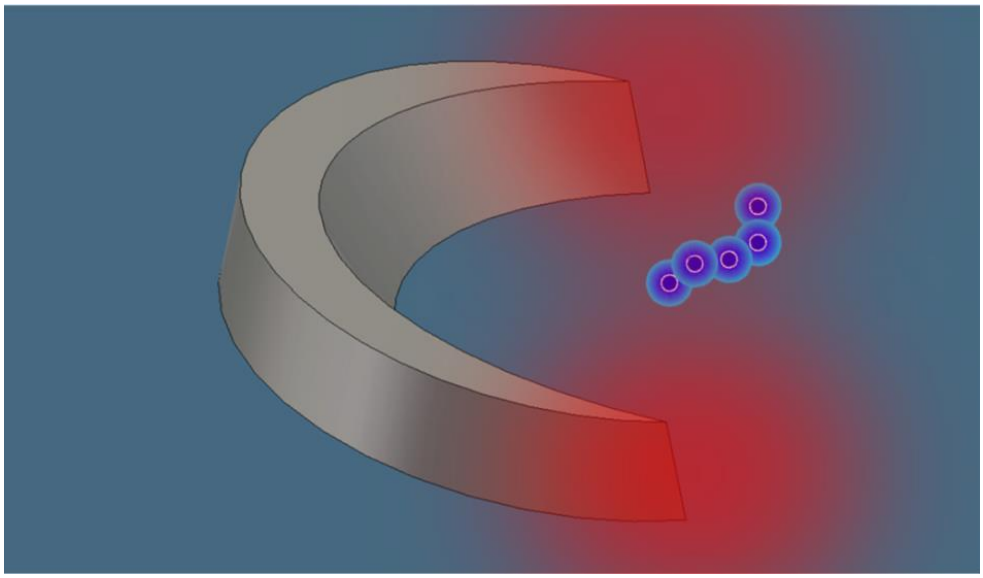

Figure 1.1. Antenna coupling energy to enhance fluorescence of molecule.

CHAPTER 2

REVIEW OF LOSSY MATERIALS FOR ANTENNAS

2.1 Propagation and Decay of Fields

Material properties play an important role in the performance of antennas. Depending on the type of antenna, its composition may include a combination of metals and dielectrics arranged in a particular order. Metals are typically used as radiating elements, while dielectrics are typically used to isolate or hold the metal components.

Materials are characterized by a set of equivalent parameters that describe the behavior of fields within it. In optics, the complex index of refraction, n = n' + in", is used for this purpose. The real part, n', is associated with the velocity of the wave, and the imaginary part, n", describes the decay of fields as they enter the medium [18]. In one dimension, for instance, the behavior of fields in a semi-infinite slab of matter can be described by equation 2.1.

$$E = Eo e^{inz} = Eo e^{i(n' + in")z} \qquad (2.1)$$

In radio frequency (RF) applications, the complex propagation constant, $\gamma = \alpha + j\beta$, serves the same purpose. The attenuation constant, α, describes the decay of fields entering a material, the propagation constant, β, describes the phase of the wave and a one dimensional expression describing the behavior of fields in semi-infinite media is given by equation 2.2 [19].

$$E = E_o e^{-\gamma z} = E_o e^{(-\alpha - j\beta)z} \quad (2.2)$$

The attenuation and propagation constants can be further expressed in terms of the complex dielectric constant and conductivity, $\varepsilon = \varepsilon' - j\varepsilon'' = \varepsilon' - j\frac{\sigma}{\omega}$, resulting in equations 2.3 and 2.4 [19][20].

$$\alpha = \omega \sqrt{\frac{\mu\varepsilon'}{2}\left[\sqrt{1 + \left(\frac{\varepsilon''}{\varepsilon'}\right)^2} - 1\right]} \quad (2.3)$$

$$\beta = \omega \sqrt{\frac{\mu\varepsilon'}{2}\left[\sqrt{1 + \left(\frac{\varepsilon''}{\varepsilon'}\right)^2} + 1\right]} \quad (2.4)$$

These expressions give further insight into the behavior of fields and allow for materials to be categorized as lossless, low loss, and good conductors. Table 2.1 shows the simplified form for the attenuation and phase constant of these special cases.

2.2 Radiating Element

Metals are excellent candidates for the radiating element of antennas at RF frequencies due to their high conductivity over this frequency range. The conductivity, σ, of metals up to infrared frequencies can be described by the Drude model for electrical conductivity as given in equation 2.5.

$$\sigma = \frac{\sigma_o}{1 + j\omega\tau} \quad (2.5)$$

where σ_o is the low-frequency conductivity, ω is the operating frequency, and τ is the relaxation time. Table 2.2 lists various characteristic parameters of metals including low-frequency conductivity [21], relaxation time [22], [23], and plasma frequency [22]. It can be observed from equation 2.5 and Table 2.2 that metals are excellent conductors at RF frequencies and although they are lossy, they are ideal for the radiating element of

antennas. The reason for this is that fields decay very fast within the metal and losses are kept low because of the small volume over which they occur [9]. A measure of the decay of fields in media is the skin depth, δ. It is defined as the penetration distance at which the magnitude of the field decays to e^{-1} of its initial value. Given the exponential decay of fields as expressed in equation 2.2, the skin depth is given by $\delta = \frac{1}{\alpha}$. For metals at RF frequencies, this expression reduces to $\delta = \sqrt{\frac{2}{\omega\mu\sigma}}$ [21]. It can be observed from this expression that the high conductivity of metals results in small skin depths compared to dimensions of antennas operating at these frequencies and thus comparably low losses. As the operating frequency increases towards optical frequencies, however, the conductivity of metals greatly decreases. Decreased conductivity results in increased penetration depth and, as a result, increased Ohmic losses. This effect is particularly detrimental in optics applications, where antennas are in the nano-/micrometer range, and the penetration depth is comparable with the dimensions of antennas. Figure 2.1 qualitatively illustrates the issue for an aluminum crescent 180 nm in diameter and 50 nm in height. The skin depth of aluminum at a wavelength of 620 nm is 13 nm [24]. The transparent volume in red shows the penetration depth of the fields into the crescent. From the figure it is readily obvious that the fields penetrate deep into the antenna for these small antennas.

Since the conductivity of all metals decreases at optical wavelengths, it is not a sufficient factor to determine the usefulness of a metal at a particular operating range. The real part of the dielectric function, ε', provides a second parameter to evaluate metals for optical applications. The permittivity, ε, of metals up to frequencies preceding interband transitions can be accurately described by the Drude model as given by

equation 2.6. This model accounts for free electrons moving within the metal lattice composed of the heavier atomic nuclei as illustrated in Figure 2.2.

$$\varepsilon = \varepsilon_o\left[\mathbf{1} - \frac{\omega_p^2}{\omega^2+\gamma^2} + \frac{\gamma}{\omega}\left(\frac{\omega_p^2}{\omega^2+\gamma^2}\right)\boldsymbol{i}\right] \quad (2.6)$$

In this expression, ω_p is defined as the plasma frequency of the electron gas and lies in the ultraviolet for typical plasmonic metals. γ is the damping constant associated with collisions between electrons and lattice atoms and is related to the relaxation time by $\gamma = 1/\tau$. ω is the operating frequency. The values for typical metals used in plasmonic antennas are listed in Table 2.2. It can be observed from this expression that when the operating frequency is much less than the plasma frequency ($\omega << \omega_p$), the real part of the dielectric function is negative. A negative permittivity is associated with reflectivity of the metal [25]. Also, the imaginary part of the dielectric function increases as the operating frequency decreases. Since the imaginary part is associated with conductivity of the metal, $\varepsilon'' = \sigma/\omega$ [19], the conductivity also increases as the frequency decreases. The increased conductivity results in decreased skin depth and thus decreased losses. These observations lead to the specification of a figure of merit to determine the usefulness of a metal at optical frequencies. In order to increase reflectivity, the negative of the real part of the permittivity, $-\varepsilon'$, is chosen as large as possible. Also, the imaginary part of the permittivity, ε'', is chosen to be as low as possible to decrease Ohmic losses. The figure of merit (FOM) is thus defined as the negative of the ratio of the real to the imaginary part of the dielectric function as shown in equation 2.7 [26].

$$\text{FOM} = \frac{-\varepsilon'}{\varepsilon''} \quad (2.7)$$

Although the Drude model describes the behavior of metals up to frequencies into the infrared, it fails to accurately describe the permittivity at wavelengths where interband

transitions occur. The reason it fails is because it assumes that only free electrons contribute to the dielectric function of the metal. Fields at higher frequencies, however, have more energy. These higher energy fields (i.e., shorter wavelengths) have enough energy to promote bound electrons from lower-lying electronic bands to the higher energy conduction band. Promotion of these electrons into higher energy levels is termed interband transitions. In contrast to free electrons described by the Drude model, these electrons are bound to a particular metal ion as symbolized in Figure 2.3 by a connecting spring. The contribution of these bound electrons to the dielectric function is given by the Lorentz model as expressed in equation 2.8. The additional term, ω_o, in this equation is the result of the attraction force of the positively charged metal ion and negatively charged electron. This force keeps the electron bound to a particular atom rather than allowing it to flow freely like conduction electrons. Note also that the variables in the Drude and Lorentz model have different values in general since the former represents free electrons while the latter represents bound electrons.

$$\varepsilon = 1 + \frac{\omega_p^2(\omega_o^2 - \omega^2)}{(\omega_o^2 - \omega^2)^2 + \gamma^2\omega^2} + \frac{\gamma\omega_p^2\omega}{(\omega_o^2 - \omega^2)^2 + \gamma^2\omega^2} i \qquad (2.8)$$

The dielectric function of metals is then the result of contributions from the Drude and Lorentz models (equation 2.9).

$$\varepsilon = \varepsilon_{\text{Drude}} + \varepsilon_{\text{Lorentz}} \qquad (2.9)$$

The interband transitions described by the Lorentz model result in increased losses [25]. This can be seen observing what happens within the metal as interband wavelengths are approached. The imaginary part of the Drude model predicts a decrease in conductivity as the frequency is increased and thus decreased of ohmic losses. At wavelengths where interband transitions occur, however, the imaginary part of the

Lorentz model contributes to the total imaginary part of the permittivity resulting in increased losses.

The figure of merit of typical metals used in plasmonic antennas is graphed in Figure 2.4. Since the figure of merit for silver and gold is large at wavelengths longer than ~600nm, these metals are suitable for applications in the infrared part of the spectrum. The figure of merit for aluminum improves as the wavelength decreases into the ultraviolet (UV). This metal is therefore useful for UV applications.

2.3 Dielectric Elements

Dielectric components make an important part of antennas. Depending on the application, dielectrics can serve multiple purposes, and their electrical properties are chosen accordingly. A common characteristic desired is that the dielectric be lossless ($\sigma = 0$). As observed from Table 2.1, this results in no attenuation (α) and only propagation (β) of the wave through the dielectric medium. In optical antenna applications, dielectric media are used as substrates to hold the antennas, and transmission-dependent measurements are used to characterize and use the antennas. This is illustrated via a typical measurement setup of optical antennas as shown in Figure 2.5 [27]. Measuring the response of an antenna requires the assembly (substrate and antennas) be illuminated by a light source. Illumination of the antennas results in three measured parameters that characterize the response of the antenna: scattering, absorption, and extinction. As the name implies, absorption corresponds to light that is absorbed by the assembly and scattering corresponds to light that is scattered in any direction other than that of the detector. Extinction is the sum of scattering and absorption and corresponds to light that

is not transmitted to the detector due to absorption or scattering by the sample. It is readily observed that the parameters of interest are based on transmission of light through the assembly. The substrate, therefore, needs to be transparent over the wavelength range of interest in order for the detector to gather light of resonant structures on top of the substrate. Depending on the operating wavelength range, several materials can be practically idealized with zero conductivity (e.g., glass or calcium fluoride).

In RF antenna applications, practical substrates are low-loss media. This media have the added advantage of reducing the size of antennas. This can be explained by evaluating the expression for the propagation constant in Table 2.1. The expression describing the relationship between wavelength and the propagation constant is $\beta = 2\pi f\sqrt{\mu\varepsilon_o\varepsilon_r} = \frac{2\pi}{\lambda}$. From this expression the effective wavelength observed within the dielectric medium is given by equation 2.10.

$$\lambda = \frac{\mathbf{1}}{\boldsymbol{f\sqrt{\mu\varepsilon_o\varepsilon_r}}} \qquad (2.10)$$

where f is the operating frequency, μ is the permeability of the material, ε_o is the permittivity of free space, and ε_r is the permittivity of the material. It is obvious from this equation that the effective wavelength can be decreased by choosing a dielectric with a high dielectric constant, ε_r. The size of an antenna can therefore be reduced by embedding the radiating element within a medium with relative permittivity higher than that of free space. This is illustrated in Figure 2.6 with an example. In Figure 2.6a, a free space wavelength of 2 m impinges on a dipole antenna. The required size of the antenna is half the wavelength or L = 1 m. Figure 2.6b shows the effect of embedding the antenna within a dielectric medium. The effective wavelength within the material is inversely proportional to the square root of the dielectric constant of the medium as given in

equation 2.10. Using a dielectric constant of $\varepsilon_r = 4$, for example, results in the size of the required antenna to be reduced by half.

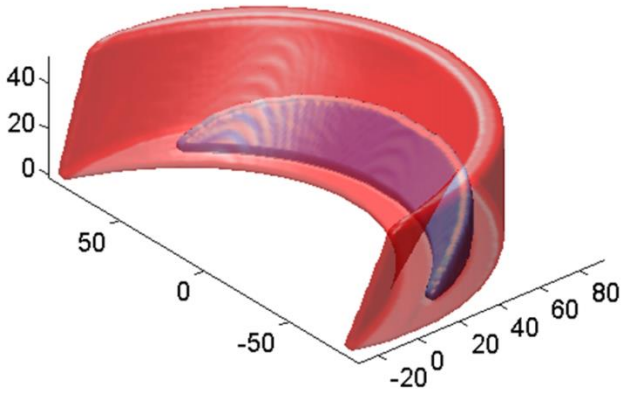

Figure 2.1: Penetration depth of fields into an aluminum nanocrescent antenna with 180 nm diameter and 50 nm height is shown as the transparent volume in red.

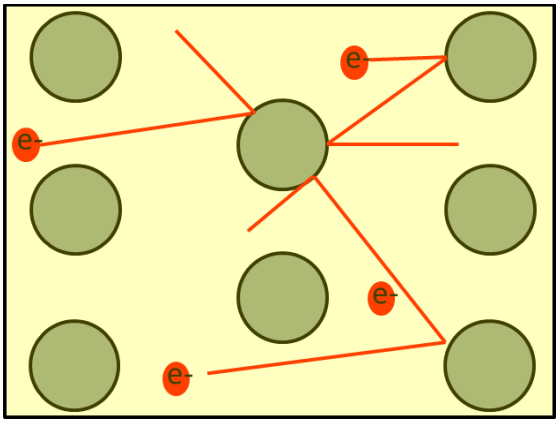

Figure 2.2. Drude model accounts for free electrons moving within the metal lattice composed of heavier metal ions.

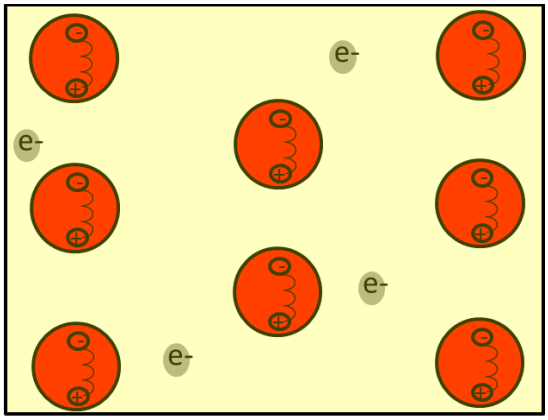

Figure 2.3. Lorentz model accounts for bound electrons within the lattice metallic ions.

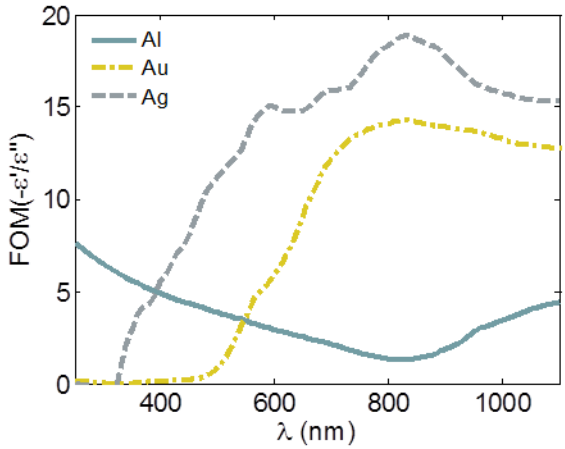

Figure 2.4: Figure of merit of aluminum, gold, and silver at ultraviolet, visible, and near-infrared wavelengths.

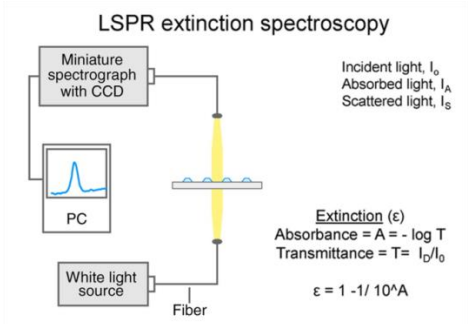

Figure 2.5: Localized Surface Plasmon Resonance spectroscopy measurement setup. Adapted with permission from [27]. Copyright 2007, Annual Reviews

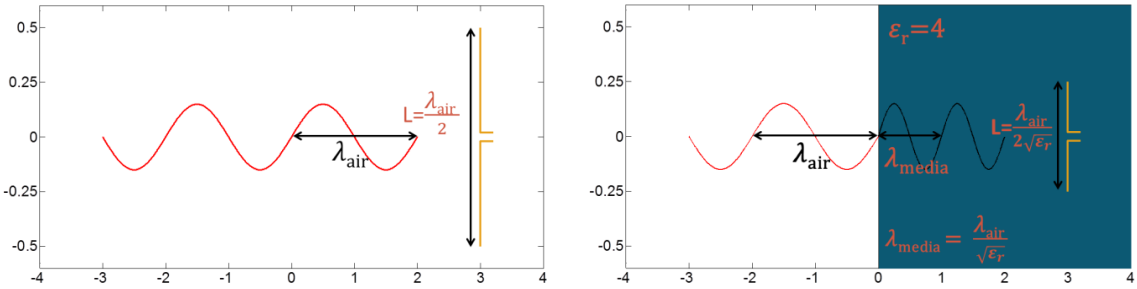

Figure 2.6: Effect of embedding a dipole antenna within dielectric media. a) The antenna required to interact with a wave is half the wavelength. b) Embedding the antenna in a dielectric medium reduces the wavelength and in turn the required antenna size.

Table 2.1. Expressions for α and β for various types of media. Table adapted from [19].

	General Media	Lossless Media	Low-Loss Media	Good Conductor
α	$\omega\sqrt{\frac{\mu\varepsilon'}{2}\left[\sqrt{1+\left(\frac{\varepsilon''}{\varepsilon'}\right)^2}-1\right]}$	0	$\frac{\sigma}{2}\sqrt{\frac{\mu}{\varepsilon}}$	$\sqrt{\pi f\mu\sigma}$
β	$\omega\sqrt{\frac{\mu\varepsilon'}{2}\left[\sqrt{1+\left(\frac{\varepsilon''}{\varepsilon'}\right)^2}+1\right]}$	$\omega\sqrt{\mu\varepsilon}$	$\omega\sqrt{\mu\varepsilon}$	$\sqrt{\pi f\mu\sigma}$

Table 2.2: Parameters describing the complex permittivity of metals.

Metal	Conductivity (S/m)	Relaxation Time τ (sec)	Plasma Frequency ω_p (s^{-1})
Aluminum	$3.96\text{x}10^{7}$	$1.1\text{x}10^{-15}$	$22.9\text{x}10^{15}$
Gold	$4.1\text{x}10^{7}$	$9.3\text{x}10^{-15}$	$13.8\text{x}10^{15}$
Silver	$6.1\text{x}10^{7}$	$31\text{x}10^{-15}$	$14.0\text{x}10^{15}$
Copper	$5.76\text{x}10^{7}$	$6.9\text{x}10^{-15}$	$13.4\text{x}10^{15}$

CHAPTER 3

AN IMPLANTABLE ANTENNA DESIGNED FOR EASE OF MANUFACTURING

3.1 Abstract

This paper describes the design of an implantable antenna designed for improved ease of manufacturing. The antenna is a PIFA spiral mounted on the titanium circuit enclosure (71 x 56 x 8 mm in size), designed to operate in the 402–405 MHz MICS band. The antenna is manufactured "upside down" by molding the silicone superstrate first, placing the radiating element (cut from titanium foil) against it, then pouring epoxy into the mold to form the substrate. The ground point is bent from the end of the foil cutout and glued against the battery pack using conductive epoxy. The entire antenna is easier to build and is expected to have fewer points of failure than similar designs proposed previously.

3.2 Introduction

Implantable medical devices touch virtually every major function in the human body. Cardiac pacemakers and defibrillators [27], neural recording and stimulation devices [29], and cochlear [30] and retinal [31] implants are just a few of the many implantable medical devices available today. Wireless telemetry for these devices is necessary to

monitor battery level and device health, upload reprogramming for device function, and download data for patient monitoring. Most commercial devices today use inductive coupling [32] for telemetry (and also often for power transfer). Implantable antennas have been used for monitoring in a number of research applications and have been proposed for wider use to increase the communication distance between the implant and external communication device. This paper addresses the design for manufacturability of these antennas.

Today's implantable antennas include basic dipoles or monopoles [33]–[35] or (more often) various shapes of microstrip patch or planar inverted F (PIFA) antennas [31], [35]–[39] including genetic algorithm (GA) designs [37]. This paper will focus on the common PIFA designs, which sandwich the planar radiating element of the antenna between insulating substrate and superstrate layers, and use the metal battery pack from the implant as the ground plane for the antenna. The antenna is designed to work in the 402–405 MHz Medical Implant Communication Services (MICS) band [40] and to meet RF safety guidelines for Specific Absorption Rate (SAR) [41], [42].

Implantable antennas must be long-term biocompatible, which is typically accomplished by using materials with low adherence and low chemical activity with the body. In this paper we will focus on the use of silicone (for superstrate), epoxy (for substrate), and titanium (radiating elements and circuit enclosure). By their nature, biocompatible materials such as titanium resist adhesion, thus making it difficult to seal layers of the antenna together and keep body fluids out of the antenna. An epoxy provides a good binding agent, but is difficult to mold. Its conductivity can be high or low as needed. Silicone provides a good sealant and insulation to keep body fluids from shorting

out the antenna, but is also difficult to adhere to titanium. This paper addresses these manufacturing issues in a biocompatible antenna design.

The sections that follow describe the process used to design and study spiral implantable antennas from the perspective of ease of manufacturability. In section 3.3, an easy to manufacture design is described where consideration is given to materials used as well as ease of assembly with chosen materials. Section 3.4 discusses simulation of the design and the effect of various parameters on antenna performance. This is followed by measurement results in section 3.5.

3.3 Design for Manufacturability

The antennas in this study, shown in Figure 3.1, were designed for a research monitoring application in the torso. They were designed to have a reflection coefficient (S_{11}) < -10dB in the Medical Implant Communication Service (MICS) band of 402 to 405 MHz [40] and to transmit as far as possible while still satisfying the 1.6 W/kg Specific Absorption Rate (SAR) limit [41], [42]. Although omnidirectional transmission would have been ideal, this was not an option as the torso attenuates the fields on the back side of the antenna, so they were designed to transmit in as broad a swath as possible. Although used only briefly in the research application, the antennas were designed to be long term biocompatible.

3.3.1 Ground Plane

As shown in Figure 3.1, the 71 x 56 x 8 mm titanium circuit enclosure was used as the ground plane for the antennas. This was a predefined size and shape. The challenge was

how to design the antenna so that it could be efficiently prototyped and manufactured without compromising the hermetically sealed can.

3.3.2 Superstrate

A layer of medical grade silicone [43] was used as a superstrate to insulate the spiral radiating element from the body (which is conductive and would short it out). Unlike previous designs that were built by gluing a solid substrate such as Teflon onto the can, followed by the radiating element and superstrate, this antenna was built by molding the superstrate first, with a curved outer surface. A "well" molded in the inside of the superstrate was designed to hold the radiating element and epoxy substrate, which would later be poured into this well.

3.3.3 Radiating Spiral

The spiral radiating element was cut from titanium foil. For initial prototypes, this was done by hand with scissors, and for more advanced prototypes, this could be done with a laser cutter. Both methods were effective. The radiating spiral was placed in the interior well of the silicone superstrate to be held in place once the epoxy substrate was poured over it in the well.

3.3.4 Feed

Because the can is hermetically sealed, it was important not to make additional openings in it for the feed or ground pins, as proposed in [31], [35]–[39]. We therefore used the plastic header of the can, where other cables were brought in and out for the

monitoring application, as the junction to the feed. A tab on the spiral was brought up to the header for connection to the antenna feed circuitry inside the can. See Figure 3.1.

3.3.5 Ground Pin

The ground pin for the PIFA was created by bending the titanium foil spiral as shown in Figure 3.1 to create a shorting tab. The shorting tab was attached to the titanium can (ground plane) using conductive epoxy in the final manufacturing step.

3.3.6 Substrate

Epotek 301 epoxy (with low conductivity) [44] was used as a substrate to separate the spiral from the ground plane. With the titanium spiral placed in the well of the silicone superstrate, the Epotek was poured over the spiral, filling the well and creating the substrate. Note also the support tabs in the substrate created by this pour. These tabs were used to ensure that the substrate would stay in place and hold the silicone and titanium spiral securely. Silicone adhesive and conductive epoxy was then used to bind the substrate to the can and to connect the ground shorting tab to the titanium can.

3.4 Simulation and Design

In designing the antennas, different factors were considered in order to merge antenna performance with manufacturability. The sections that follow describe the effects of shape, materials, and optimal shorting connection type and location. Figure 3.2 and Figure 3.3 show the two antennas considered. Configuration 2 is essentially the design in [16]. Configuration 1 is a more easily prototyped version of the same antenna. The labels

shown in the figures are defined as follows:

L = Length of antenna

D = Distance between feed and shorting tab

S = Distance between shorting tab and tip of antenna

T = Substrate thickness

P = Superstrate thickness

The antennas were designed and simulated using CST STUDIO SUITE [45], which uses the Finite Integration Technique (FIT) to numerically simulate electromagnetic structures. The transient solver of the software package was used to select the frequency band of interest. The electrical properties of materials used are listed in Table 3.1. The simulations were useful in determining expected resonant frequencies, radiation patterns, and reflection coefficients (S11).

3.4.1 Effect of Spiral Shape

Implantable PIFA antennas have been designed in many shapes, most commonly the spiral we will focus on in this paper, as well as serpentine and GA designs [16], [37]. We explored the two similar shapes in Figure 3.2 and Figure 3.3, both based on [16]. Their resonant frequencies are sensitive to antenna length, and we found Configuration 1 to be easier to prototype accurately. Configuration 1 with L = 114 mm, D = 10.5 mm, S = 0 mm and P = T = 3 mm resonates at 360 MHz as shown in Figure 3.4. Configuration 2 with L = 123 mm, D = 9.5 mm, S = 0 mm and P = T = 3 mm resonates at about 380 MHz.

3.4.2 Effect of Shorting Tab versus Shorting Pin

The planar spiral antennas are inverted-F (PIFA) type antennas. PIFAs use a short circuit at or near the end of the antenna to approximately double (or at least substantially increase) its effective electrical length. This requires a shorting connection between the spiral radiating element and the ground plane (can). The original designs in [16] proposed a shorting pin soldered to the can, but in the manufacturing method demonstrated in this paper, that was not a good option. A shorting pin requires that a hole be drilled through the ground plane in order to weld the connection. This would compromise the hermetically sealed container; plus welding to titanium is difficult. A shorting tab is much easier to manufacture and attach. It can be built as an extension of the spiral, bent into place, and attached to the ground plane with conductive epoxy. A shorting tab results in a slightly higher resonant frequency then a shorting pin as shown in Figure 3.4, but this can be accounted for in the design.

The shorting tab must be placed at the far end of the spiral (S = 0), while the ground pin was often proposed a distance S from the end. Changing the distance between the shorting pin/tab and the feed affects impedance matching of the antenna, but has little effect on resonance frequency [16]. Additional simulations showed that there is an optimal distance, D, between shorting tab and feed. This optimal distance varies depending on the placement of the shorting tab and length of the antenna.

3.4.3 Effect of Substrate and Superstrate Shape

The effect of substrate and superstrate shape was also studied in order to determine its effect on antenna performance. Although it is simple and relatively easy to design and

simulate antennas using hexahedral substrates and superstrates, in practice the sharp edges and corners of these shapes should be avoided in implantable antennas for medical reasons. The antennas manufactured in this study, therefore, used smooth convex-shaped silicone superstrates shown in Figure 3.5, enclosing both the substrate and radiating element. The shape of the superstrate changed the resonant frequency by less than 1 MHz.

3.4.4 Effect of Material Properties

In order to study the effect of variation in materials, we optimized Configuration 2 to resonate at 402 MHz with the initial set of material properties shown in set 1 of Table 3.2. We subsequently changed the material properties of each of the antenna's components in order to determine the effect of these variations on its performance. The highlighted entry on each row of Table 3.2 shows the material changed. The change in resonant frequency and reflection coefficient is shown at the end of each row and graphed in Figure 3.6.

The electrical properties of the surrounding (torso) environment play an important role in antenna performance. Both the tissue properties and their exact size/shape at the implant site vary substantially from individual to individual, which has been shown to add substantial uncertainty to the simulation results as well as detuning the antenna [46], [47]. For simplicity, we simulated and measured the antennas in a plastic jar 11 cm in height and 10 cm in diameter. First (row 1) the antenna was simulated in blood bank saline [48], which was later used for measurements (Set 1). Next, knowing that any simulations will thus be approximate anyway, we designed the antenna in heterogeneous

2/3 muscle [49] (the de facto standard when the full body detail is not simulated). This is "Set 2" antenna in Table 3.2. The antenna in saline has a resonant frequency 6 MHz below that in 2/3 muscle.

We next considered the uncertainty of the substrate Epotek and superstrate silicone. Epotek can vary between ε_r = 3.5 (Set 1) and 4.0 (Set 3) and silicone between ε_r = 3.1 (Set 1) and 3.5 (Set 4). Increasing either of these dielectric constants decreases the resonant frequency, similar to what has been previously reported in [16].

Since the titanium circuit enclosure is being used as a ground plane, reducing its conductivity is sometimes desirable to reduce interference caused by eddy currents. Set 5 in Table 3.2 shows that this resulted in only a 1 MHz shift in resonant frequency.

3.5 Measurements

Antennas were manufactured in Configuration 1 (with L = 114 mm, D = 9.5 mm, S = 0 mm and P = T = 3 mm, shown in Figure 3.7) and Configuration 2 (with L = 114 mm, D = 10.5 mm, S = 0 mm and P = T = 3 mm, shown in Figure 3.8). The reflection coefficient (S_{11}) and radiation pattern were measured for each antenna. In order to approximate implanted conditions, the antenna was centered in a plastic cylindrical container 11 cm in height and 10 cm in diameter. It was held in place by nylon screws. The tissue simulant material (blood bank saline with PH = 7.0–7.2) was then added to the container. A hole was drilled on the lid of the container to route the cable to the outside of the container. With the cable in place, the hole was then sealed with silicone to prevent the fluid from leaking as the container was rotated to measure the radiation pattern. Figure 3.9 shows the set up for these measurements.

The measured S_{11} values of the antennas are shown in Figure 3.10. Both antennas fall below the -10 dB requirement within the 402–405 MHz band. The resonant frequencies are 390 MHz for Configuration 1 and 409 MHz for Configuration 2.

The measured radiation patterns at 402 MHz in the horizontal plane ($\varphi = 0$) are shown in Figure 3.11 and Figure 3.12 and in the vertical plane ($\varphi = 90$) in Figure 3.13 and Figure 3.14. The antennas are mainly vertically polarized, except directly above the antenna. A circularly polarized receiving antenna is recommended. Configuration 2 radiates approximately 12 dB more than Configuration 1.

3.6 Conclusion

This paper has described the design of implantable PIFA antennas for ease of manufacturability. Based on original designs in [16], slight design changes can produce an antenna that is much easier to manufacture. The antenna is manufactured by molding a silicone superstrate to act as the mold for an epoxy substrate. A titanium foil radiating element is sandwiched between them in this process. A grounding tab is bent at the end of this radiating element, and glued to the titanium can along with the rest of the antenna using conductive epoxy. The feed point is designed to protrude up to the header of the can for easy access to the antenna circuitry without breaching the hermetically sealed titanium can (which also serves as the ground plane of the antenna).

The effects of materials, shape, substrate, and superstrate thickness and optimal short and feed locations were analyzed. Titanium has high enough conductivity to create a very good antenna, even when its conductivity is slightly decreased to prevent eddy current interference. Unlike previous designs, this can and its hermetic seal were not

compromised by this manufacturing design, which was a high priority for this application. The shorting tab epoxied to the can was key to this aspect of the design. The tab and pin had essentially the same resonant frequency but slightly different impedance. This could be tuned by slightly adjusting the location of the tab.

The shape of the radiating element was also studied, and two potential designs were presented. Of these, Configuration 2 radiated approximately 12 dB more power than Configuration 1. It was found that the superstrate can be simulated in a simple hexahedral shape and built in a more biologically acceptable convex shape without significantly changing the properties of the antenna.

The body surrounding the antenna has substantial impact on the antenna properties. Changing the surrounding media from phosphate buffered saline solution to the more realistic 2/3 muscle model of the human body shifted the resonant frequency by about 6 MHz. Since the exact location inside the body is highly variable, the exact resonant frequency will change with placement location within the body anyway, and the 6 MHz change was considered minimal. Because of this anticipated uncertainty, and the fact that the electrical properties of Epotek and silicone were not well characterized, the antenna should be designed with plenty of excess bandwidth to account for these variations. Designing the antenna using these approximate values was sufficient to produce an effective antenna for this application.

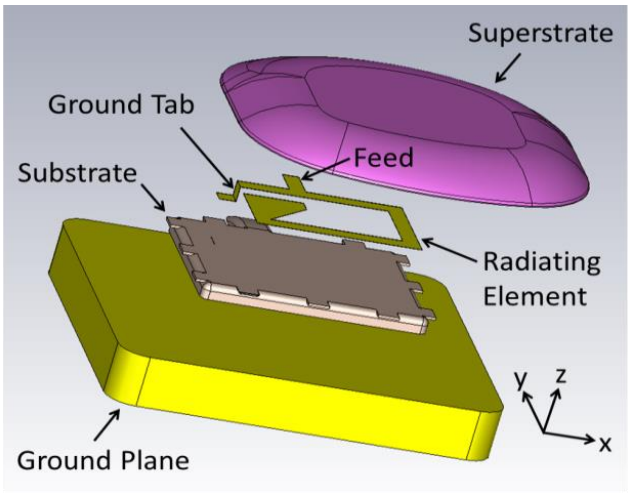

Figure 3.1 PIFA Antenna Assembly.

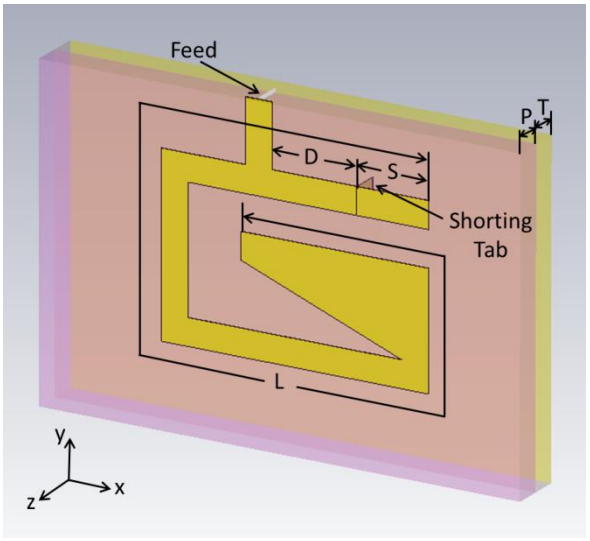

Figure 3.2 Antenna Configuration 1. L = 114 mm, D = 10.5 mm, S = 0mm and P = T = 3 mm.

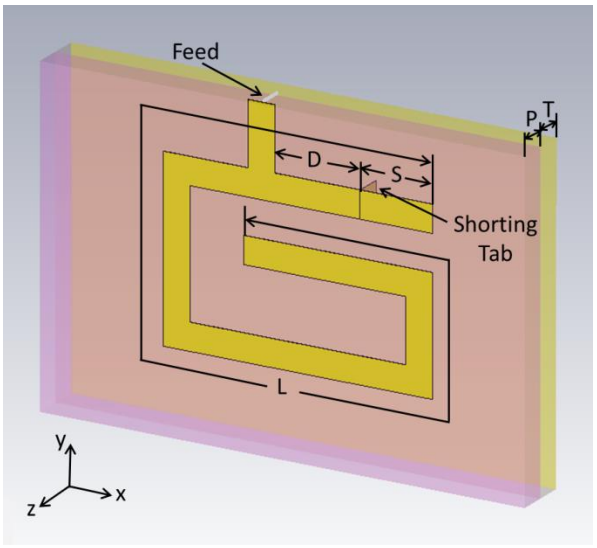

Figure 3.3 Antenna Configuration 2, from [16]. L = 114 mm, D = 10.5 mm, S = 0 mm, and P = T = 3 mm.

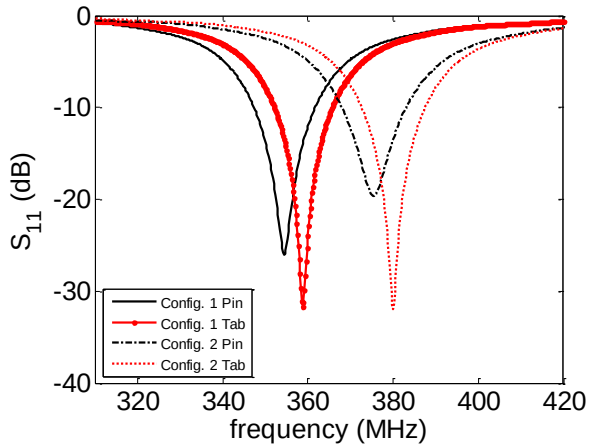

Figure 3.4 Reflection coefficients of Configurations 1 and 2 using Shorting Pin vs. Shorting Tab.

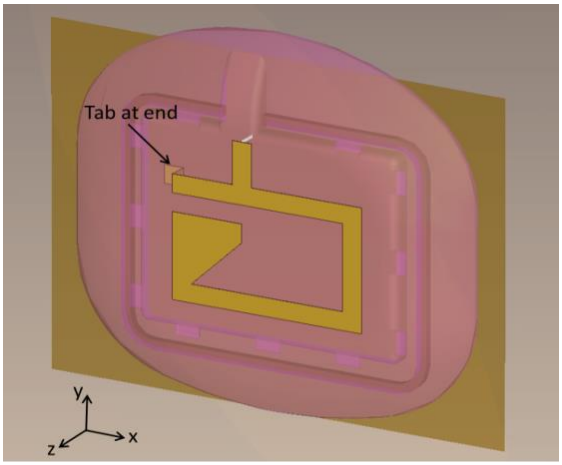

Figure 3.5 Convex shaped superstrate, encapsulating the substrate and radiating element.

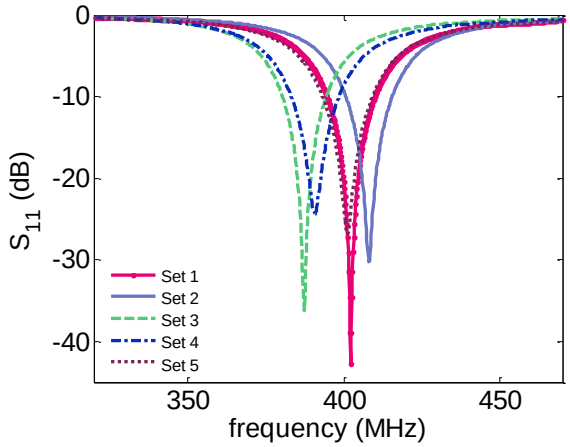

Figure 3.6 Effect of material properties on reflection coefficient.

Figure 3.7 Manufactured Configuration 1.

Figure 3.8 Manufactured Configuration 2.

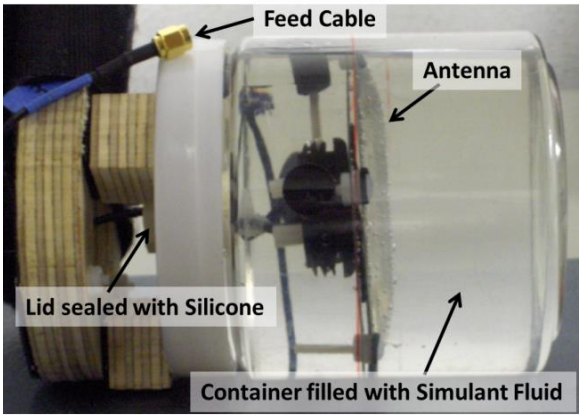

Figure 3.9 Measurement set up.

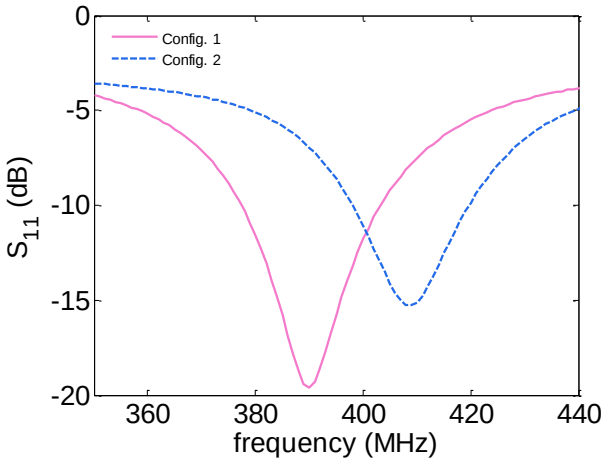

Figure 3.10 Measured reflection coefficient.

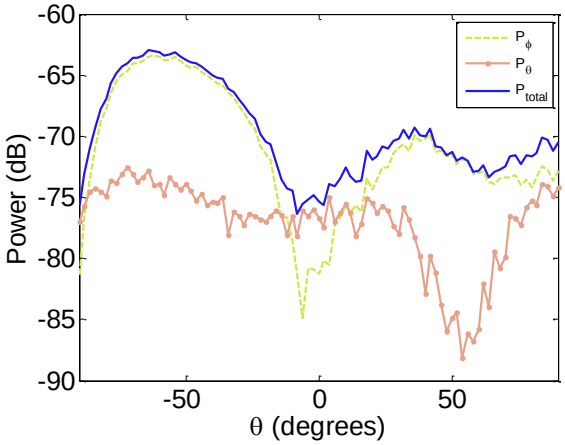

Figure 3.11 Measured radiation pattern for Configuration 1 in horizontal plane ($\varphi = 0$).

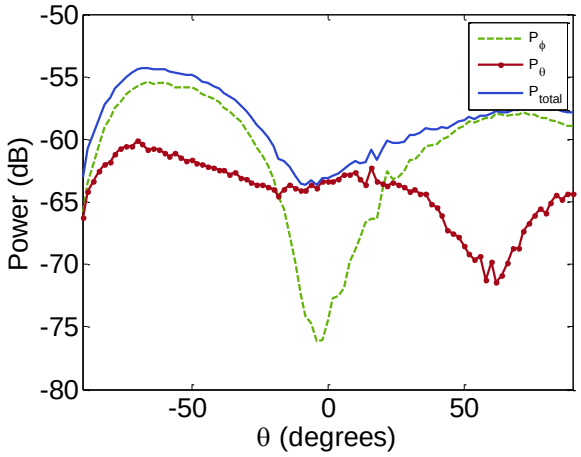

Figure 3.12 Measured radiation pattern for Configuration 2 in horizontal plane (φ = 0).

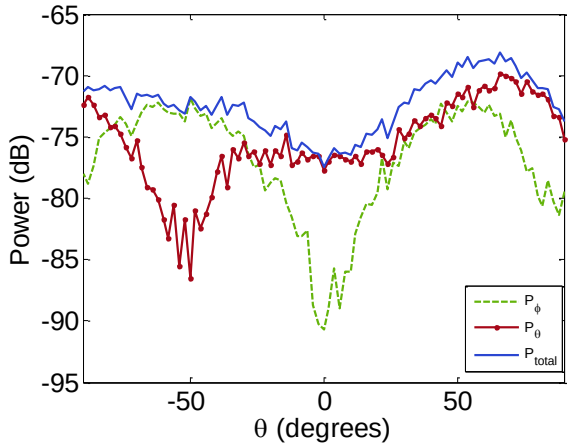

Figure 3.13 Measured radiation pattern for Configuration 1 in vertical plane (φ = 90).

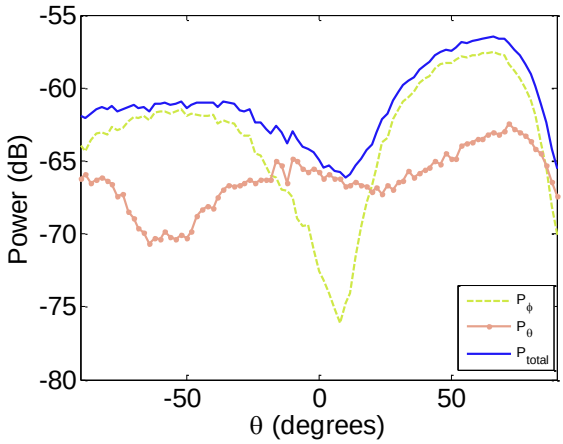

Figure 3.14 Measured radiation pattern for Configuration 2 in vertical plane (φ = 90).

Table 3.1. Material Properties (402–405 MHz).

	Material	ε_r	Conductivity σ (S/m)
Ground Plane	Titanium	1	2.38×10^{6}
Substrate	Epotek 301 Epoxy[44]	4	7.81×10^{-12}
Spiral	Titanium	1	2.38×10^{6}
Superstrate	Silicone, P.N. MED16-6606[43]	3.5	1.9×10^{-4} $\tan \delta = 0.0025$
Surrounding Media	Phosphate Buffered Blood Bank Saline Solution, PH: 7.0-7.2, P.N. 8505 [48]	77.52	1.83
Surrounding Media	2/3 Muscle [49]	42.8	0.646

Table 3.2. Resonant frequency variations as material properties change.

	External Environment	Epotek Substrate	Silicone Superstrate	Ground Plane & Radiating Element	f(MHz)	S11(dB)
Set 1	Saline Solution $\varepsilon_r = 77.5$, $\sigma = 1.83$	$\varepsilon_r = 3.5$	$\varepsilon_r = 3.1$	$\sigma = 2.38 \times 10^{6}$ S/m	402	-42.8
Set 2	2/3 Muscle $\varepsilon_r = 42.8$, $\sigma = 0.646$	$\varepsilon_r = 3.5$	$\varepsilon_r = 3.1$	$\sigma = 2.38 \times 10^{6}$ S/m	408	-30.3
Set 3	Saline Solution $\varepsilon_r = 77.5$, $\sigma = 1.83$	$\varepsilon_r = 4.0$	$\varepsilon_r = 3.1$	$\sigma = 2.38 \times 10^{6}$ S/m	387	-36.2
Set 4	Saline Solution $\varepsilon_r = 77.5$, $\sigma = 1.83$	$\varepsilon_r = 3.5$	$\varepsilon_r = 3.5$	$\sigma = 2.38 \times 10^{6}$ S/m	391	-24.4
Set 5	Saline Solution $\varepsilon_r = 77.5$, $\sigma = 1.83$	$\varepsilon_r = 3.5$	$\varepsilon_r = 3.1$	$\sigma = 0.79 \times 10^{6}$ S/m	401	-26.8

CHAPTER 4

REVIEW OF CRESCENT ANTENNAS

4.1 Crescent Types

Crescent antennas have been studied at frequencies ranging from the RF to the ultraviolet [6], [10], [11], [17], [50]–[72]. In the RF these structures are typically used for communications, but as the frequency increases, countless applications have been proposed and studied. These applications include near-field microscopy probes [17], chemical and biological sensors [17], [50], [52]–[54], [57], [60], [63]–[65], nonbleaching optical labels [17], [65], transmission-localized surface plasmon resonance (T-LSPR) spectroscopy [17], surface-enhanced Raman scattering spectroscopy (SERS) [11], [17], [51], [52], [57], [58], [62]–[67], surface enhanced infrared absorption spectroscopy (SEIRAS) [17], [50], nonlinear laser-induced scanning tunneling microscopy (NLL-STM) [11], initiate photochemical reactions at specific sites [10], [11], single molecule spectroscopy [10], [54], UV sensing applications [10], light guiding, improving imaging systems [60], improving photovoltaics [6], plasmon-enhanced fluorescence spectroscopy [52], [67], metamaterial [52], [53], [55]–[57], [59], [61], superlenses [55], [56], [61], cloaking [55], [56], [61], white light generation [53] and magnetic recording [60].

The term crescent applies to different geometries, including spherical, cylindrical, and planar structures as shown in Figure 4.1. A spherical crescent is typically composed of a

metallic shell open at one end with its cross-section having the shape of a crescent (Figure 4.1a). The structure can be either hollow or contain a dielectric core embedded within. This structure benefits from the benefits of local field enhancement occurring at tips. In the cross-section the structure resembles a crescent with a sharp tip. In its circular symmetry, therefore, the structure expands the hot spot from a tip to a circular line or group of tips [63]. They are fabricated by first casting a monolayer of spherical polystyrene colloids on a photoresist coated glass substrate (Figure 4.2). The colloids are then coated with a gold layer using electron beam evaporation. The sample is kept rotating at an angle with respect to the gold target during deposition. Lift-off of the crescents from the structures is then accomplished using acetone. The polystyrene cores can then be dissolved or kept depending on the application.

Optical planar crescent antennas consist of a crescent-shaped metal on top of a substrate (Figure 4.1). This structure also takes advantage of high localization of fields into small volumes. A number of different fabrication techniques have been proposed for these structures including nanosphere template lithography (NTL) [52], shaped nanosphere lithography [61], electron beam lithography (EBL) [58], and oblique angle metal deposition on nanopillar sidewalls [59].

Nanosphere template lithography is an extension of Nanosphere lithography and begins by first depositing beads on a substrate as shown in Figure 4.3a. A layer of metal is then deposited at an angle with respect to the normal to the substrate (Figure 4.3b). This is followed by etching at a right angle to the substrate where the bead acts to protect the metal beneath it (Figure 4.3c). The beads can then be lifted off using tape leaving the crescent-shaped antennas (Figure 4.3d) [52].

Shaped nanosphere lithography begins by spin coating a layer of polystyrene spheres to form a close-packed array. An argon/oxygen (Ar/O2) reactive ion etch (RIE) is then used to change the diameter and shape of the nanospheres. This causes the spheres to collapse and their shape changes to mushroom-like structures. This is followed by evaporation or sputtering of gold onto the array of collapsed spheres. In this step some metal builds up under the overhang of the collapsed spheres. A shaped nonconductive strip (either a piece of silicon wafer or a glass microscope slide) is placed on top of a narrow portion at the edge of the sample. A second reactive plasma etch step is then used to remove metal. In this step the nonconductive strip that was previously placed on top of the sample serves to direct the flow of reactive ions resulting in crescent-shaped structures. The polystyrene beads are finally removed using tape [61].

RF planar antennas can be made by etching the crescent shape on commercially available RF substrates (such as Rogers, FR4, etc.) and etching, peeling, or milling away the undesired metal. Planar RF antennas typically include a strip of metal to feed and match the impedance of the antenna to the source and maximize the radiated power. This microstrip requires a ground plane beneath the dielectric substrate. For the sake of completeness, it is worth mentioning that cylindrical crescent structures have been studied as possible elements for metamaterials. These structures consist of long insulator cylinders partially covered by metal (Figure 4.1). Cylindrical crescents have been theoretically studied in [73] and [74].

4.2 RF versus Plamonic Antennas

The resonating charge oscillations of RF antennas differ from that of optical antennas operating at high frequencies. This can be explained by examining the Drude model for conductivity of metals, equation 4.1, over the frequency range from RF to optical frequencies.

$$\sigma = \frac{\sigma_o}{1+j\omega\tau} \qquad (4.1)$$

Consider for instance the complex conductivity of silver, $\sigma = \sigma' + j\sigma''$, where σ' represents the real part and σ'' represents the imaginary part of the conductivity. The real and imaginary parts of the conductivity are plotted in Figure 4.4. It can be observed from this graph that the real part of the conductivity dominates at RF and into the far infrared range. As the frequency increases, the imaginary part of the conductivity increases until it surpasses the decreasing real part and begins to dominate.

Using the values from Figure 4.4, the phase of the conductivity, calculated as $\theta = \tan^{-1}\left(\frac{\sigma''}{\sigma'}\right)$, is plotted in Figure 4.5. It is observed from this graph that the conductivity undergoes a phase shift from being purely real at RF frequencies ($\theta = 0^{o}$) to being almost purely imaginary ($\theta = 90^{o}$) at optical frequencies.

Considering then the constitutive relation $E = \sigma J$, it can be noted that at RF frequencies, the current follows in phase with the electric field since the imaginary part of the conductivity is negligible compared with the real part: $E = \sigma J = (\sigma' + j\sigma'')J \approx \sigma' J$. At optical frequencies, on the other hand, the approximately imaginary conductivity results in a 90^{o} phase lag of the current density with respect to the electric field: $E = \sigma J = (\sigma' + j\sigma'')J \approx j\sigma'' J$.

In direct analogy to a mass-spring oscillating system, a resonance can result from the

90° phase lag between the oscillating electrons and the applied electric field as illustrated in Figure 4.6. In this analogy, the spring represents the Coulomb interaction describing the force of attraction between the positively charged lattice ions and the negatively charged conduction electrons. The mass of the electron is represented by m_e and its charge by q. The damping at the interface between the mass and the holding surface accounts for Ohmic and radiative losses. The natural response of the system results in a minimum velocity at the positions of maximum force caused by the compressed or stretched out spring. Maximum velocity occurs between these two positions when the spring exerts minimum force on the mass. The relationship between force and velocity for the system is shown in Figure 4.6. The figure shows that there is a 90° phase difference between the mass velocity and the force. An applied force, F, that matches this natural response creates a resonance on the system.

In terms of electric parameters, the electric field is directly proportional to the force, F = qE, and the current density is directly proportional to the velocity, J = qv. At resonance, therefore, a 90° phase difference exists between the applied field and the current density. This type of resonance is referred to as plasmon resonance.

The different material properties of metals in RF versus optical regimes results in different behavior of antennas. One difference pertains to scalability of their resonance with antenna dimensions. At RF frequencies, the resonant frequency can be scaled by simply scaling the antenna. This relationship does not apply at optical frequencies. This is a direct consequence of the reduction of conductivity of metals at higher frequencies. The high conductivity of metals at RF frequencies results in a very low penetration depth of fields into the metal. Current flow can therefore be approximated by an equivalent

surface current density [75]. This surface current density determines the fields radiated by the antenna and the metal properties do not significantly affect the response of the antenna [76]. The effective wavelength seen by the antenna is the same as that of the surrounding media. At optical wavelengths, however, the conductivity of metals greatly decreases, resulting in increased penetration depth of fields. The fields then respond to the dielectric properties of metals, resulting in a decreased effective wavelength [77]. Also, because dielectric properties are dependent on the metal, the resonance response of a particular antenna is also dependent on the metal used. This is in contrast to RF antennas, where the metal used has little effect on resonant frequency.

The frequency at which the resonance response changes is not clear-cut, but as the frequency increases, the resonance transitions from a purely RF "antenna-like" response to a plasmonic response. In practice, the resonance type can be identified by observing the resonance behavior when different metals are used for the same structure. The distinction between these resonance types has been observed to blur in the mid-IR for crescent antennas of gold and silver. In that case the distinction between the mostly geometry-dependent "antenna-like" resonance was differentiated from the materials dependent plasmonic resonance by running simulations using a perfect electric conductor (PEC) as the metal for the structure and comparing with the results of using silver and gold.

4.3 Materials

In order to produce a good resonance, the metal used for the antenna needs to produce low losses. The dielectric constant of the metal can be used to determine its usefulness.

To provide a good resonance the real part of the complex dielectric function needs to be negative and as large as possible in order to increase the reflectivity, and the imaginary part needs to be as small as possible in order to decrease penetration losses [78]. A figure of merit (FOM) therefore can be defined as FOM = $-\varepsilon'/\varepsilon''$ [26]. Figure 4.7 shows the FOM for typical metals used in plasmonic antennas. The wavelength range over which each metal is useful can readily be observed from this graph. Aluminum, for instance is a good metal from the UV and into the visible, but its figure of merit decreases in the near-infrared. This is caused by interband transitions that occur at approximately 800 nm. Gold interband transitions occur in the range between 530–550 nm, and silver has them at approximately 400 nm [78]. These transitions limit their usefulness in the visible and UV, but they prove very useful in the near- and mid-infrared.

The choice of substrate is also important in the fabrication of nanoantennas. A typical setup for measurement of fabricated antenna samples is shown in Figure 4.8a [27]. Measuring the response of an antenna requires the assembly (substrate and antennas) be illuminated by a laser. Illumination of the antennas results in three measured parameters that characterize the response of the antenna, scattering, absorption, and extinction. As the name implies, absorption corresponds to light that is absorbed by the assembly and scattering corresponds to light that is scattered in any direction other than that of the detector. Extinction is the sum of scattering and absorption and corresponds to light that is not transmitted to the detector due to absorption or scattering by the sample. It is readily observed that the parameters of interest are based on transmission of light through the assembly. The substrate, therefore, needs to be transparent over the wavelength range of interest in order for the detector to gather light of resonant structures on top of the

substrate. Glass is transparent in the UV and visible range with a dielectric constant of 1.46 at a wavelength of 500 nm [79]. In the near-infrared, calcium fluoride (CaF_2) is transparent with a wide transmission range from the ultraviolet to the infrared as shown in Figure 4.8b. The refractive index of CaF_2 is 1.399 at a wavelength of 5 μm [80].

4.4 Investigations on Crescent Antennas

Although the FOM provides an initial assessment on the usefulness of materials for particular wavelength ranges, the geometry of the antenna greatly influences its resonance. Nanocrescent antennas have been shown to support resonances from the UV through the mid-IR. The descriptions below sample results from the long list of papers written on crescent antennas [6], [10], [11], [17], [50]–[72]. In the discussion that follows, a source polarized along the width of a planar crescent antenna will be defined as a short axis polarized source, E_s, as shown in Figure 4.9. Similarly, a source polarized along the length of the antenna will be defined as a long axis polarized source, E_l.

4.4.1 Ultraviolet

4.4.1.1 Scaling the Response of Nanocrescent Antennas into the Ultraviolet

The resonance response of aluminum nanocrescent antennas to variations in height, width and diameter was studied in [10]. In this study, FDTD simulations are used to show that these crescents exhibit dipole and quadrupole modes in the visible and a rich spectrum of modes in the ultraviolet. Average field enhancements of ~100 were shown at UV wavelengths for field intensity values averaged over a 1000 nm^3 volume. Field

enhancements of ~250 have been shown at short axis dipole resonances and ~60 at long axis quadrupole resonances occurring in the visible range. Figure 4.10a shows the field enhancement variations as a function of crescent diameter. The results also show that at dipole resonances the fields are localized at the tips and at higher order mode resonances the fields can be localized to the tips and backbone of the crescents (Figure 4.10b).

The article also studied the effect of aluminum oxide (Al_2O_3) on the response of the crescents. Aluminum naturally develops an approximate 3 nm layer of Al_2O_3. This layer results in dampening of resonance resulting in decreased field enhancement. Average field enhancement values of ~20 for 180 nm diameter crescents were estimated at UV wavelengths when the Al_2O_3 layer surrounding the crescent is included (Figure 4.11a). Also, since the aluminum gets buried within the Al_2O_3, the highest fields are spatially split along the sides of the tips at dipole resonances (Figure 4.11b).

4.4.2 Visible

4.4.2.1 Toward High-efficiency Solar Upconversion with Plasmonic Nanostructures

The use of spherical nanocrescent antennas to improve the efficiency of photovoltaics was investigated in [6]. Efficiency of solar cells can be improved by using upconversion, where lower energy (i.e., longer wavelengths) photons can be converted to the higher energy (shorter wavelength) photons needed by the solar cell. The idea is to place an upconverter under the solar cell. The upconverter then converts lower energy photons to higher energy and re-emits them to be absorbed by the solar cell. Preventing the successful implementation to this concept are the low absorption efficiencies and high

nonradiative recombination rates of upconverting systems. Upconversion can be improved by using silver crescents with upconverter-doped dielectric cores as the upconverter layer.

Simulations of these crescent structures show multiple resonances in the visible range. The crescents could therefore be tuned to efficiently absorb at longer wavelengths and efficiently emit upconverted photons at shorter wavelengths. The article also studies the field intensity along the axis of the crescent as a function of the distance from the tips. The study shows that the field intensity at resonance is strong within the crescent even when the incident light is not perpendicular to the structure. This is beneficial in exposing more of the upconverting-core to incoming light.

4.4.2.2 Fabrication of Aluminum Crescent Nanoantennas by Copper Mask Nanosphere Template Lithography

Fabrication of aluminum crescent nanoantennas based on modified nanosphere template lithography (NTL) is discussed. Although NTL as described above is an effective method for creating gold and silver nanocrescent antennas, it proves difficult in making aluminum crescents. The reason for that is that unlike gold and silver, which can be etched by using Ar+ plasma, aluminum cannot. In this investigation, a modified version of NTL is used to fabricate aluminum crescent antennas as illustrated in Figure 4.12. The process begins as usual by depositing polystyrene beads on a substrate (Figure 4.12a). Copper is then deposited at angle with respect to the normal to the substrate (Figure 4.12b). The bead shadows an area on the opposite side where copper is not deposited, thus creating a mold where aluminum can be deposited. Aluminum is then

deposited again at an angle with respect to the normal, but on the opposite side of the substrate (Figure 4.12c). The copper can then be chemically dissolved using nitric acid, and the excess aluminum deposited on top of the copper can be removed by sonicating the substrate in nanopure water. The result is a crescent-shaped nanoantenna (Figure 4.12d).

In fabricating the antennas sometimes multiple templates agglomerate together. The fabricated sample therefore contains not only single isolated crescents, but at times multiple crescents joined together. Since dimers are more prevalent other than single isolate crescents, the expected response is the average response of single crescents and dimers. Simulated results for isolated and dimer crescents are shown in Figure 4.13 a and b, respectively. In order to compare simulated and measured results, a weighted sum the calculated response of single crescents and dimers was performed. This is rationalized by noting that the amplitude of each peak will depend on the number of single crescents and dimers present in the sample. Based on the measured results shown in Figure 4.13d, the largest peak of the simulated long axis dimer response (Figure 4.13b) was weighted down to approximately 75% of the long axis single crescent response (Figure 4.13a). The weighted results were then added together and compared to the measured response as shown in Figure 4.13d. The calculated weighting factor was also used for the short axis response of single and dimer crescents in order to keep a consistent comparison as shown in Figure 4.13c. Figure 4.13 c and d show very good agreement between measured and calculated results. Also the simulated results highlight an additional long axis resonance at approximately 1600 nm that appears as a shoulder in the measurements. Agreement between measured and simulated results is a very exciting find as it opens the door for the

use of higher order resonant modes of crescent nanoantennas in UV plasmonics as will be discussed in Chapter 5.

4.4.2.3 Other Reported Visible Resonances

Studies of planar crescent antennas have also reported resonances in the visible range for Al, Ag and Au nanocrescents. In [10], simulations of 80–200 nm diameter aluminum nanocrescents have shown dipole resonances associated with dipole modes for short axis polarized sources and quadrupole resonances for long axis polarized sources. Hot spots associated with these resonances are exhibited at the tips of the crescents. Also, measurements and simulations of silver and gold nanocrescent antennas have been shown to possess resonances in the visible range [10], [11], [17], [50], [52], [53].

4.4.3 Near-IR

4.4.3.1 Fabrication of Crescent-Shaped Optical Antennas

In [52] nanosphere template lithography (NTL) was initially introduced as a method for fabricating nanocrescent structures as illustrated in Figure 4.14a. This method involves (1) deposition of colloid templates on a substrate followed by (2) oblique metal deposition. In step (2), the colloids serve to shadow an area opposite to the template so that metal is only deposited on one side of the colloid. This step is followed by (3) ion beam milling where an argon-ion-beam is oriented perpendicular to the substrate to mill away metal not directly below the protective colloids. The colloids are then removed from the substrate, (4) leaving only the crescent-shaped antennas. Using this process, a high degree of control over the crescent's features including the crescent diameter,

thickness, and gap size (opening between tips) is demonstrated. As shown in Figure 4.14b, the gap size can be reduced by sequentially evaporating metal, azimuthally rotating the substrate and evaporating metal again. The two deposition steps result in the superposition of two rotated crescents that result in closing of the gap. Using this approach, various gold crescents are fabricated on glass substrates. The extinction spectra dependence on polarization of incident field is shown in Figure 4.14b. The figure shows that when the source is polarized along the long axis of the crescent (top crescent in Figure 4.14b), two resonant peaks are observed at 538 nm, 1300 nm, and 1958 nm. Rotating the polarization to coincide with the short axis of the crescent (middle crescent) results in resonance peaks at 538 nm and 830 nm. Illuminating at 45° incident polarization (bottom crescent) excites all modes of the crescent.

4.4.3.2 Highly Tunable Infrared Extinction Properties of Gold Nanocrescents

In [17] the extinction properties of gold nanocrescents are shown to be highly tunable in the infrared by manipulation of the crescent's diameter, aspect ratio of diameter to height or width, and operating environment dielectric properties. The crescents are manufactured by NTL as reported in [52]. Using this method, the width of the crescent can be increased by increasing the angle at which metal is deposited. It is reported that the crescent's tips can be made sharper by increasing the ratio of length to width or to height. Measured spectra of crescents with diameters of 125 nm, 194 nm, 356 nm, and 465 nm show that all structures are characterized by at least three resonant peaks (Figure 4.15a). The first occurs in the visible range and is independent of the polarization of the

source. The next peak (termed transverse peak) is strongest when the incident field is polarized along the short axis of the crescent. The peak occurring at the longest wavelength (longitudinal peak) is strongest when the source is polarized along the long axis of the crescent. The study shows a linear relationship between the longitudinal and transverse modes as a function of crescent diameter (Figure 4.15b).

The article also investigated the effect of dielectric environment on the resonant wavelength. Using a 194 nm diameter crescent, it is reported that an increase in the environment's refractive index results in red-shifting of the resonance peaks (Figure 4.16a). Figure 4.16b shows that there is a linear dependence between the environments refractive index and resonance wavelength. The slope of the line defines the sensitivity of the crescent to the change in the dielectric environment.

4.4.3.3 Polarization Anisotropy of Multiple Localized Plasmon Resonance Modes in Noble Metal Nanocrescents

In [11] the anisotropic behavior of gold and silver nanocrescent antennas with respect to polarization of incident light is demonstrated. The experiements show controlled induction of resonance modes based on incident polarization of light. Long axis polarized sources result in only long axis quadrupole (LA-Q) and dipole (LA-D) resonances being observed, while short axis polarized sources only excite short axis dipole (SA-D) resonances. Exciting with a source polarized at an angle between these two extremes results in both long and short axis resonances being excited simultaneously. The strength of each resonance is dependent on the angle of polarization of the source. Figure 4.17a shows the simulated results for a 356 nm diameter gold crescent. Figure 4.17b shows the

experimental results.

Simulations also show that LA-D resonance at λ = 2275 nm couples very strongly with incident light polarized along the long axis resulting in the highest field enhancement localized to the tips of the crescent (Figure 4.18a) while the LA-Q at λ = 950 nm couples less strongly, resulting in weaker field enhancement at that wavelength (Figure 4.18b). Similarly, the SA-D at λ = 1295 nm couples strongly with a source polarized along the short axis resulting in high field intensity at this resonance (Figure 4.18c). These results provide the opportunity to control the spatial distribution of optical near field enhancement through polarization of incident light.

4.4.3.4 Plasmonic Nanocrescent Arrays Fabricated by Controlled Plasma Etching of Polystyrene Nanosphere Templates

A simplified approach to fabricating crescent antenna arrays using Nanosphere Template Lithography is investigated. The study shows the creation of crescent arrays by first close packing beads in hexagonal patterns. This is followed by the key step of shrinking the beads using oxygen plasma to allow space for metal deposition. The following steps are typical of NTL, namely, metal deposition at an angle with respect to the normal to the substrate followed by etching perpendicular to it. The process is illustrated in Figure 4.19. It was noted that reducing the size of the templates past ½ of the original size, resulted in roughening producing “spiky beads.” The resulting crescents fabricated from these “spiky beads” were distorted. These distorted crescents produced some interesting results, as will be described below.

Using the fabrication technique described above, the orientation of the crescents within the hexagonal pattern is dependent upon the orientation of the hexagon when metal is deposited. SEM images indicated two main orientations for fabricated crescents. These are illustrated in Figure 4.20. In the first orientation, the crescent tips are next to each other in a vertical fashion, while in the second the tips are oriented more towards the backbone of adjacent crescents. Since both patterns exist in the same substrate, the measured spectrum is expected to be the average response of both arrangements. Extinction measurement spectra for isolated crescents, smooth crescent arrays, and distorted crescent arrays are shown in Figure 4.21. The simulated spectra of arrays arranged as in Figure 4.20 a and b is shown in Figure 4.22 a and b, respectively. The predicted response matches observations, although simulated dipole resonances are blue shifted in comparison to measurements. Comparison between the spectra of dispersed, isolated crescents and that of the smooth arrays shows that both share the same resonant peaks. The measured long axis dipole resonance for the arrays is blue shifted and broader in comparison to that of single isolated crescents. Changes in the bandwidth of short axis dipole resonances are not as significant and experimental results show blue shifting of the array resonance in comparison to single isolated crescents. The field patterns at short and long axis resonance wavelengths for each of the array configurations shown in Figure 4.20 are shown in Figure 4.23. In each figure, the black arrow indicates the source intensity.

Measured spectra of distorted crescent arrays seem to show an additional peak as indicated by the black arrow in Figure 4.21c. Although simulations of these crescents using AFM data show this resonance (Figure 4.24), the other resonances are significantly

red-shifted in comparison to measured data. This is possibly caused by instrument distortion of AFM images, and additional analysis is needed.

4.4.3.5 Sensitivity of Crescent-Shaped Metal Nanoparticles to Attachment of Dielectric Colloids

In [54] the response of planar nanocrescent antennas when polystyrene beads are brought within the vicinity of the tips is studied in simulation and experiment. Experimentally, the beads are deposited in the substrate containing the crescents. This is followed by moving the beads to various locations around the tips using a scanning force microscope (SFM).

Simulations were performed by using a simplified model of the crescents where the top and bottom surfaces are flat crescents joined by vertical walls. Simulation results predicted an 8.5 nm red-shift of the resonance peak when the bead is brought to the tip. Experimentally, shifts ranging from 8.8 nm to 16.5 nm were observed. Discrepancy of theoretical and experimental results is attributed to various factors, including differences between the idealized crescent used in simulations and the actual fabricated antenna. It was also noted that when the colloid and crescent were separated by a small gap, no resonance shifting was observed. This indicates the small probe volumes of nanocrescent antennas and shows the promise of these structures in single molecule detection where the volumes need to be small enough to discriminate one molecule from others located close by.

4.4.3.6 Peptide-Nanoparticle Hybrid SERS Probe for Dynamic Detection of Active Cancer Biomarker Enzymes

In [65], gold spherical crescents with polystyrene cores were used to study detection of active cancer biomarker enzymes in real time. In this study, crescents were lined with specially designed peptides composed of HSSKLQ (which has very high affinity to PSA), a cysteine group to attach the peptide to the crescent and a Raman active molecule such as biotin or Rhodamine 19 (R19) to provide the detection signal (Figure 4.25a). The initial peptide-conjugated crescent spectrum has three peaks, one from the Raman active molecule (biotin or R19), another from the crescent and the last from the peptide. After exposure to PSA, the peptide is digested by the PSA dislocating the Raman tags from the crescents and causing the Raman tag peak to disappear from the spectrum (Figure 4.25b). The experimental graphs showing the disappearance of the biotin peak upon exposure to PSA is shown in Figure 4.25c.

4.4.3.7 Plasmon Tuning and Local Field Enhancement Maximization of the Nanocrescent

A parametric study was conducted in [67] to show the high degree of tunability of the spherical crescent antenna when its various parameters are varied. The parameters studied include the outer radius, r_o, inner radius, r_i, center-to-center distance between r_o and r_i, d, angle of incident field, θ, and tip radius, s. The study results indicated that increasing the outer radius, r_o, or decreasing the center to center distance, d, resulted in red-shifting of the resonant peak. Varying the inner radius, r_i, or tip radius had very little effect on the resonance wavelength. Decreasing the tip radius, however, resulted in a significant

increase in field enhancement. The relationship between tip radius, s, and field enhancement, $|E|_{max}/|E_i|$, was observed to follow the expression $|E|_{max}/|E_i| = a + bs^{-1/2}$ where a and b depend on wavelength and geometry. Finally, variation of the incident angle resulted in splitting of the resonance peak between θ equal to 90 degrees and 135 degrees.

4.4.4 Mid-IR

4.4.4.1 Mid-Infrared Localized Plasmons Through Structural Control of Gold and Silver Nanocrescents

Gold and silver crescents with diameters larger than 500 nm were observed to support plasmonic resonances into the mid-IR. In theory, expanding resonances into the infrared can be accomplished by scaling up the dimensions of plasmonic structures. It has been observed, however, that as the dimensions of structures are increased, the localized plasmonic response is lost. Structures capable of maintaining nanoscale features, such as nanorods with microscale lengths and nanoscale widths, can still support LSPR response into longer wavelength ranges. Fabrication of nanocrescents has the unique property that their diameter and width can be controlled independently. The diameter/length of the crescent can be made arbitrarily large by using larger beads while the width can be controlled by adjusting the deposition angle. This results in crescent antennas with micrometer lengths and nanometer widths that can still support plasmonic resonances in the mid-infrared. Additionally, narrowing of geometrical features at the tips results in higher field intensities as compared to nanorods and asymmetry that leads to higher order modes. Figure 4.26e shows one such structure with a crescent diameter of 1.10 μm,

thickness of 50 nm, and a backbone width of 365 nm. Figure 4.26a shows the simulated extinction spectra, and Figure 4.26b shows the measured data. The simulated field distributions for long and short axis polarized sources are shown in Figure 4.26 c and d, respectively, confirming high field localization for these large structures.

Experimentally, gold crescent antennas with diameters of 2.05 μm and backbone widths of 470 nm fabricated on CaF substrates show a long axis dipole resonance at 7.68 μm and corresponding short axis dipole resonance at 3.84 μm. Similarly, measurements on silver crescent antennas with diameters of 2 um and widths of 425 nm show a long and short axis dipole resonance of 7.48 μm and 3.78 μm, respectively. Extrapolation of measured resonances for crescents of different diameters stipulates a long axis dipole resonance of 11.13 μm for gold crescents of 3.25 μm and width of 674 nm. Similar extrapolation of silver crescents estimates a long axis resonance of 10.82 μm for crescents with 3.13 μm diameter and 650 nm backbone width. Figure 4.27 a and b show measured resonances for crescents with different diameters and the extrapolation of these data into the mid-IR.

4.4.5 Microwaves

4.4.5.1 A Printed Crescent Patch Antenna for Ultrawideband Applications

A patch crescent antenna formed by a circle slot cut out of an ellipse is discussed in [69]. The antenna is desgned for ultrawideband operation between 3 GHz and 10 GHz. The antenna is shown in Figure 4.28. The tips of the crescent are connected, and a ground plane was provided for the matching microstrip line only. The antenna was printed on an

FR4 substrate with ε_r = 4.2, and copper was used for all the conductive elements. The design was based on the observation that currents mainly flow along the perimeter of an elliptical patch antenna. Carving an elliptical (or circular) slot with radii r1 and r2 introduces an additional resonance above 6 GHz (in comparison with the elliptical patch) when the radius is larger than 7 mm as shown in Figure 4.29a. The perimeter of the hole governs the resonant frequency, since the current flows mainly along its periphery. A larger hole corresponds to a longer current path and in turn a longer equivalent monopole wire and therefore a lower resonant frequency. Measured and simulated radiation patterns for co- and cross-polariztion in the E(yz)-plane is shown in Figure 4.29b. The pattern resembles the omnidirectional pattern of a dipole antenna up to 8 GHz. Higher order current modes result in a more directional antenna at frequencies higher that 8 GHz.

4.4.5.2 Design of the Crescent-Shape Planar Ultrawideband Antenna with a Band-notch Structure

A crescent antenna for ultrawideband applications (3.1–10.6 GHz) with a built-in notch filter to avoid interference between 5 GHz and 6 GHz is proposed in [72]. An initial design (antenna 1) without the notch filter is shown in Figure 4.30a. It consists of an ellipse with a circular cut-out. A trapezoidal backplane is provided for the microstrip feed line. The antenna with the notch filter (antenna 2) is shown in Figure 4.30b. The filter consists of a slot carved out of the backbone of the crescent. The VSWR for the antennas is shown in Figure 4.31. It can be seen from the graph that the introduction of the notch filter in antenna 2 results in an increased in the VSWR between 5 GHz and 6 GHz causing the antenna to block this band of frequencies. The current distributions

below (3.1 GHz), within (5.5 GHz) and above (9.0 GHz) the desired blocked frequency range is shown in Figure 4.32. The figure shows that at 5.5 GHz, strong currents flow all around the notch filter. At 3.1 GHz and 9.0 GHz currents flow more along the edges of the crescent antenna.

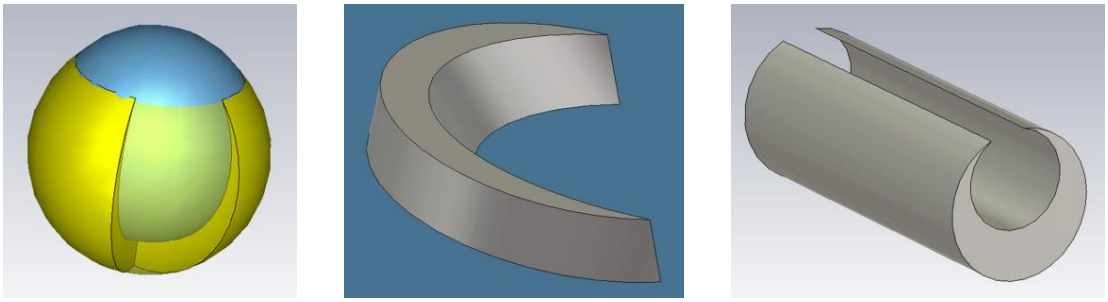

(a) (b) (c)

Figure 4.1. Crescent types. a) Spherical crescent. b) Planar crescent. c) Cylindrical crescent.

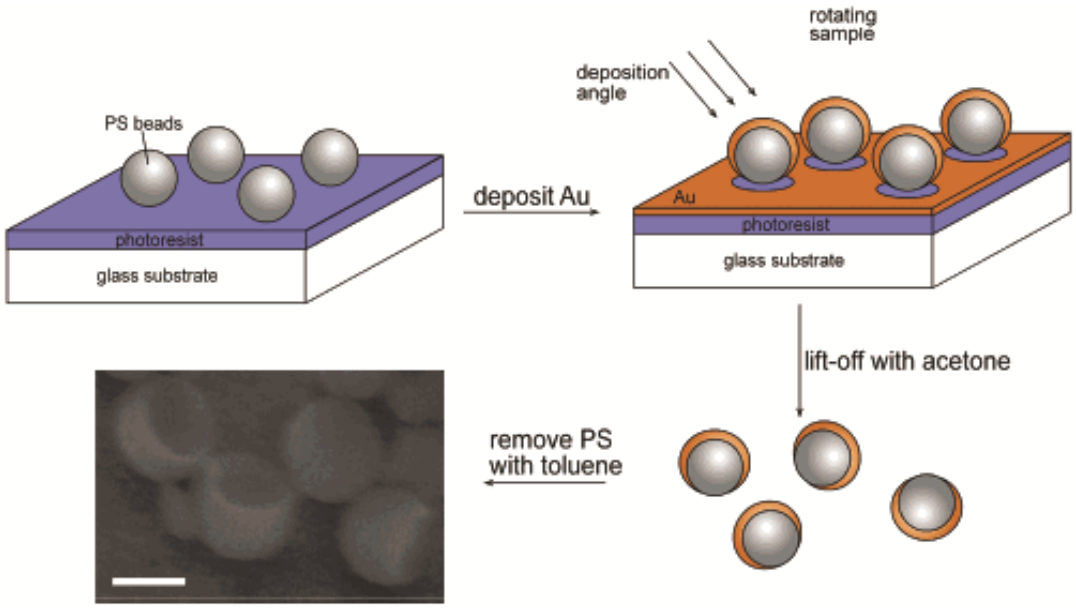

Figure 4.2. Fabrication procedure of spherical nanocrescents. Reprinted with permission from Y. Lu, G. L. Liu, J. Kim, Y. Mejia, and L. P. Lee, "Nanophotonic crescent moon structures with sharp edge for ultrasensitive biomolecular detection by local electromagnetic field enhancement effect," *Nano Lett.*, vol. 5, no. 1, pp. 119–124, Jan. 2005. Copyright 2005, American Chemical Society.

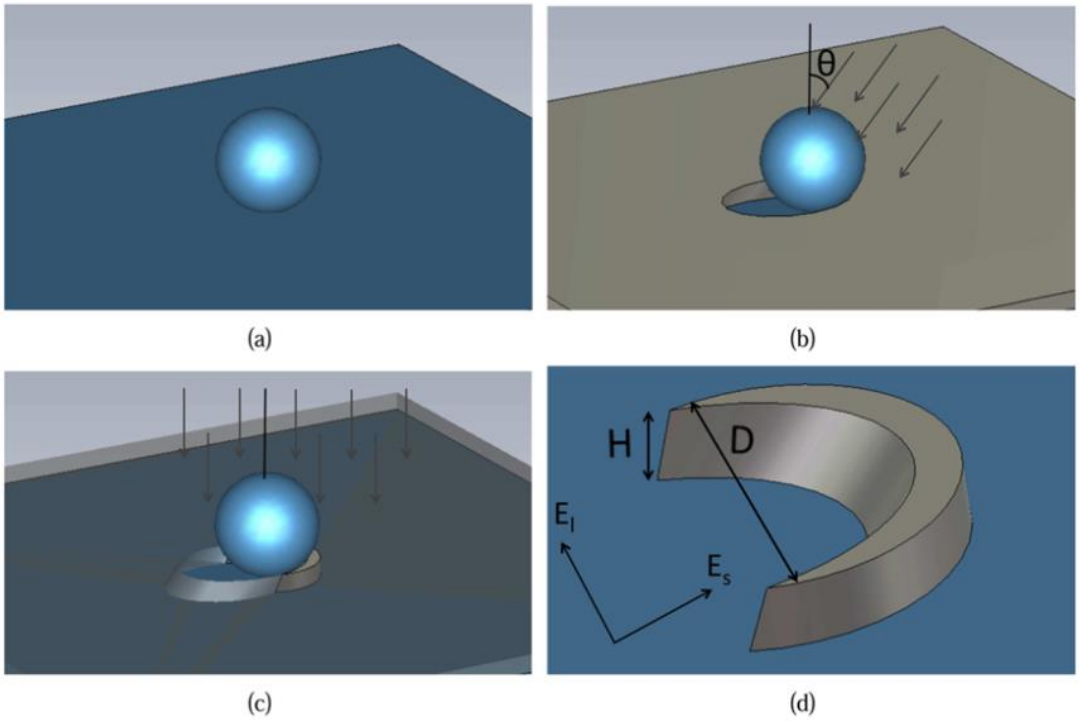

Figure 4.3. Nanosphere Template Lithography method for fabrication of planar crescent antennas. a) Polystyrene beads are deposited on a substrate. b) A layer of metal is deposited at a desired angle. c) Etching is done normal to the substrate and the bead acts to protect the metal beneath it. d) The bead is lifted off, leaving a crescent-shaped antenna. Reprinted with permission from M. Rodriguez, C. Furse, J. S. Shumaker-Parry, and S. Blair, "Scaling the response of nanocrescent antennas into the ultraviolet," *ACS Photon.*, pp. 496–506, May, 2014. Copyright 2014, American Chemical Society.

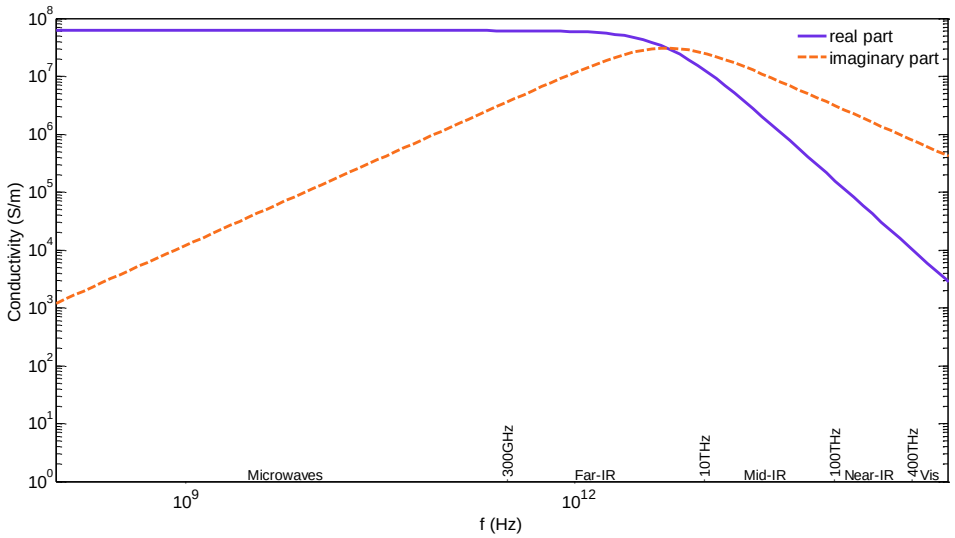

Figure 4.4. Real and imaginary part of the conductivity of silver based on the Drude Model.

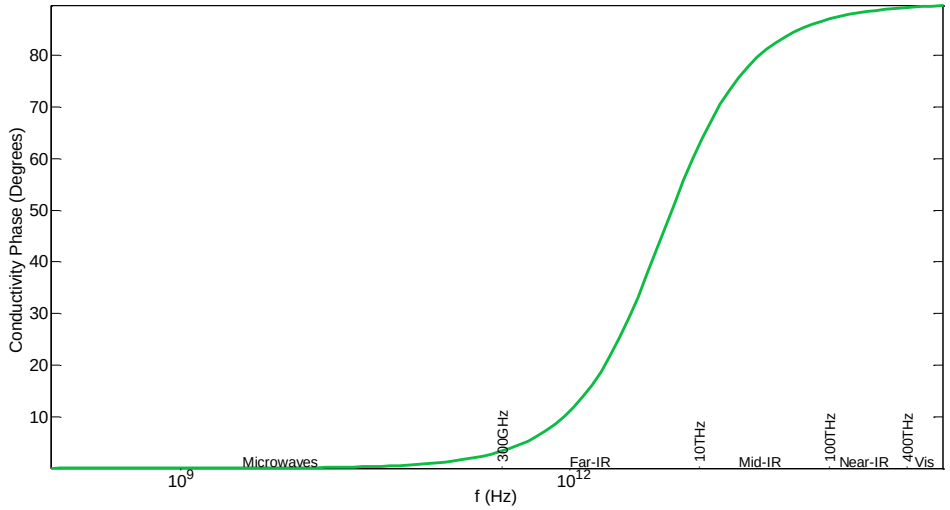

Figure 4.5. Phase of the conductivity of silver.

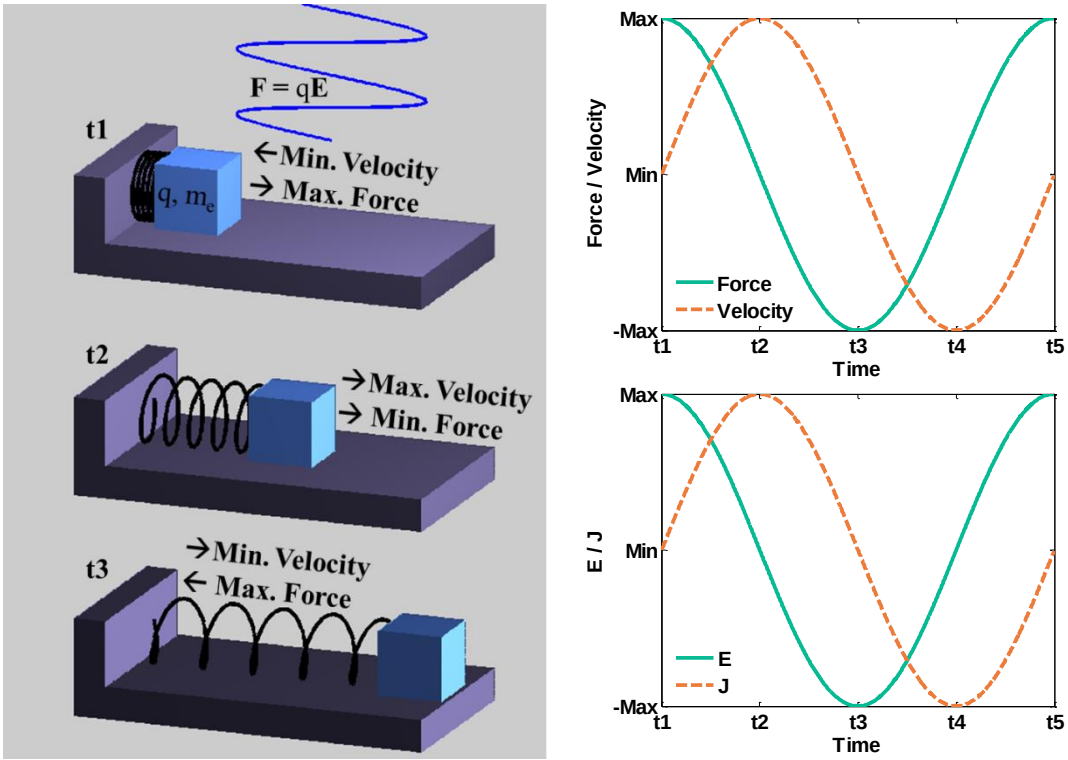

(a) (b)

Figure 4.6. Mass-spring model of plasmonic resonances. a) A mass representing a moving electron cloud in metals oscillates out of phase with the force representing incident electric fields. b) Out of phase relationship between the velocity and force in the mechanical model (top) and the resulting out of phase relationship in electrical parameters (bottom).

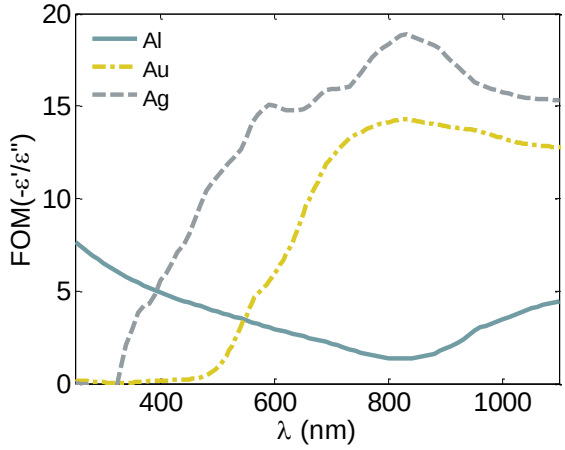

Figure 4.7. Figure of merit of aluminum, gold, and silver at ultraviolet, visible, and near-infrared wavelengths.

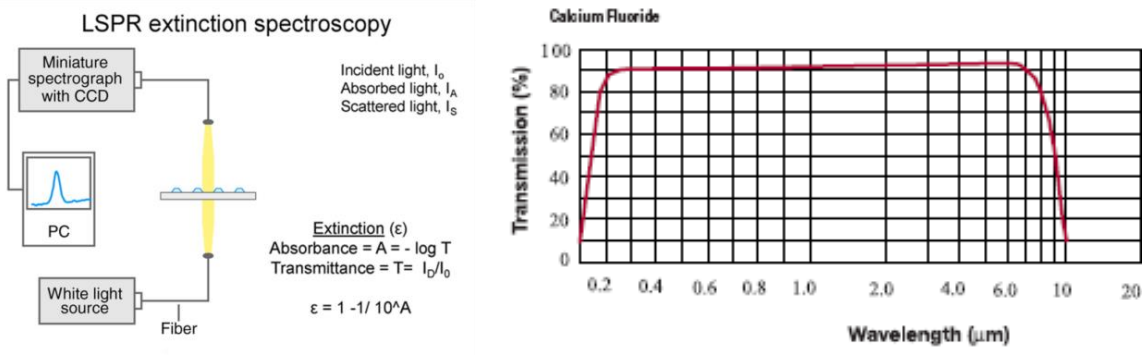

(a) (b)

Figure 4.8. Measurement of optical antennas. a) Localized Surface Plasmon Resonance spectroscopy measurement setup. Adapted with permission from [27]. Copyright 2007, Annual Reviews. b) Transmission window of CaF_2 substrate. Reprinted with permission from OptoCity, "CaF2 Crystal," http://www.optocity.com/CaF2.htm.

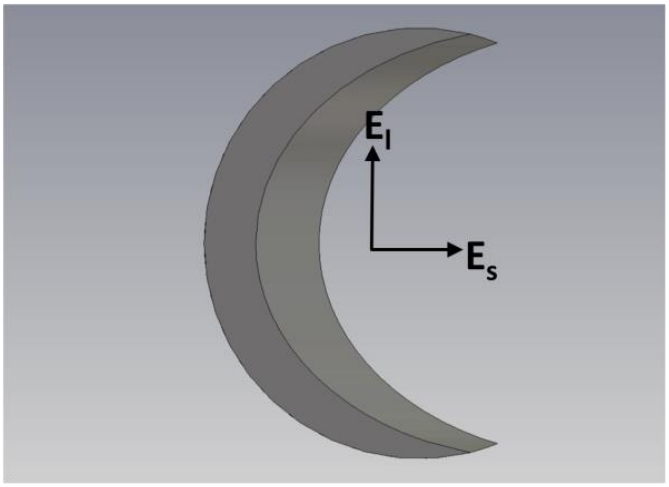

Figure 4.9. Definition of short, E_s, and long, E_l, axis polarized sources with respect to a planar crescent antenna.

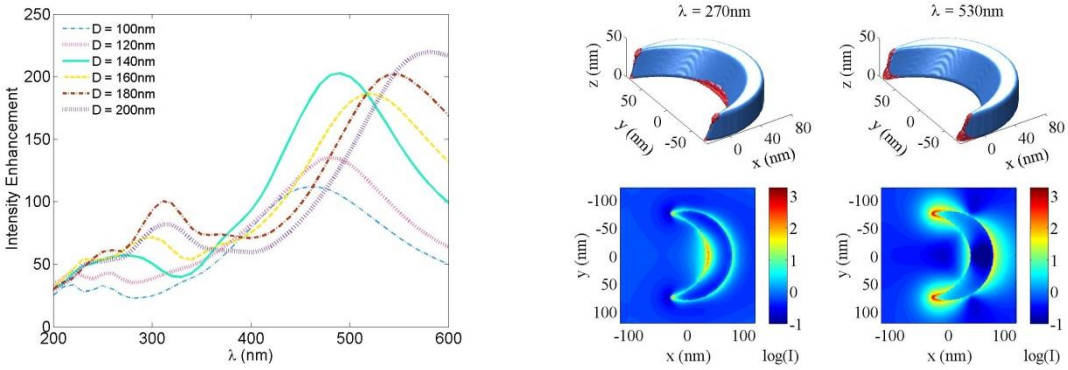

(a) (b)

Figure 4.10. Resonance response of aluminum crescent nanoantennas. a) Near-Field response of planar crescent antennas with a height of 50 nm when excited by a short axis polarized source. b) 3-D and 2-D intensity distributions of crescent with diameter of 160 nm and height of 30 nm at λ = 270 nm and 530 nm resonances. Reprinted with permission from M. Rodriguez, C. Furse, J. S. Shumaker-Parry, and S. Blair, "Scaling the response of nanocrescent antennas into the ultraviolet," *ACS Photon.*, pp. 496–506, May, 2014. Copyright 2014, American Chemical Society.

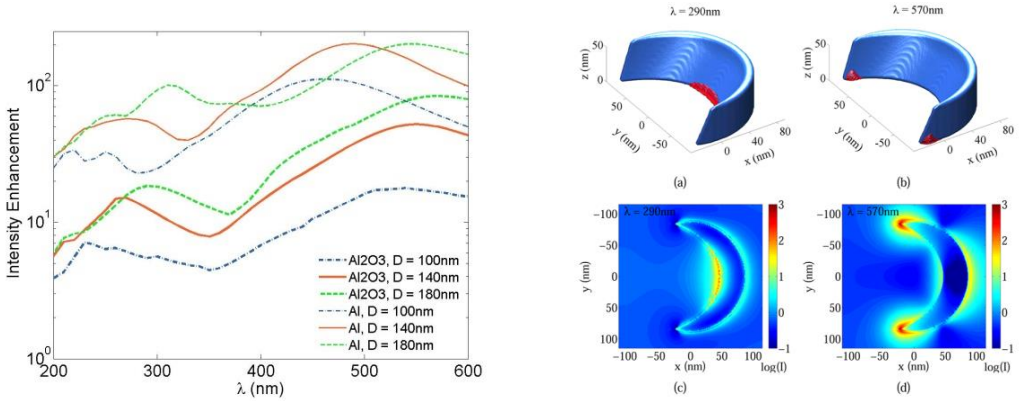

(a) (b)

Figure 4.11. Near-field response of antennas including a 3 nm oxide shell (Al2O3). a) Comparison in near-field response for antennas with and without an Al2O3 layer. b) 3-D and 2-D intensity distribution for antennas with diameter of 180 nm and height of 50 nm at λ = 290 nm and 570 nm resonances. Reprinted with permission from M. Rodriguez, C. Furse, J. S. Shumaker-Parry, and S. Blair, "Scaling the response of nanocrescent antennas into the ultraviolet," *ACS Photon.*, pp. 496–506, May, 2014. Copyright 2014, American Chemical Society.

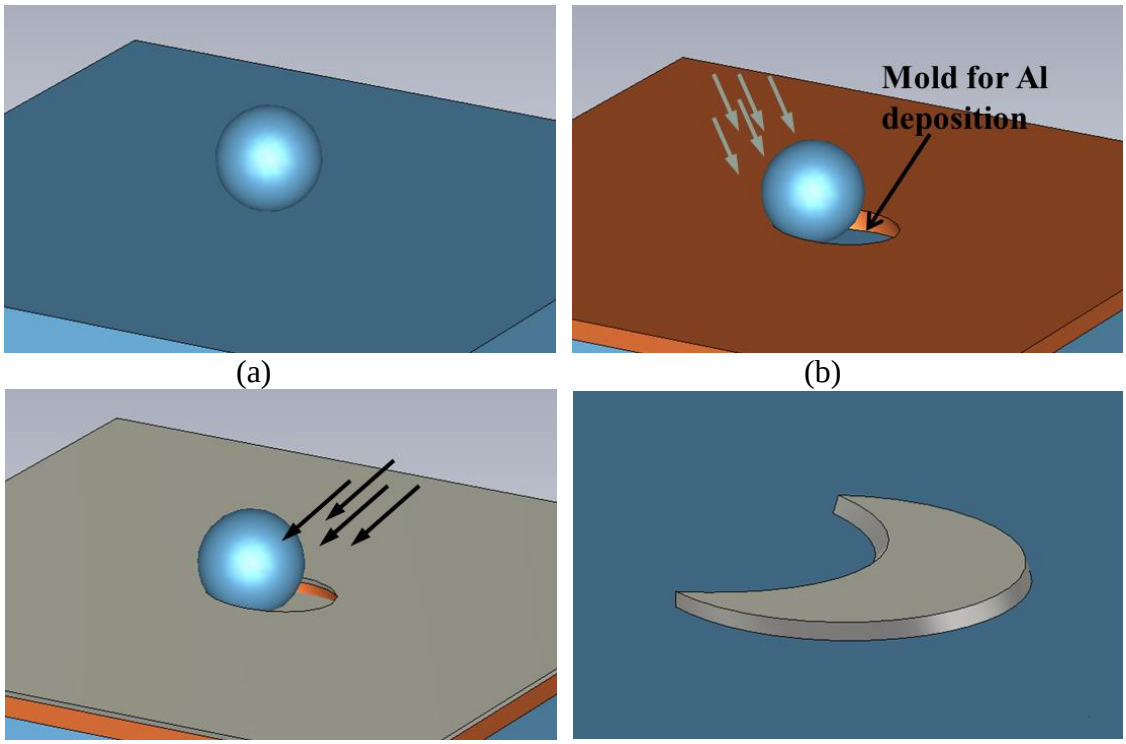

Figure 4.12. Fabrication of aluminum nanocrescent antennas using modified nanosphere template lithography. a) The process begins by depositing beads on a substrate. b) A layer of copper is then deposited at a desired angle to create a mold at the opposite side. c) This is followed by deposition of aluminum on the side of the mold. d) Copper is dissolved using nitric acid and excess aluminum on top of the copper is removed by sonicating substrate in nanopure water, leaving a crescent-shaped nanoantenna.

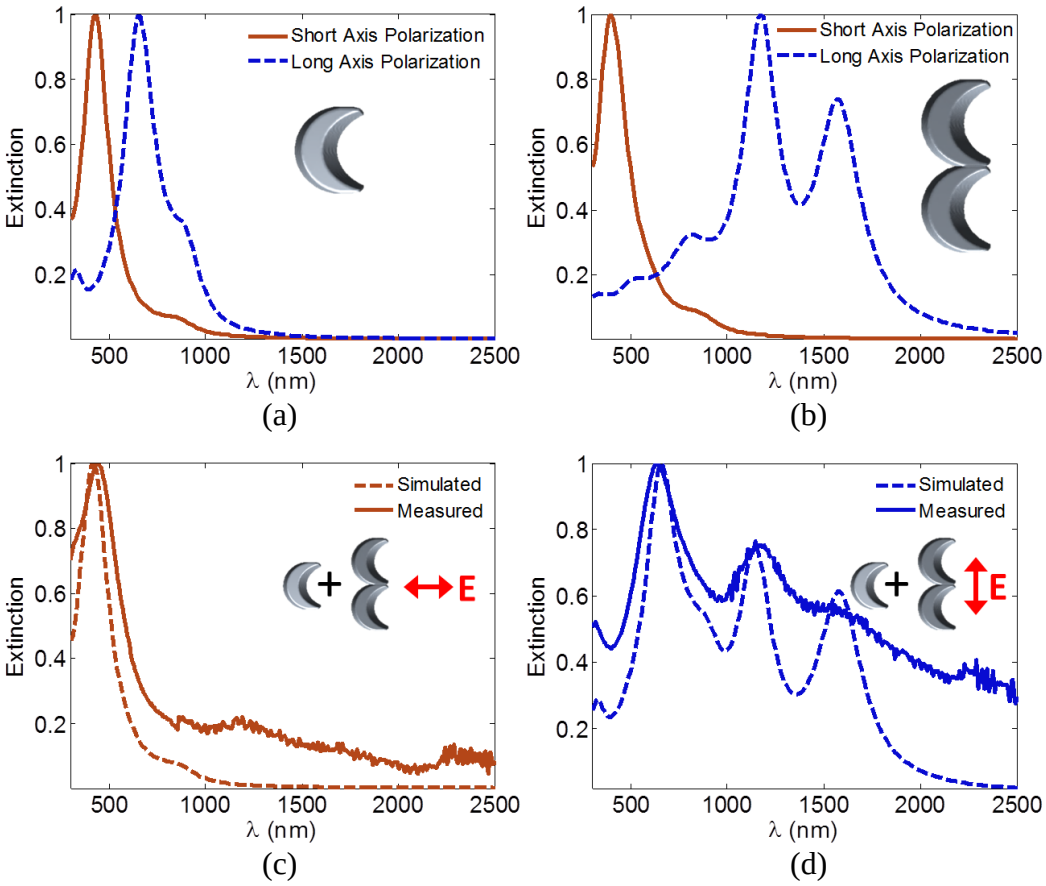

Figure 4.13. Measured and simulated response of aluminum crescent nanoantennas. a) Simulated extinction spectra of isoltated crescent antennas. b) Simulated extinction spectra of dimers. c) Comparison between measured and simulated responses of combined single and dimer crescents under short axis excitation. d) Comparison between measured and simulated responses of combined single and dimer crescents under long axis excitation.

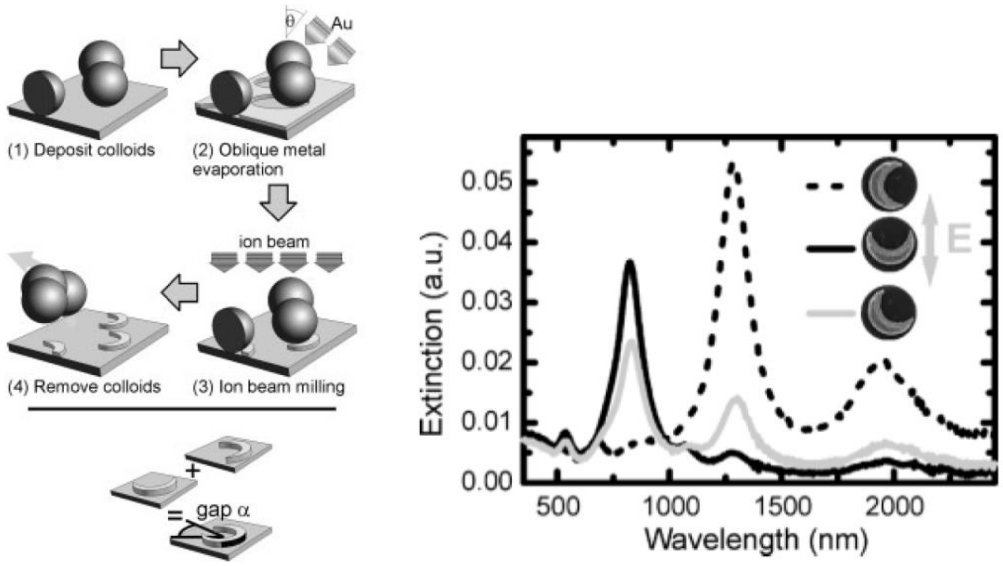

(a) (b)

Figure 4.14. Planar crescent nanoantennas. a) Fabrication scheme of planar crescent antennas using nanosphere template lithography. b) Extinction spectra for illuminating light at different angles of polarization with respect to the antenna. Reprinted with permission from [52]. Copyright 2005, WILEY-VCH Verlag GmbH & Co. KGaA, Weinheim.

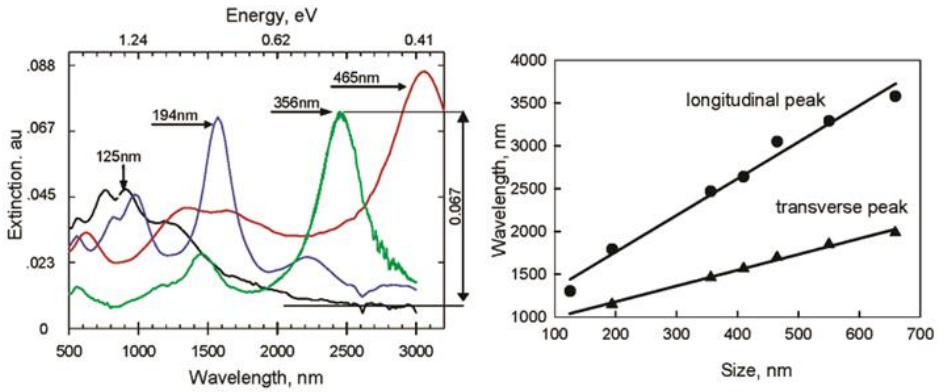

(a) (b)

Figure 4.15. Size-dependent nanocrescent LSPR properties. a) Extinction spectra for gold nanocrescent antennas of different diameters. b) Linear dependence LSPR peaks on the diameter of the nanocrescents. Reprinted with permission from R. Bukasov and J. S. Shumaker-Parry, "Highly tunable infrared extinction properties of gold nanocrescents," *Nano Lett.*, vol. 7, no. 5, pp. 1113–1118, May 2007. Copyright 2007, American Chemical Society.

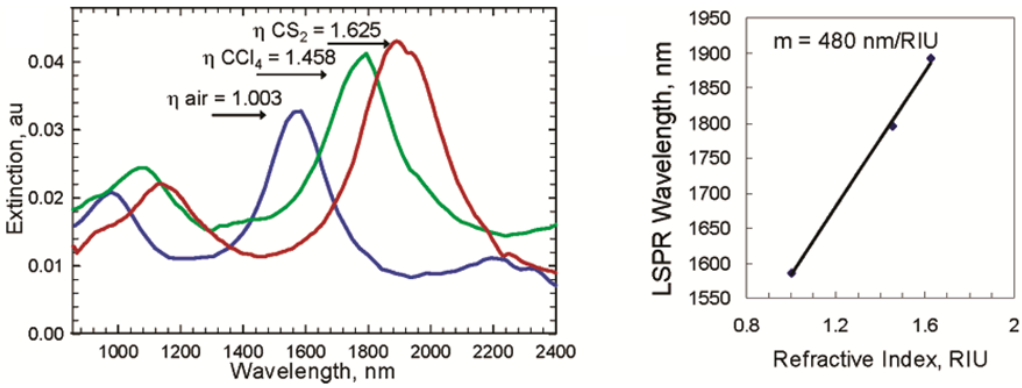

(a) (b)

Figure 4.16. LSPR sensitivity to the local dielectric environment. a) Resonance peaks are observed to red-shift as the refractive index of the dielectric environment increases. b) The LSPR for the nanocrescents is the sensitivity to dielectric environment is equal to the value of the slope. Reprinted with permission from R. Bukasov and J. S. Shumaker-Parry, "Highly tunable infrared extinction properties of gold nanocrescents," *Nano Lett.*, vol. 7, no. 5, pp. 1113–1118, May 2007. Copyright 2007, American Chemical Society.

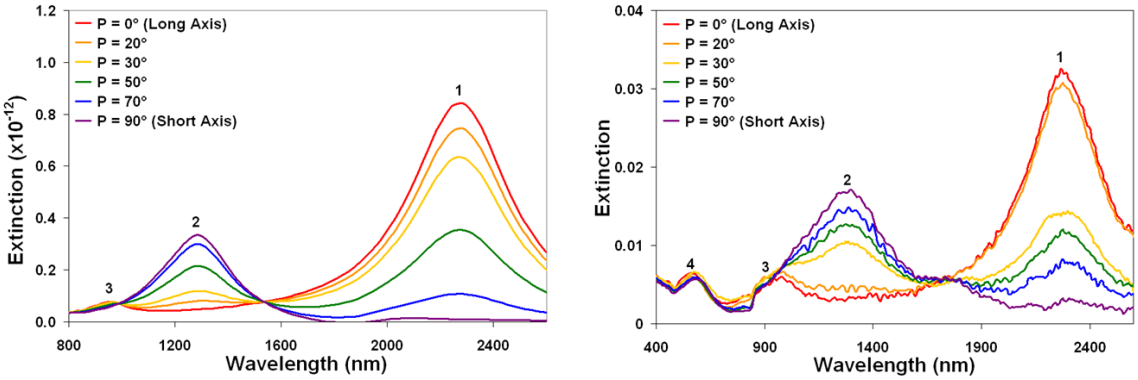

(a) (b)

Figure 4.17. Extinction spectra for gold nanocrescent antennas with a diameter of 356 nm as the polarization of incident light is rotated. a) Simulated results. b) Measured results. Reprinted with permission from C. T. Cooper, M. Rodriguez, S. Blair, J. S. Shumaker-Parry, "Polarization anisotropy of multiple localized plasmon resonance modes in noble metal nanocrescents," *J. of Phys. Chem.*, pp. 1167–1173, 2014. Copyright 2014, American Chemical Society.

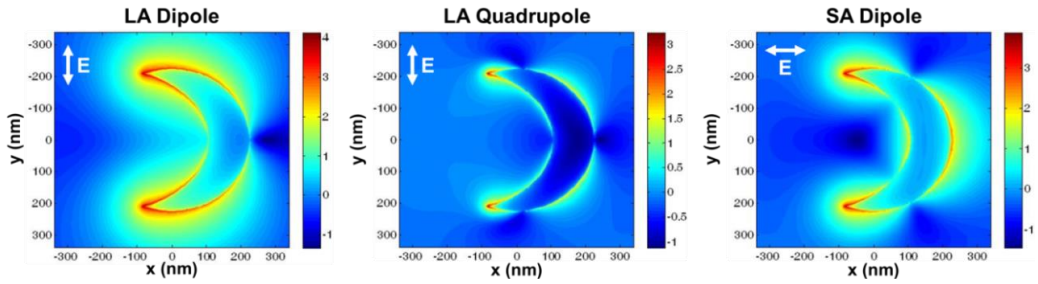

(a) (b) (c)

Figure 4.18. Calculated intensity maps of 356 nm diameter gold nanocrescents at a) long axis dipole resonance, b) long axis quadrupole resonance, and c) short axis dipole resonance. Reprinted with permission from C. T. Cooper, M. Rodriguez, S. Blair, J. S. Shumaker-Parry, "Polarization anisotropy of multiple localized plasmon resonance modes in noble metal nanocrescents," *J. of Phys. Chem.*, pp. 1167–1173, 2014. Copyright 2014, American Chemical Society.

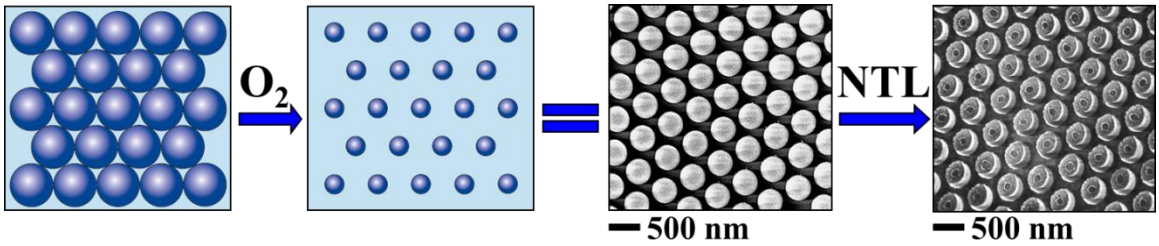

Figure 4.19. Fabrication process of nanocrescent antennas using modified nanosphere template lithography. Credit to Dr. Cindy T. Cooper.

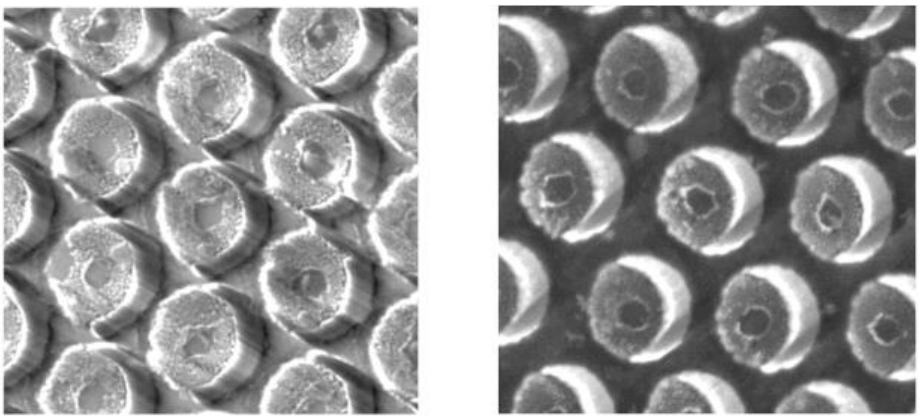

(a) (b)

Figure 4.20. Observed crescent orientations in fabricated hexagonal arrays. Credit to Dr. Cindy T. Cooper.

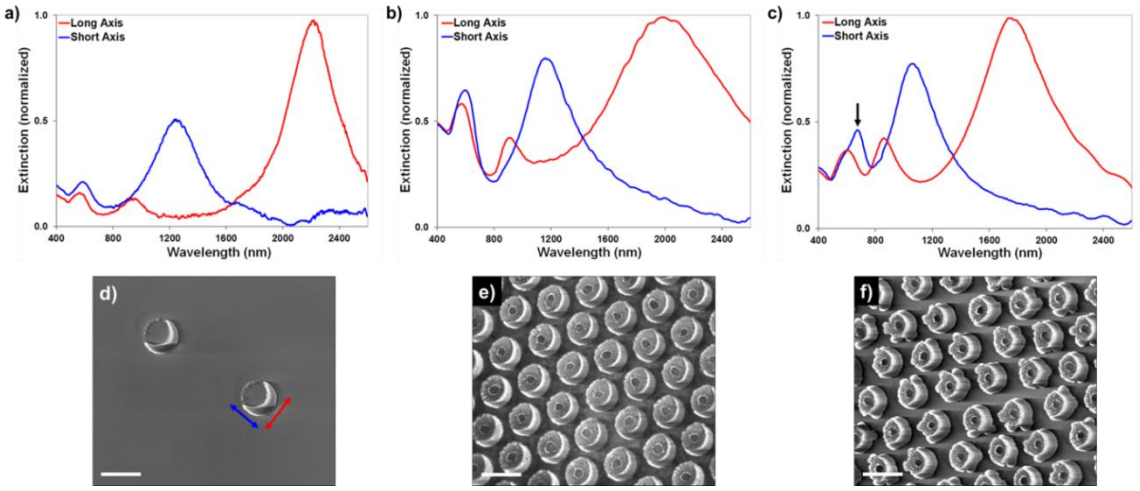

Figure 4.21. Extinction spectra of isolated (a) and arrayed (b, c) gold nanocrescents with final diameters of a) 440 nm, b) 410 nm, and c) 400 nm. Electric field polarized across long axis (red spectra) and short axis (blue spectra) with corresponding SEM images below (scale bars = 1 μm). Array samples were fabricated from 505 nm beads etched at 100 W for 120 s (b) and 160 s (c). Black arrow in c indicates new short axis quadrupole peak. Credit to Dr. Cindy T. Cooper

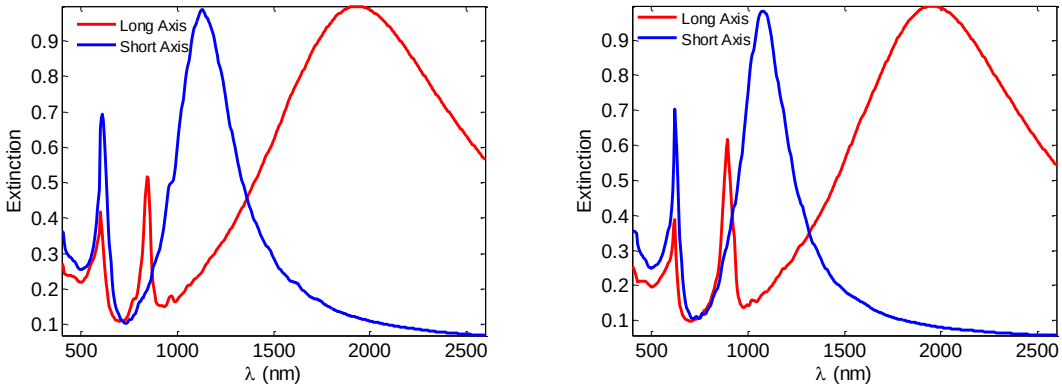

Figure 4.22. Simulated extinction spectra for crescents arranged in configuration of a) Figure 4.20a and b) Figure 4.20b.

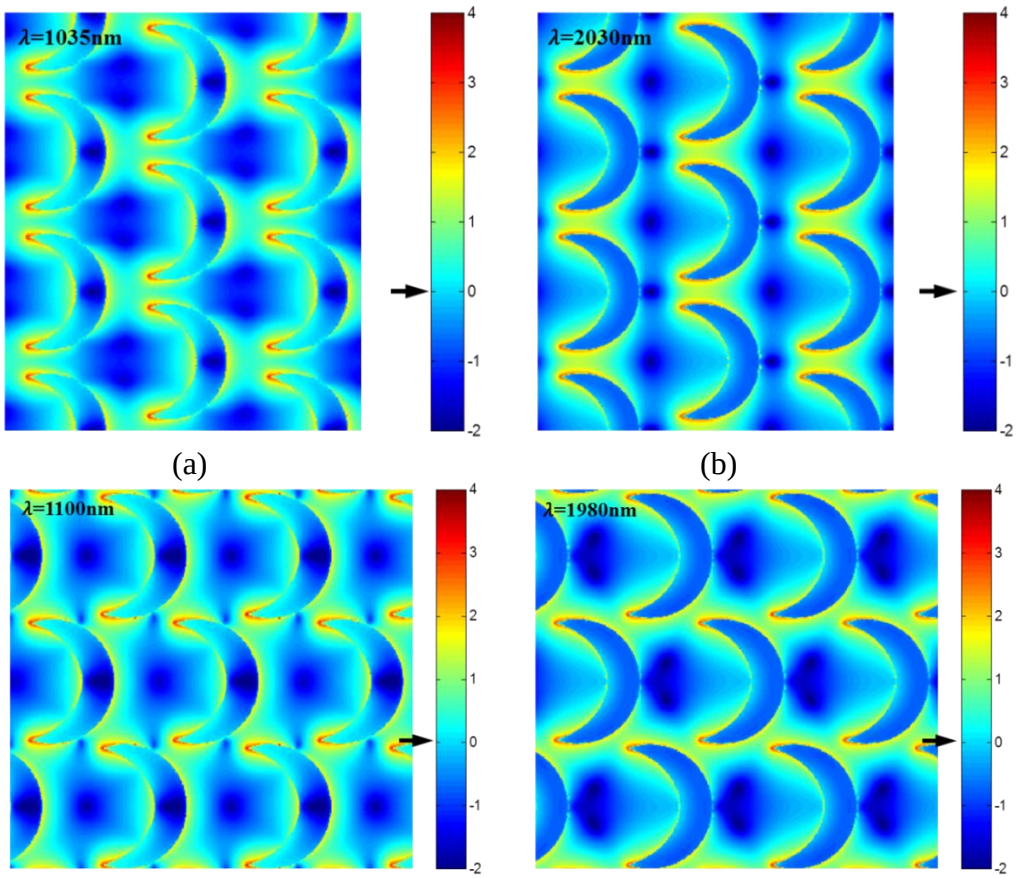

Figure 4.23. Simulated field patterns for hexagonal crescent arrays. Note that the arrangement of crescents in a and b is different from that in c and d. a) Field intensity distribution at short axis resonance. b) Field intensity distribution at long axis resonance. c) Field intensity distribution at short axis resonance. d) Field intensity distribution at long axis resonance.

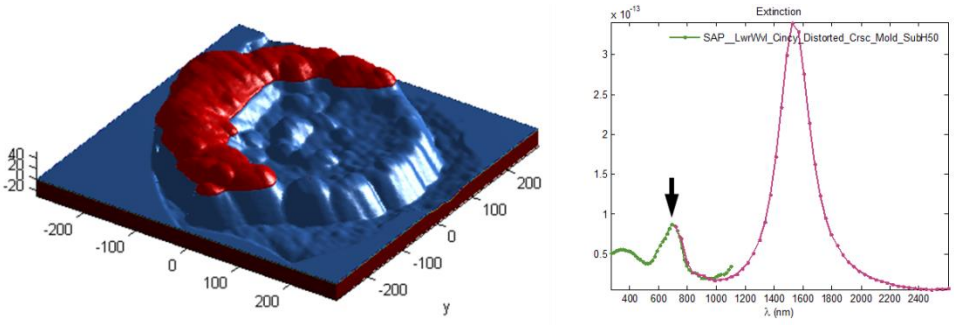

Figure 4.24. Simulated AFM image of crescent nanoantenna. a) Distorted crescent antenna image imported into simulation program. b) Resulting extinction spectrum when illuminated with a short axis polarized source.

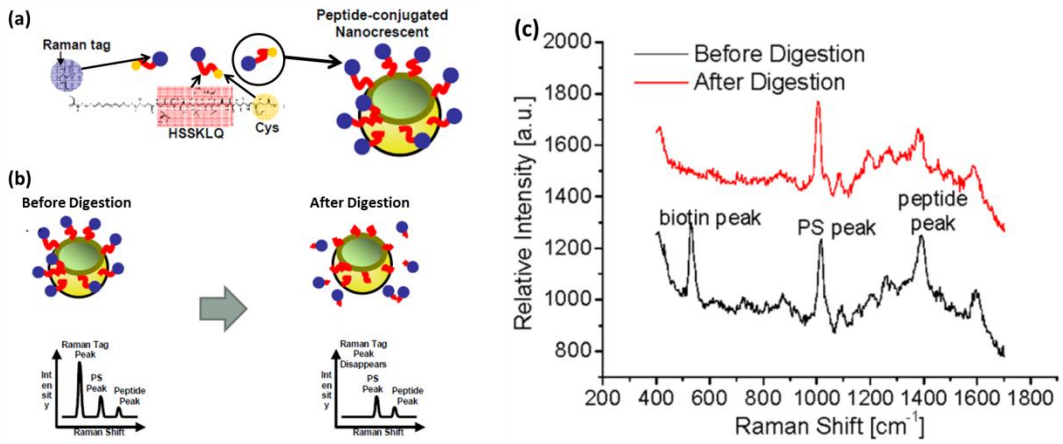

Figure 4.25. Cancer detection using spherical nanocrescent antennas. a) Schematic showing the tagging of spherical nanocrescents with specially designed peptides for cancer detection. b) Before digestion, the Raman tag shows a strong resonance due to its vicinity to the tip of the crescent. After exposure of the setup to PSA, the HSSKLQ portion of the peptide is digested, dislocating the Raman tags and eliminating the Raman resonance peak from the spectrum. c) Experimental results showing the disappearance of the Raman tag (biotin) resonance peak after digestion. Reprinted with permission from [65]. Figure adapted from [65]. © Copyright 2006, IEEE.

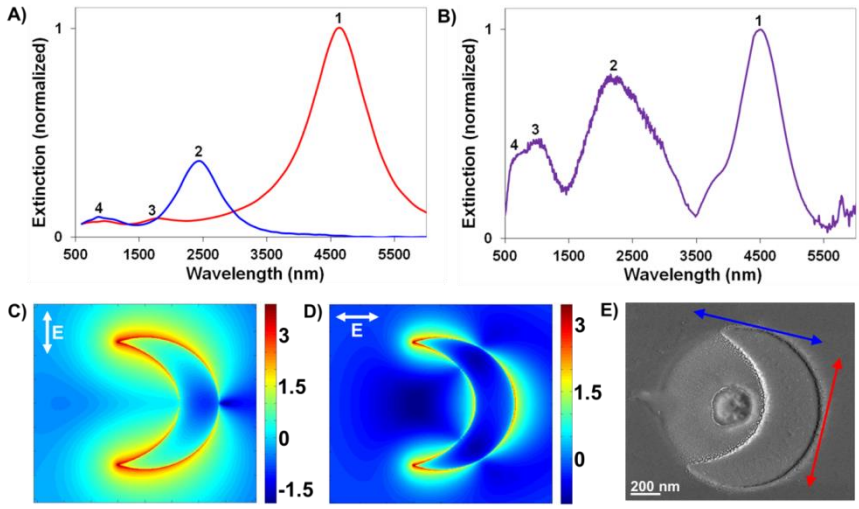

Figure 4.26. Response of 1.10 μm diameter gold crescent antenna. a) Simulated extinction spectrum. b) Unpolarized measured extinction spectrum. Calculated intensity distribution at c) long axis dipole resonance and d) short axis dipole resonance. e) Electron micrograph of fabricated crescent antenna. Credit to Dr. Cindy T. Cooper.

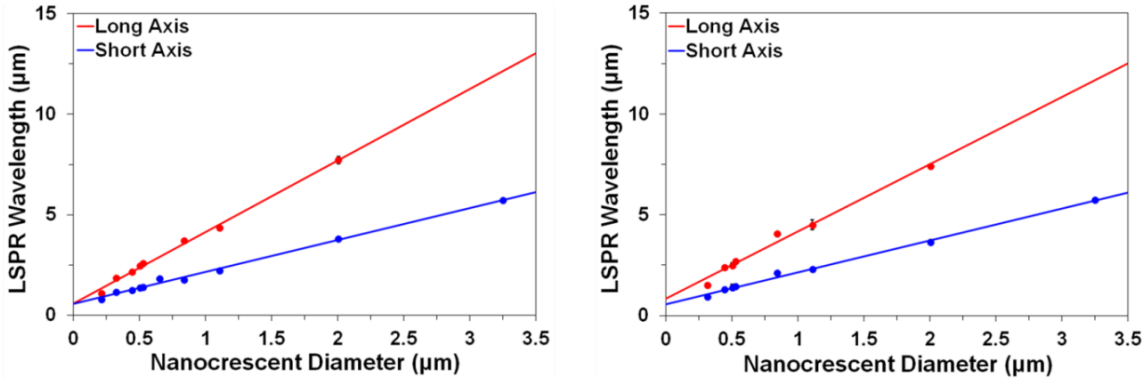

Figure 4.27. Relationship of polarization dependent plasmon resonance wavelengths for a) gold nanocrescents and b) silver nanocrescents over a broad size range demonstrating a high degree of LSPR wavelength tunability. Credit to Dr. Cindy T. Cooper

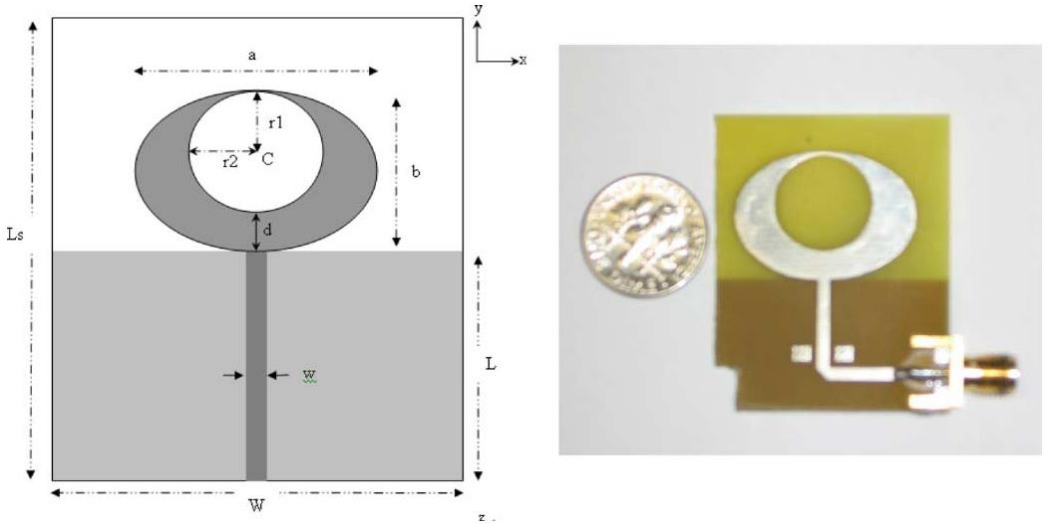

Figure 4.28. Antenna structure and photograph of a crescent-shaped patch antenna. Reprinted with permission from [69]. © 2007, IEEE.

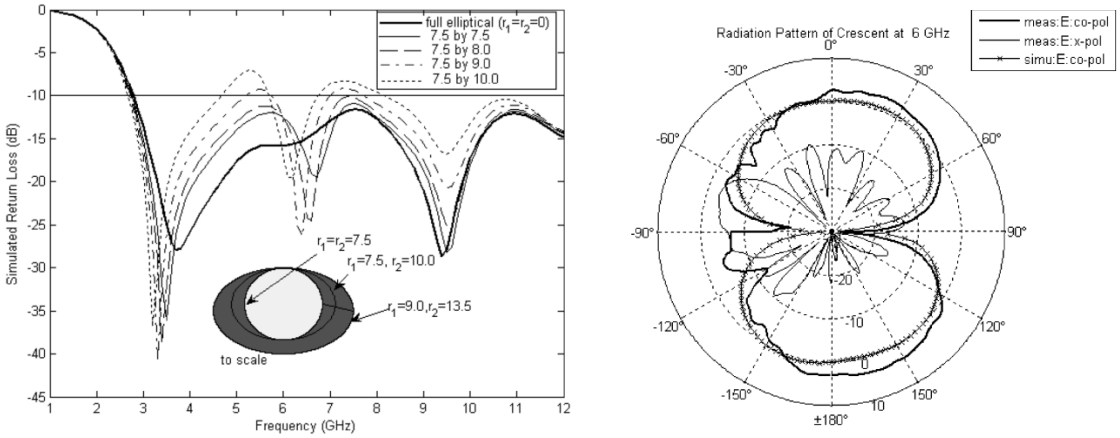

(a) (b)

Figure 4.29. RF crescent antenna investigation. a) Parametric studies of effect of r1 and r2 on the return loss of crescent antenna. b) Measured and simulated radiation patterns of a crescent antenna at 6GHz. Reprinted with permission from [69]. © 2007, IEEE.

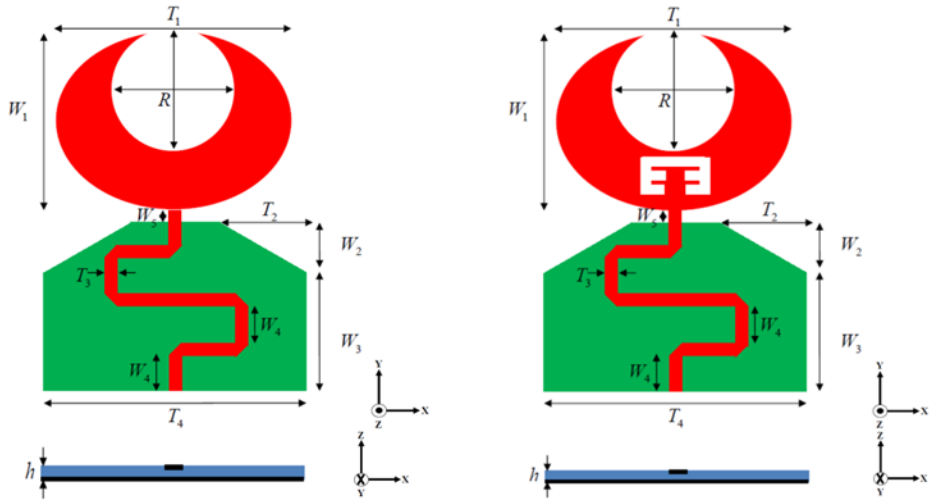

(a) (b)

Figure 4.30. RF crescent antennas designed for wideband applications. a) Crescent antenna 1 without notch filter. b) Crescent antenna 2 with notch filter incorporated at backbone. Reprinted with permission from [72]. © 2007, IEEE.

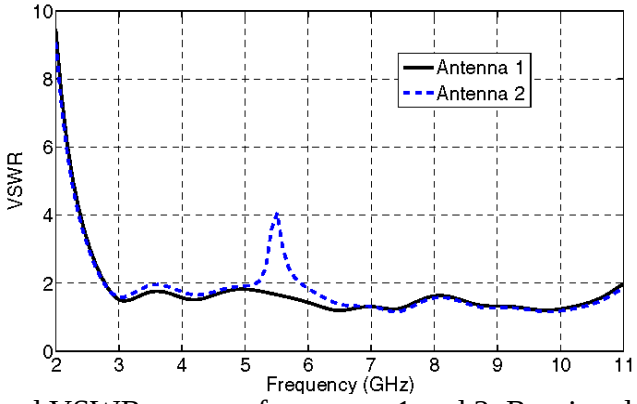

Figure 4.31. Simulated VSWR curves of antennas 1 and 2. Reprinted with permission from [72]. © 2007, IEEE.

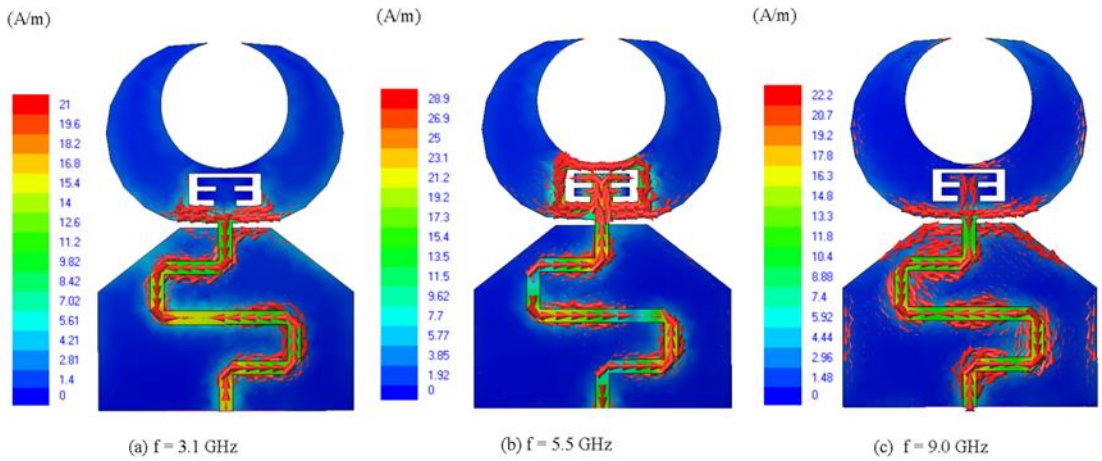

Figure 4.32. Simulated surface current distributions of the proposed antenna 2 a) at 3.1GHz, b) 5.5GHz, and c) 9.0GHz. Reprinted with permission from [72]. © 2007, IEEE.

CHAPTER 5

SCALING THE RESPONSE OF NANOCRESCENT ANTENNAS INTO THE ULTRAVIOLET[1]

5.1 Abstract

Fundamental resonance modes of nanocrescent optical antennas are associated with large electric fields at the crescent tips. These antennas have been extensively studied due to their relative ease of fabrication and tunable response via methods such as nanosphere template lithography. To date, investigations have only been performed in the visible to mid-infrared range, where the multimode anisotropic response has been documented both experimentally and through simulations. However, the presence of interband transitions in the dielectric response of the metals used for these studies complicates the analysis of the higher-order resonance modes. In this paper, we perform a comprehensive investigation of the electromagnetic response of aluminum nanocrescent antennas. Aluminum has an interband transition in the near-infrared, which facilitates scaling of the resonance modes into the ultraviolet part of the spectrum, thus allowing investigation of the higher-order modes of the nanocrescent structure. These higher-order modes exhibit intense and controllable hot spots, suggesting that nanocrescent antennas are suited for applications in the UV regime.

5.2 Introduction

Nanocrescent-shaped antennas have been widely studied [50], [51], [60], [81]. The high field-enhancement, combined with ease of fabrication [52], [82] and tunability [17], make these structures very promising for many applications. One of the challenges in scaling antenna resonances to short wavelengths is the dielectric response of the constituent metals. Gold and silver, for example, have interband transitions in the green and blue parts of the spectrum, respectively, and thus limit strong resonance response to longer wavelengths. Therefore, most studies to date of antenna response in the ultraviolet have employed other metals, such as aluminum [83]–[92]. Another significant issue in scaling antenna response to the ultraviolet range is the physical size of the antenna – the resonance wavelengths of the antenna generally scale with the antenna size [93], therefore requiring high-resolution patterning. An alternative is to utilize higher-order antenna modes, which are well-characterized for dipole [88], [94] and simple rod [93] [95] antennas.

Nanocrescent antennas exhibit a rich spectrum of anisotropic modes [11], which have only been studied in the visible to mid-infrared. These studies have been based on the use of gold or silver for the antenna, complicating the analysis of the structure of the higher-order modes as the resonance wavelengths of these modes approach the interband transition frequencies of the metals. Aluminum, by contrast, has an interband transition near 800 nm with a Drude-like free-electron response from the visible to UV wavelengths [96]. Even though other metal options exist for UV plasmonics [96]–[101], we use aluminum in part due to its compatibility with conventional semiconductor processing [93].

5.3 Simulation Model

Nanocrescent antennas are fabricated using nanosphere template lithography [52]. The process begins with placing polystyrene beads on a glass substrate to serve as a template for the crescent antennas as shown in Figure 5.1a. A metal layer is then deposited at a controlled angle, Figure 5.1b. The thickness can be controlled by adjusting deposition rate and time. The deposition angle is defined with respect to the normal to the substrate and can be used to control the top and bottom widths of the antenna. Increasing the deposition angle, for instance, results in a wider antenna at the base and narrower at the top. Deposition is followed by etching at a normal angle to the substrate, Figure 5.1c. The bead's shadow acts to protect the metal underneath so that only metal outside of this area is etched. The result is a crescent of height H and diameter D equal to the diameter of the bead used to create it. Finally, the beads are removed by tape-off, leaving only the crescents on the substrate, Figure 5.1d.

In this study, the nanocrescent response was obtained through simulation using Lumerical's FDTD Solutions, and all data processing was performed using Matlab R2009b. FDTD Solutions allows for objects to be constructed from Boolean combinations of simpler geometrical objects. A crescent on a substrate can be created by overlaying four shapes with priorities as indicated in Figure 5.2. The program interprets this as a substrate that overrides anything embedded within it since it has the highest priority. Similarly, a portion of the right cylinder is overridden by the sphere and tilted cylinder, resulting in a crescent shape.

The simulation model described above follows directly from the fabrication process, where the "shadow" of the bead prevents metal from depositing onto certain locations,

Figure 5.1b, and prevents metal from being removed during etching, Figure 5.1c. Following geometrical model definition, the structure is meshed. FDTD Solutions allows hexahedral meshes where the height, width, and length of the hexahedra can be independently defined. The grid resolution is a compromise between accuracy and computational expense. Crescents with diameters 80 nm and less were meshed at $0.5\times0.5\times0.5$ nm^3 in the x, y, and z directions. Crescents with larger diameters were meshed coarser at $1\times1\times1$ nm^3 in order to reduce simulation time and storage space.

After defining the mesh, the model was augmented with monitors to record near-field data or power flow for far field calculations. For near-field calculations, 3-D monitors were used to record electric field intensity. The volume occupied by these monitors is delineated by the yellow lines in Figure 5.3. The spatial locations where the electric field intensity and materials' properties are determined were also recorded in the monitors and have the same resolution as the enclosed mesh. For far field simulations, the 3-D monitor was replaced by six 2-D power flow monitors to determine absorption cross-section, and six additional power flow monitors enclosing the source were added to find the scattering cross-section.

A Total Field Scattered Field (TFSF) source was used for simulations. This type of source is used to simulate plane wave incidence on finite structures. This follows in line with experimental procedures where a nanocrescent is much smaller than the laser beam spot used to characterize it. In Figure 5.3 this is shown as the volume enclosed by gray lines. The incident direction of the source is indicated by the pink arrow and the electric field polarization by the blue arrows. Polarization can be defined for 360° around the incident axis. The two polarizations of interest are short axis (SA) polarization, E_s, and

long axis (LA) polarization, E_l, defined as fields polarized along the short and long axis of the crescent respectively. This is illustrated in Figure 5.1d.

After defining the source, the complete structure was enclosed by a simulation region. This region is shown enclosed by brown lines in Figure 5.3. This simulation region provides perfectly matched layers (PML) boundary conditions to absorb light incident upon it and avoid reflecting it back towards the structure being simulated. The near field response of each crescent was determined from simulations performed at discrete wavelengths in the range of 200 nm to 600 nm in increments of 10 nm and for each electric field polarization.

Simulation of crescents was followed by data extraction and analysis. As described in [102], data from power flow monitors located within and outside of the volume of the TFSF source was extracted to compute the absorption and scattering cross-section, respectively. The extinction cross-section is simply the sum of the two. Near-field data were analyzed by extracting the data from FDTD Solutions and analyzing it using Matlab. The field data values produced by the simulations are in reference to a unit source and therefore represent field enhancement. In order to better define the usefulness of the crescents, the fields were averaged over a small volume. Only fields in free space were considered for this analysis; fields inside materials were masked by using the index of refraction. In this study, a 1000 nm^3 amorphous volume following the highest field intensity around the crescent was used. For example, assuming a $1\times1\times1$ nm^3 mesh, each mesh point approximates the field intensity over the 1 nm^3 surrounding the point. In order to represent a 1000 nm^3 volume, 1000 mesh points are needed. This is true regardless of the arrangement of the points. Therefore, the 1000 highest field intensity values

(specified at 1000 mesh points) were averaged to determine the near field response. Due to the symmetry of the structure, only one half of the crescent was analyzed, as shown in Figure 5.4. The near-field response at the tips was determined by averaging the highest field intensity points in region I of Figure 5.4. The dividing plane between tip and backbone was selected to be 85° from the xz-plane. Similarly, the near-field response at the backbone was determined by averaging the highest field intensity points in region II. The overall crescent response was obtained by averaging over regions I and II combined.

5.4 Results

The resulting intensity response in each region for a crescent 160 nm in diameter and 30 nm in height with a deposition angle of 40° and that was excited using a short-axis polarized source is shown in Figure 5.5a. The figure shows that the largest peak from the tip response and overall crescent response coincide (λ = 530 nm). At this wavelength, the tips produce the dominant contribution to the overall crescent response, as can be seen directly from Figure 5.5b. This peak is associated with the short-axis dipole resonance, and the wavelength at which it occurs is primarily affected by the diameter of the crescent. The figure shows an additional peak at λ = 270 nm. This peak has comparable contributions from both tip and backbone fields, and has a quadrupole character. In previous papers, this resonance has been denoted an "out-of-plane" resonance [11], which is descriptive based upon the charge oscillation along the edges of the tips (in the z-direction), resulting in two distinct hot spots at the corners of each tip. We further observe that the wavelength of this peak can be adjusted by changing the deposition angle (which changes the width of the backbone) in addition to the crescent diameter.

Similarly, for a long-axis polarized source, the tip, backbone, and overall responses of the nanocrescent are shown in Figure 5.6a. Excitation of the crescent with this polarization results in a dipole resonance (which lies outside the range of the graph, and is influenced by the interband transition of Al) and a quadrupole resonance (λ = 420 nm). Both of these resonances shift with the crescent diameter, while the quadrupole resonance is also affected by the backbone width. The enhancement spectrum also exhibits multiple higher-order antenna resonances, the dominant one located at λ = 220 nm, which shifts with the width of the crescent backbone. The near-field intensity patterns are illustrated in Figure 5.6b.

To further analyze the resonance modes of the crescent antenna, a parametric study was performed to determine the effects of diameter, height, and deposition angle. The crescent diameter was varied from 40 to 200 nm in increments of 20 nm, the crescent height was varied from 20 nm to half of the crescent diameter in increments of 10 nm, and the deposition angle was varied from 20^0 to 60^0 in increments of 10^0.

5.4.1 Scaling with Crescent Diameter

Figure 5.7 shows the crescent's response as the diameter varies. The results show that decreasing the diameter of the nanocrescent has the effect of blue shifting the dipole and quadrupole resonances, as expected. Figure 5.7a shows that when excited with a short-axis polarized source, the dipole resonance can be brought into the UV range by reducing the diameter to approximately 40 nm. For comparison, Figure 5.7d shows that while the long-axis dipole resonance lies outside the plotted wavelength range, the quadrupole resonance can be blue-shifted into the UV range with diameters less than approximately

120 nm when using a deposition angle of 40^0. Shift of the higher-order long-axis resonances as a function of diameter is also apparent, but the shift is more pronounced as a function of the deposition angle, as will be shown next.

5.4.2 Scaling with Deposition Angle

The backbone width of the crescent can be controlled by changing the deposition angle as described previously. The result of varying the deposition angle for short and long-axis polarized sources is shown in Figure 5.8 a and b, respectively. Figure 5.8a shows that as the deposition angle is increased, the short-axis dipole resonance does undergo some blueshift. A similar response is observed in Figure 5.8b for the long-axis quadrupole resonance, with the greatest change occurring between 20° and 30° deposition angles in both cases.

The behavior of the higher-order resonances in general is to redshift with increasing deposition angle, which follows intuition since the backbone width increases with angle. However, as the backbone width increases, the inner and outer path lengths along the crescent decrease and increase, respectively, to the point that the higher-order resonances undergo splitting, as shown prominently for the short-axis polarization at $\theta = 60°$. The local intensity patterns for these two modes are shown in Figure 5.9, showing that the shorter-wavelength mode has additional field nulls along the outside arc of the structure, Figure 5.9(a, d), as compared to uniform intensity in Figure 5.9e. Comparing Figure 5.9 and Figure 5.5, the short-axis dipole and quadrupole modes remain relatively unchanged.

Similar behavior is seen for the long-axis resonance in the emergence of an additional higher-order mode for deposition angles $\theta \geq 40°$. For $\theta = 60°$, the two near-field intensity

patterns are shown. At λ = 220 nm, Figure 5.10(a, d), the intensity pattern is similar to that in Figure 5.6 (λ = 220 nm); however, a new intensity pattern emerges at the λ = 290 nm resonance wavelength, with intensity more localized at the tips (b, e). The intensity pattern at the long-axis quadrupole resonance (c, f) at λ = 400 nm is unchanged compared to Figure 5.6 at λ = 420 nm.

5.4.3 Scaling with Crescent Height

Crescent height has little effect in shifting the resonant wavelengths, but can be used as an optimizing parameter for intensity enhancement. Figure 5.11a for instance shows the intensity enhancement dependence on crescent height when a crescent with a diameter of 140 nm and a deposition angle of 40° is illuminated with a short axis polarized source. The figure shows that a crescent height of 50 nm results in the strongest dipole resonance, while a height of 70 nm results in the strongest quadrupole resonance.

Figure 5.11b shows the response for a long axis polarized source. Although the dipole resonance for this incident polarization occurs at much longer wavelengths, the quadrupole occurs within the wavelength range of interest and is maximized with a height of 50 nm. The higher-order resonance at λ = 220 nm is maximized with a height of 60 nm.

5.4.4 Effect of Native Oxide Shell

Aluminum is an oxidizing metal, with the natural oxide thickness often quoted in the 2 to 3 nm range. The effect of this oxide layer on the plasmonic response of Al

nanostructures has been studied by a number of groups [85], [86], [103]. A significant conclusion from these studies is that the presence of the oxide layer dampens and red-shifts the plasmonic response, especially when that response is due to highly-localized fields, such as at tips or sharp corners. Aluminum oxide growth is self-terminating and is usually well-described by an inverse logarithmic law [104], [105] – based upon oxidation in an air environment at 295 K and 70% humidity, oxide thickness is about 2 nm after 24 hours and reaches a steady-state thickness of about 2.5 nm after 10 days [85], [106].

It is not always feasible to maintain Al samples in a reduced oxygen environment or to perform measurements before significant oxidation occurs. There are situations, however, in which neglecting the oxide layer, as represented by our results so far, may be a reasonable approximation. A number of surface passivation schemes have been developed that significantly reduce oxide growth, such as passivating with carboxylic acid [107], an epoxide group [108], or oleic acid [109]. Nevertheless, it is important to look at the effect of an oxide layer on nanocrescent antennas, as even a passivation process will produce a thin dielectric shell around the structure that could affect plasmonic response.

In the simulations to follow, the exposed surfaces of the nanocrescent structures were enclosed by a 3 nm shell of Al_2O_3. Due to numerical meshing considerations, the thickness was chosen to be a multiple of 1 nm, and 3 nm was chosen to slightly overestimate the effect. The structure model parameters D and H now reference the oxide shell, whereas the enclosed Al structure is correspondingly reduced in size. The reduction in size should blue-shift the plasmonic resonances, whereas the oxide shell (being of higher refractive index than the surrounding medium) should red-shift the resonances.

The effect of the oxide shell on the nanocrescent near-field resonances is shown in Figure 5.12 for different sizes D and H. Note that some of the smallest structures were not included in these results as their volume fractions of oxide resulted in negligible external intensity enhancement. In general, the resonances are red-shifted, with a reduction in intensity measured outside of the structure. The significant reduction in intensity is primarily due to the fact that a portion of the enhanced local field is buried within the oxide layer. Thinner (e.g., H = 20 nm) and smaller (i.e., D < 100 nm) structures are more strongly affected. However, higher-order resonances of larger structures can still be utilized, with factor ~10 enhancement achievable throughout the 200 to 400 nm range. As with the nonoxidized structures, some improvement in enhancement can be obtained by using greater deposition angles θ.

The effect of the oxide shell on the near-field intensity patterns is shown in Figure 5.13 and Figure 5.14 for short and long-axis illumination resonances, respectively. The 3-D renderings show the external intensity patterns, while the 2-D cross-sections show the intensity patterns throughout the plane at the nanocrescent-substrate interface. In Figure 5.13d, the short-axis dipole mode pattern still exhibits strong field localization near the tips, but as shown in panel (b), the field that extends into the surrounding medium is split due to the increased effective oxide thickness at the tip apex, such that the region of strongest intensity enhancement is buried within the oxide shell. For the higher-order resonance at λ = 290 nm, Figure 5.13 a and c, the enhancement pattern manifests primarily at the backbone interior, with peak external intensity enhancement values of about 30x.

Similar behaviors are seen for the long-axis resonances. Again, the highest near-field

intensity at the tips for the quadrupole mode is buried within the oxide layer, as shown in Figure 5.14 b and d, while the portion of the higher-order resonance mode at λ = 230 nm that extends into the surrounding medium is more strongly confined to the backbone region.

It should be noted that with the NTL fabrication method, scaling structure size requires $H \leq D/2$. It therefore appears to be infeasible to scale these structures small enough to access the short-axis dipole resonance in the UV due to dual effects of oxide formation – increasing oxide volume fraction and resonance red-shifting. The situation is similar for the long-axis quadrupole resonances and will generally be the case for the low-order resonances of any Al nanoantenna, especially antennas comprising tapered tips. However, local intensity enhancement in the UV can still be achieved through the higher-order resonance modes of larger nanocrescents, where these modes are localized in the backbone region and are less affected than the tips by geometrical curvature that increase the effective oxide thickness near the regions of highest enhancement.

5.5 Conclusions

Using a "UV plasmonic" metal such as aluminum, the response of nanocrescent antennas can be shifted to short wavelengths by appropriate manipulation of fabrication parameters, such as the angle of deposition, metal thickness, and bead template diameter. Short-axis dipole and long-axis quadrupole resonances can be shifted into the UV range by using small diameters (Figure 5.15), but as the diameter decreases so does local intensity enhancement. Higher-order modes, however, are very promising for operating in this range and can produce strong and tunable intensity enhancement. For a given

diameter, the wavelength of operation of the short-wavelength resonances can be adjusted by using an appropriate angle of deposition (Figure 5.15) and the intensity enhancement can be adjusted through the height (Figure 5.11), neither of which present a restrictive change in the fabrication process.

For comparison, other investigations of the near-field response of UV antennas have been performed. A previous study of 40 nm diameter Al hemispheres predicted a ~10x spatially averaged intensity enhancement (with a maximum enhancement of 200), also neglecting the native oxide layer [110]. The same study showed that for the case of a spherical Al particle, corresponding enhancements are about 10x lower. Other studies have investigated local field enhancement in the gap between Al nanosphere dimers. Using 20 nm diameter Al spheres with a 1 nm gap, average gap enhancements ~1000x were predicted throughout the UV [96]. Similar enhancements were predicted with 80 nm Al spheres and 2–8 nm gaps in the near-UV range [111]. Under the same assumption of neglecting the native oxide, the enhancements produced by the higher-order resonances of the nanocrescent are comparable: >50x spatially-averaged intensity enhancement, with peak values ~1000x.

We further investigated the effect of the native oxide on the near-field response of the nanocrescent antenna. The presence of the oxide layer red shifts the near-field resonances and reduces the local intensity enhancement. Resonance modes with intensity localization near the tips are most strongly affected, making a stronger case for the use of higher-order resonances for UV response. Through the higher-order modes, averaged intensity enhancements >10x can still be achieved throughout the UV, with peak values of about 30x. Again, this is comparable to other reports. A previous study of ~100 nm conical Al

nanoparticles, incorporating a 3 nm oxide layer, predicted 100x peak enhancement in the mid-UV due to a quadrupolar resonance, with spatially-averaged enhancement of ~10x estimated from SERRS measurements [112]. A number of experimental fluorescence studies have also been performed, with typical enhancements ~10x reported [111], [113].

In summary, we have shown that higher-order resonance modes of the nanocrescent produce a number of local intensity pattern combinations between the tips and backbone of the structure in the UV range. These modes can potentially be exploited for applications in single-molecule spectroscopy and initiating localized photochemical reactions.

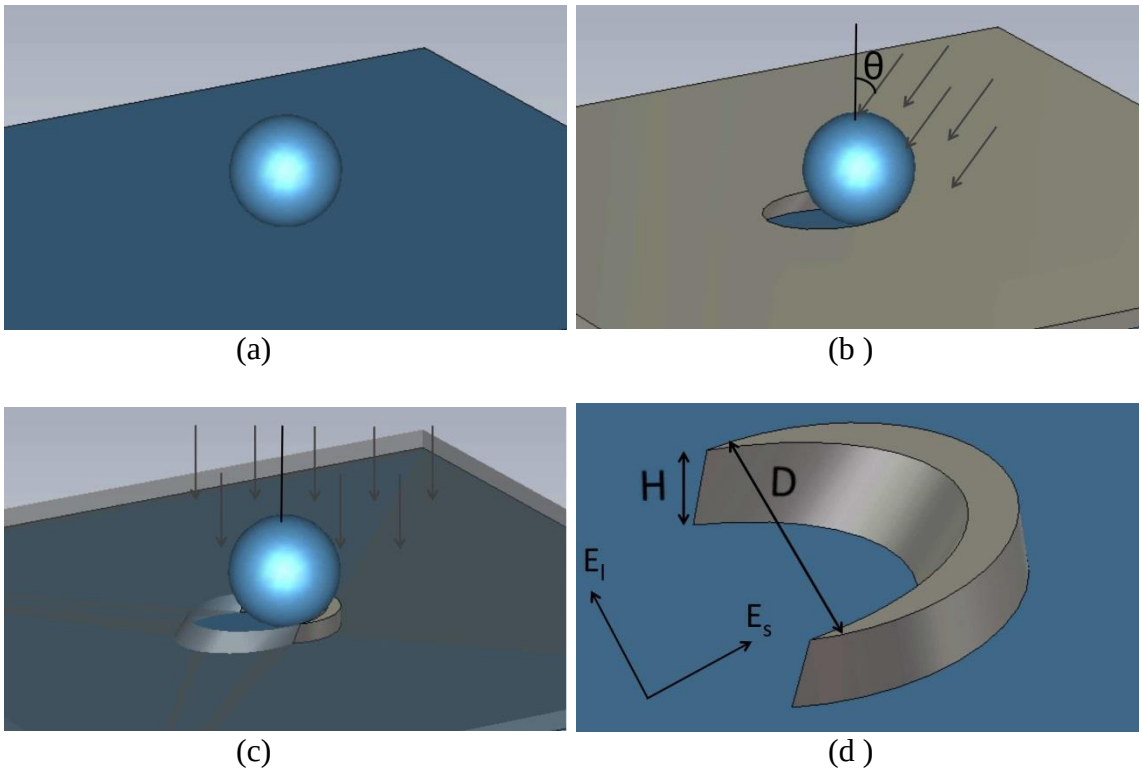

(a) (b) (c) (d)

Figure 5.1. Fabrication of antennas via nanosphere template lithography. (a) The process begins by depositing beads on a substrate. (b) A layer of metal is then deposited at a desired angle. (c) This is followed by etching at a right angle to the substrate where the bead acts to protect the metal beneath it. (d) The bead is then lifted off, leaving a crescent-shaped nanoantenna.

Shape	Material	Priority
Hexahedral	Glass	1
Tilted Cylinder	Cylinder	2
Sphere	Free Space	3
Right Cylinder	Aluminum	4

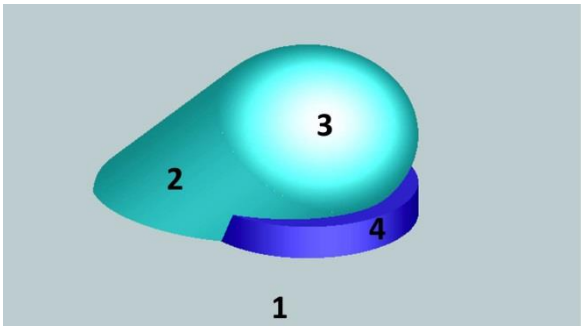

Figure 5.2. Priority assigned to different objects in the creation of the crescent simulation model. An object with a lower number overrides higher number objects embedded within it.

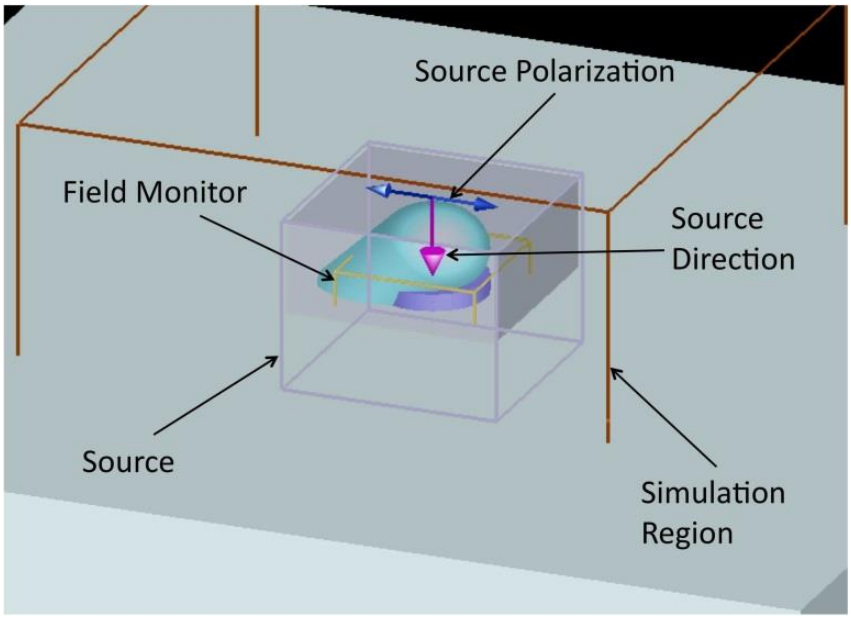

Figure 5.3. Simulation setup.

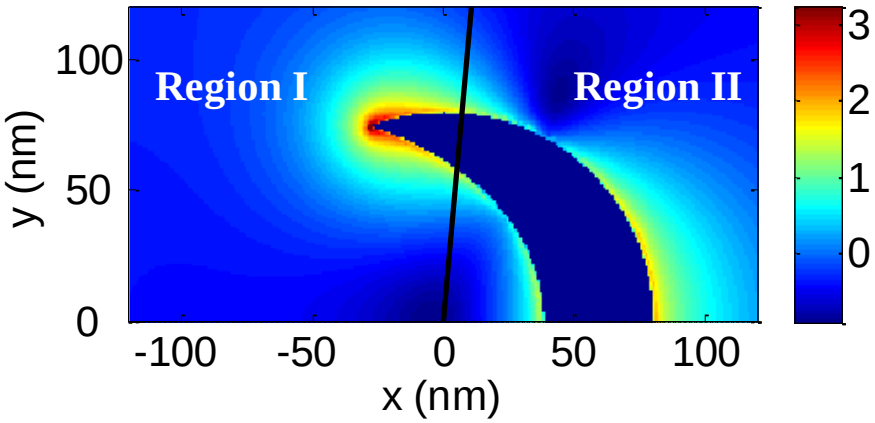

Figure 5.4. Fields are averaged over Regions I and II to determine the tip and backbone near-field response. Fields are also averaged over both regions combined to determine the overall response.

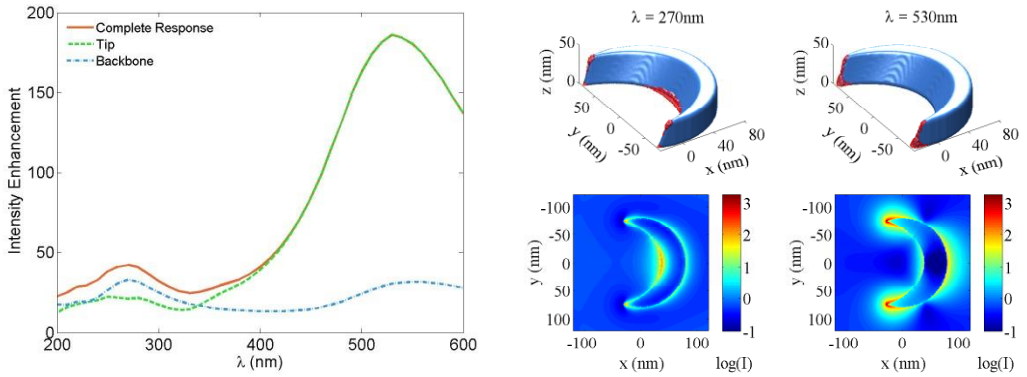

(a) (b)

Figure 5.5. Intensity enhancement response of a crescent antenna with D = 160, H = 30 nm, and θ = 40° that was excited with a short-axis polarized source. (a) Spectral response. (b) 3-D and 2-D cross-section views of the intensity distributions of the crescent at the λ = 270 nm and 530 nm resonances. The 2-D cross-section views are at the plane of the metal-substrate interface.

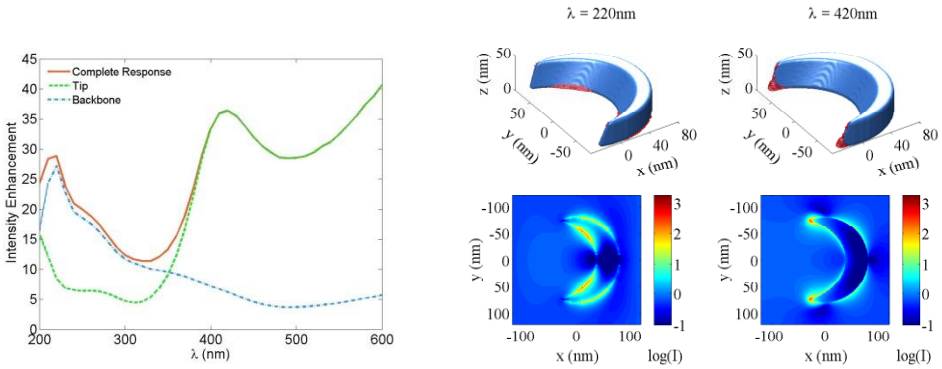

(a) (b)

Figure 5.6. Intensity enhancement response of crescent with D = 160 nm, H = 30 nm, and θ = 40° that was excited with a long-axis polarized source. (a) Spectral response. (b) 3-D and 2-D cross-section views of the intensity distributions of the crescent at the λ = 220 nm and 420 nm resonances. The 2-D cross-section views are at the plane of the metal-substrate interface.

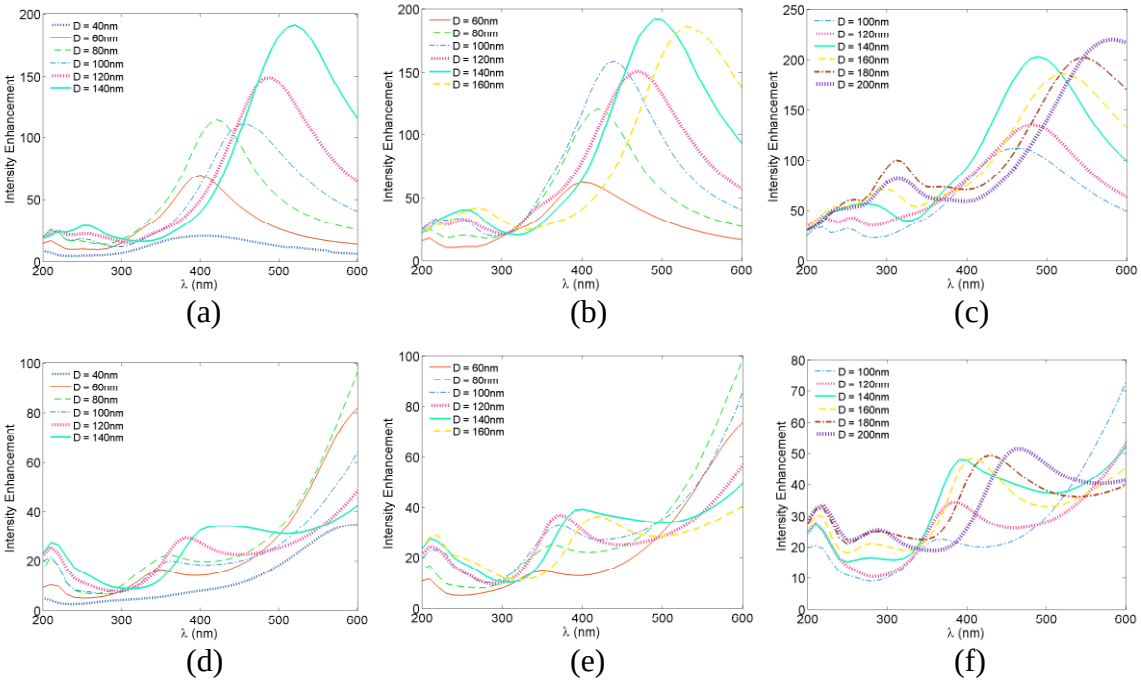

Figure 5.7. Near-field response of crescent antennas with (a, d) H = 20 nm, (b, e) H = 30 nm, (c, f) H = 50 nm and $\theta = 40^0$ as the diameter is varied when excited by (a, b, c) short and (d, e, f) long-axis polarized sources.

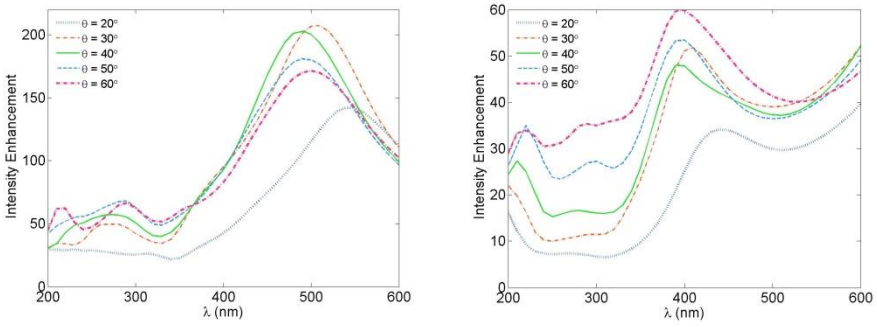

Figure 5.8. Near-field response of crescent with D = 140 nm and H = 50 nm as the deposition angle is varied when excited by a) short and b) long-axis polarized sources.

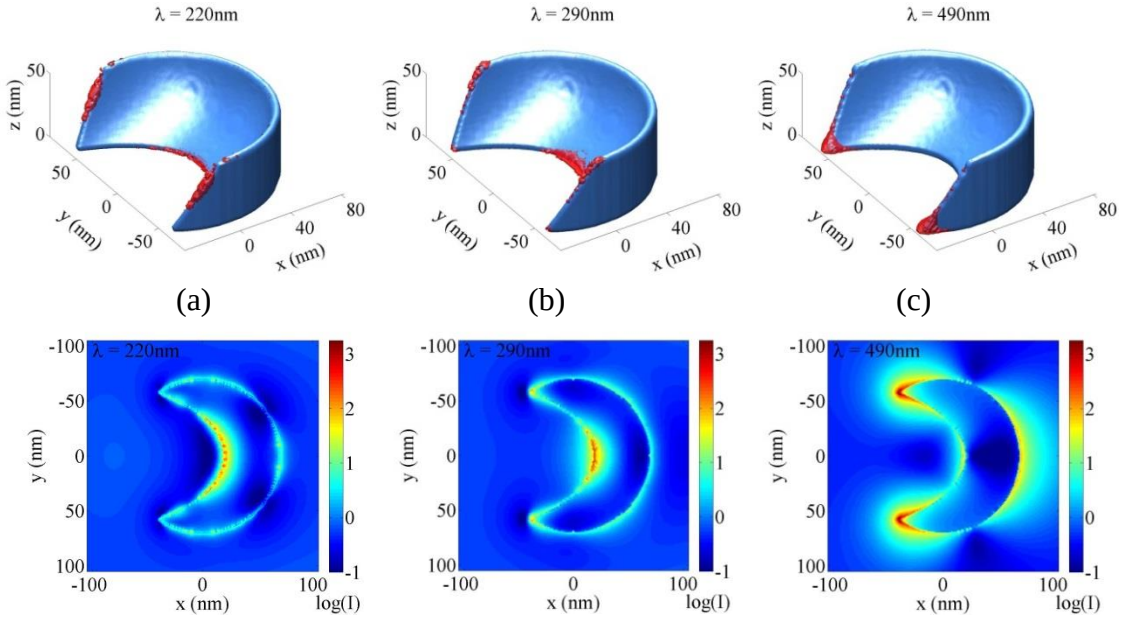

Figure 5.9. 3-D and 2-D cross-section views of the intensity distributions of a crescent antenna (D = 140 nm, H = 50 nm, θ = 60°) at λ = 220 nm, 290 nm, and 490 nm under short-axis illumination. The 2-D cross-section views are at the plane of the metal-substrate interface.

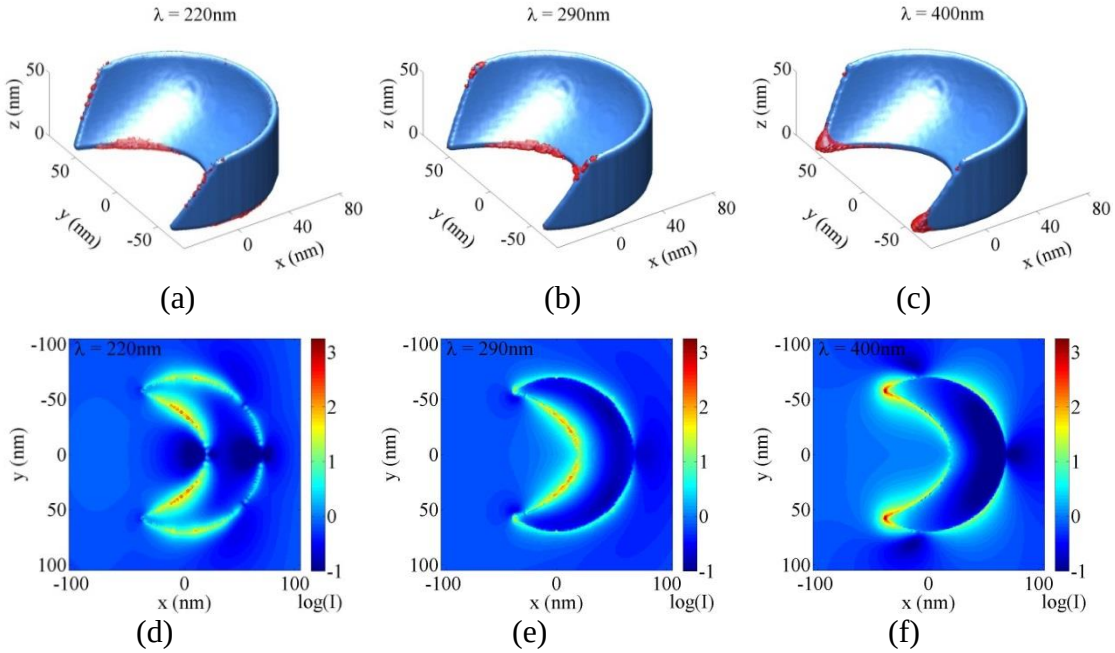

Figure 5.10. 3-D and 2-D cross-section views of the intensity distributions of a crescent antenna (D = 140 nm, H = 50 nm, θ = 60°) at λ = 220 nm, 290 nm, and 400 nm under long-axis illumination. The 2-D cross-section views are at the plane of the metal-substrate interface.

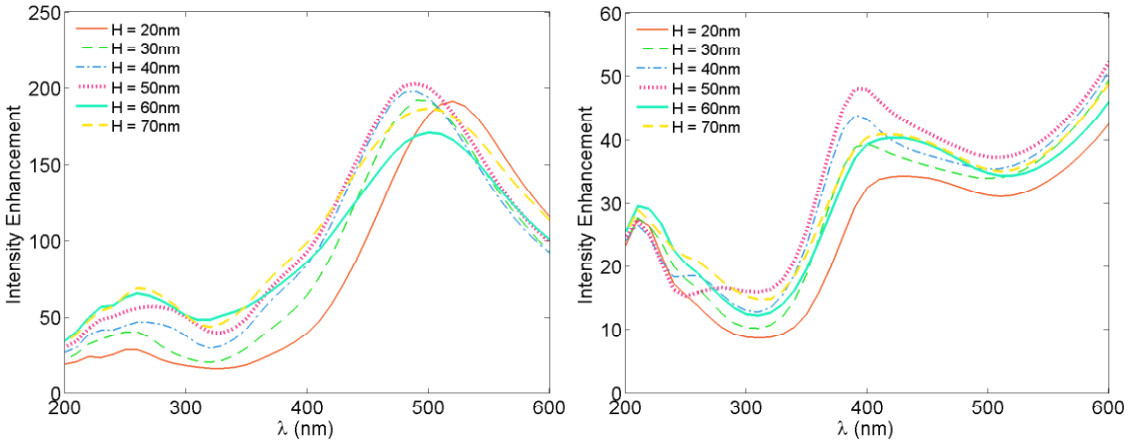

Figure 5.11. Near-field response of crescent with D = 140 nm and $\theta = 40^0$ as the height is varied when excited by (a) short and (b) long-axis polarized sources.

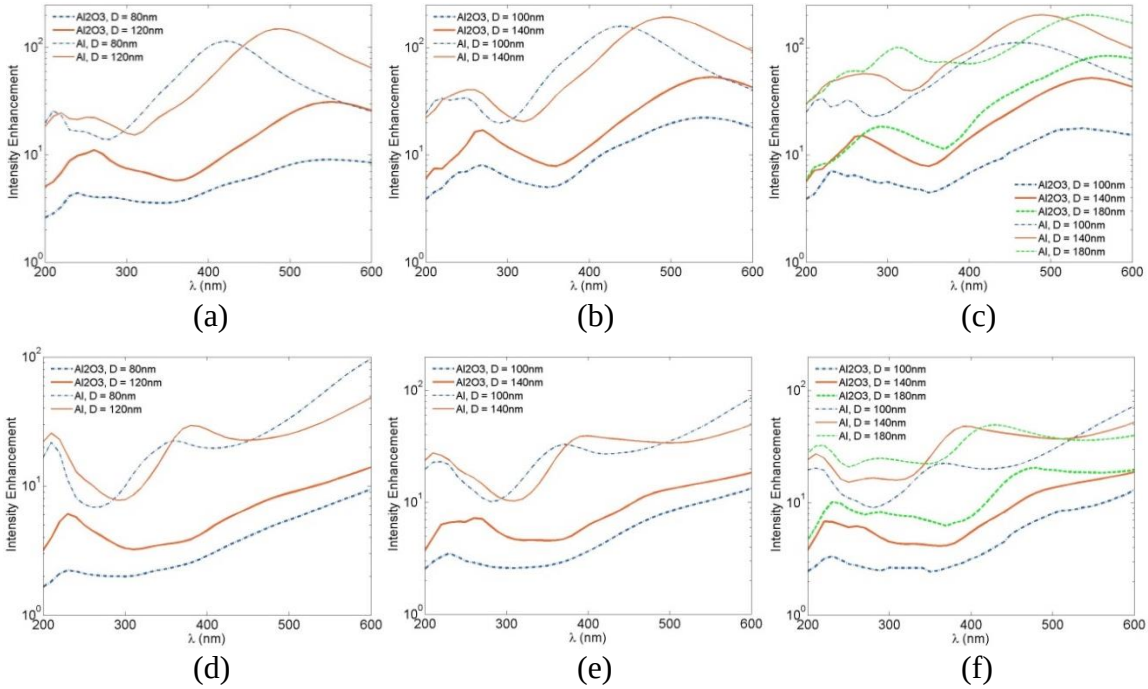

Figure 5.12. Near-field response of crescent antennas, including a 3 nm oxide shell, with (a, d) H = 20 nm, (b, e) H = 30 nm, (c, f) H = 50 nm, and $\theta = 40^0$ as the diameter is varied when excited by (a, b, c) short and (d, e, f) long-axis polarized sources. A log intensity scale is used to better exhibit the resonance peaks.

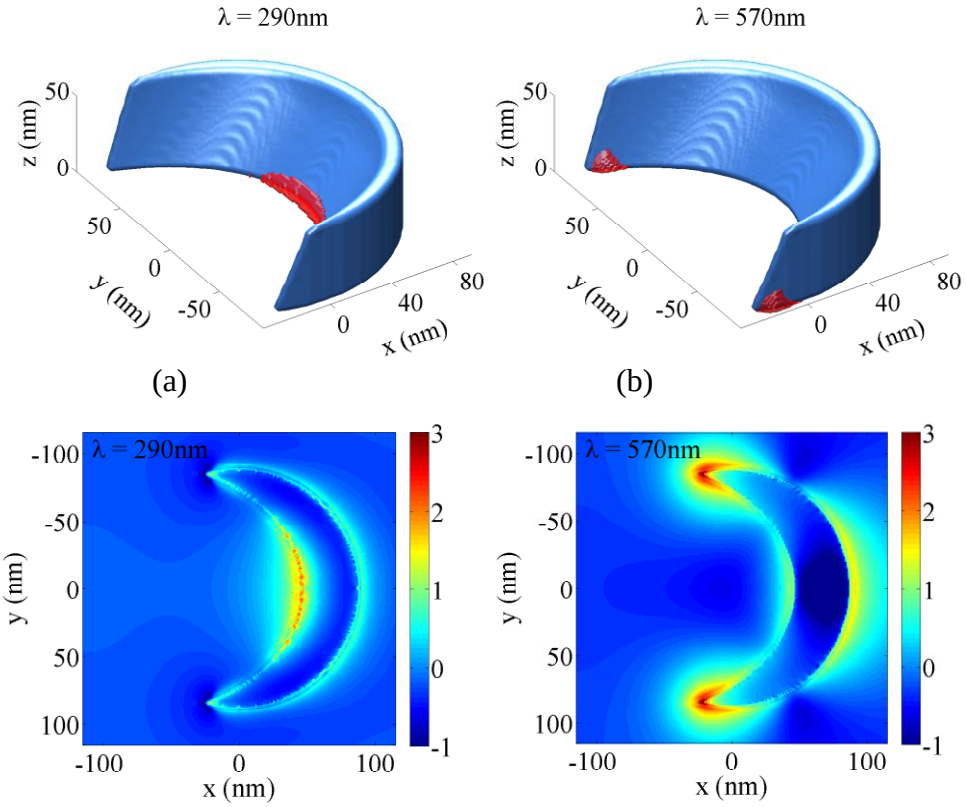

Figure 5.13. 3-D and 2-D cross-section views of the intensity distributions of a crescent antenna (D = 180 nm, H = 50 nm, θ= 40^0) with a 3 nm oxide shell, shown at λ = 290 nm and 570 nm under short-axis illumination. The 2-D cross-section views are at the plane of the metal-substrate interface.

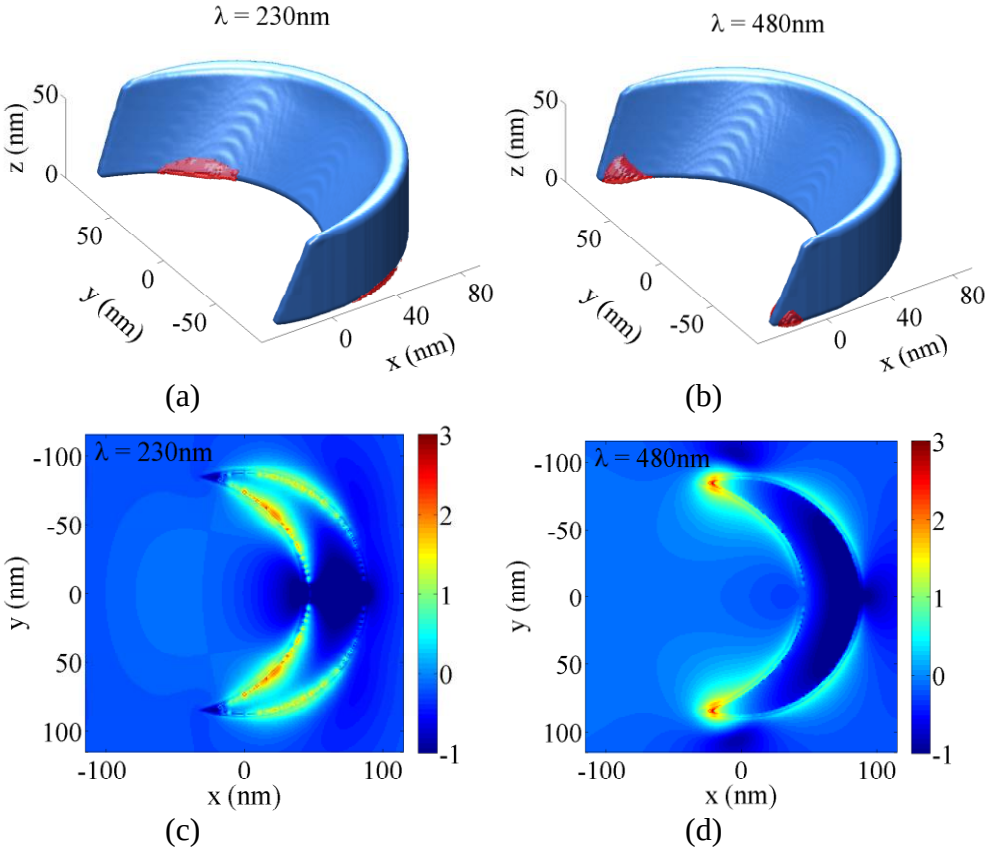

Figure 5.14. 3-D and 2-D cross-section views of the intensity distributions of a crescent antenna (D = 180 nm, H = 50 nm, θ = 40^0) with a 3 nm oxide shell, shown at λ = 230 nm and 480 nm under long-axis illumination. The 2-D cross-section views are at the plane of the metal-substrate interface.

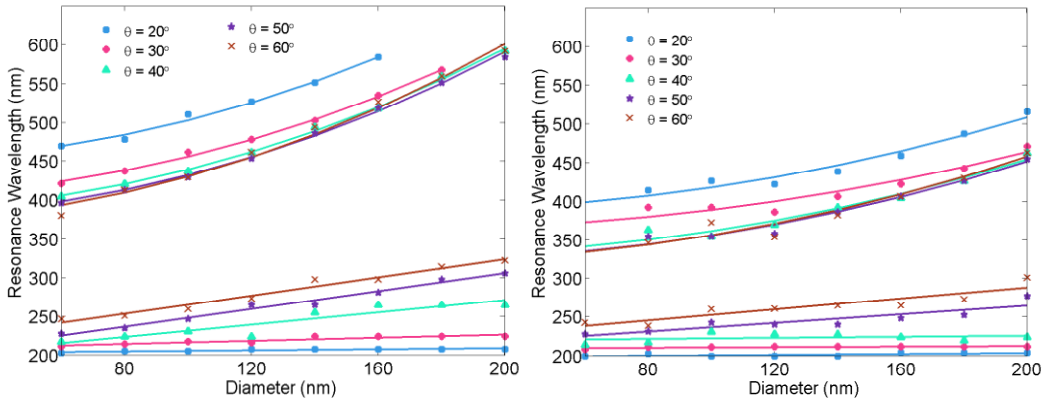

Figure 5.15. Nanocrescent resonances as the diameter is varied for different deposition angles with H = 30 nm when excited by (a) short and (b) long-axis polarized sources. For short-axis excitation, positions of the dipole and quadrupole resonances are plotted. For long-axis excitation, positions of the quadrupole and principal higher-order resonances are plotted.

CHAPTER 6

CONCLUSION

The purpose of this research was to study the effect of material losses in RF and optical antennas. Implantable spiral antennas and crescent nanoantennas at RF and optical frequencies, respectively, were used for this investigation. The results demonstrated that materials properties influence the performance of antennas especially when lossy materials are involved. Metals are excellent conductors at RF frequencies, but particular applications involve lossy media. These lossy media must be taken into account in order to offset their detrimental effects on resonance. At first glance, all materials seem to be atypical for optical antennas. The reason for this is that the electrical properties that make metals so desirable at RF frequencies degrade at optical frequencies. Metals are still good candidates for antennas at optical frequencies, but care must be taken in selecting the appropriate metal for the appropriate operational wavelength range. It is also important to take into account the variability of electrical properties (i.e., complex permittivity, complex refractive index, etc.) as the wavelength changes. At optical wavelengths, the permittivity must be considered a dielectric function rather than a dielectric constant for calculation purposes. The contributions of this research are the demonstrated resonance of lossy antennas at various frequency ranges from the RF to the ultraviolet and are described below.

6.1 Contributions

6.1.1 Implatable Antenna Designed for Ease of Manufacture

In order to study the use of realistic materials in implantable antennas, the effect of biocompatible materials in spiral antennas was investigated. This was described in Chapter 3, and presented at [12]. Design, simulation, manufacturing and testing were all accomplished using biocompatible materials. Radiating element, ground plane, and shorting tab were made from titanium. The substrate was created from epotek epoxy, and silicone superstrate was used to insulate the antenna from its lossy environment. The resulting design was shown to produce resonance over the desired frequency range and meet stringent requirements for materials used. Additionally, the antenna was designed for ease of manufacturabily using nonconventional RF materials. Testing was simplified by using saline solution as the conductive environment where the antenna operates. Simulations showed that change of the operating environment would shift the resonance to higher frequencies.

6.1.2 Scaling the Response of Crescent Nanoantennas into the UV

The use of aluminum in crescent nanoantennas was studied to determine the feasibility of obtaining resonance in the ultraviolet wavelength range. This investigation is described in Chapter 5, was published in [10], and presented at [13]–[15]. Additional investigations are currently being done and are described in section 4.4.2.2. Using a “UV plasmonic” metal such as aluminum, the response of nanocrescent antennas can be shifted to short wavelengths by appropriate manipulation of fabrication parameters, such as the angle of

deposition, metal thickness, and bead template diameter. Short-axis dipole and long-axis quadrupole resonances can be shifted into the UV range by using small diameters, but as the diameter decreases so does local intensity enhancement. Higher-order modes, however, are very promising for operating in this range and can produce strong and tunable intensity enhancement. For a given diameter, the wavelength of operation of the short-wavelength resonances can be adjusted by using an appropriate angle of deposition, and the intensity enhancement can be adjusted through the height, neither of which presents a restrictive change in the fabrication process.

6.1.3 Polarization Anisotropy of Crescent Nanoantennas

The ability to induce or suppress resonance modes of gold and silver crescent antennas at infrared wavelengths by manipulating the polarization of incident light was described in section 4.4.3.3 and published in [11]. The study showed that of crescent antennas poses two distinct dipole resonances, which can be controlled independently. A longer wavelength resonance is induced when the source polarization is oriented along the longest dimension of the crescent and a second resonance at a shorter wavelength is induced for a source polarized along the shortest dimension of the structure. The strength of each resonance and accompanying near-fields can be controlled in degrees from its highest intensity to complete suppression by merely rotating the polarization of the source. Control of intensity results in control of near-field volume that would prove valuable in single molecule detection where the probe volumes need to be kept down to within the physical dimensions of the molecule.

6.1.4 Plasmonic Gold and Silver Nanocrescent Arrays

Maximizing the use of crescent antennas by creating closed-packed arrays is described in section 4.4.3.4. The results demonstrated that the response of these arrays is not much different than that of single crescents, but the benefits could be immense. Increasing the density of crescents in a substrate results in increasing the usable area and could prove significant in sensing by enhancing the probability of enhancing signals of molecules drifting on a substrate.

6.1.5 Mid-IR LSPR of Gold and Silver Nanocrescents

Gold and Silver Nanocrescent antennas for operation at mid-IR wavelengths were described in section 4.4.4.1. The study demonstrated that resonances of crescent antennas can be scaled into the mid-IR due to the great degree of control that can be independently exerted on the different features of the antennas. It was noted that ability to maintain a nanometer scale width and micrometer scale length is key to maintain resonance in this wavelength range. The fabrication method used for crescent antennas allows for easily manipulating these dimensions independently. The results showed that although the resonances of gold and silver antennas are very similar in wavelength, a plamonic type resonance still exists.

REFERENCES

[1] Wikipedia, *Antenna (radio)* [Online]. Available: http://en.wikipedia.org/wiki/Antenna_%28radio%29

[2] P. Bharadwaj, B. Deutsch, and L. Novotny, "Optical antennas," *Adv. Opt. Photonics*, vol. 1, no. 3, pp. 438–483, 2009.

[3] S. Nie and S. R. Emory, "Probing single molecules and single nanoparticles by surface-enhanced raman scattering," *Science*, vol. 275, no. 5303, pp. 1102–1106, Feb. 1997.

[4] K. Mitsui, Y. Handa, and K. Kajikawa, "Optical fiber affinity biosensor based on localized surface plasmon resonance," *Appl. Phys. Lett.*, vol. 85, pp. 4231–4233, Nov. 2004.

[5] L. Cao, P. Fan, A. P. Vasudev, J. S. White, Z. Yu, W. Cai, J. A. Schuller, S. Fan, and M. L. Brongersma, "Semiconductor nanowire optical antenna solar absorbers," *Nano Lett.*, vol. 10, pp. 439–445, 2010.

[6] A. C. Atre, A. Garcia-Etxarri, H. Alaeian, and J. A. Dionne, "Toward high-efficiency solar upconversion with plasmonic nanostructures," *J. of Opt.*, vol. 14, pp. 1–7, 2012.

[7] X. Huang, S. Neretina, and M.A. El-Sayed, "Gold nanorods: from synthesis and properties to biological and biomedical applications," *Adv. Mat.*, vol. 21, pp. 4880–4910, 2009.

[8] J. M. Lourtioz, H. Benisty, V. Berger, J. M. Gerard, D. Maystre, and A. Tchelnokov, "Specific Features of Metallic Structures," *Photonic Crystals*, 1st Edition, New York, Springer, 2005, ch. 4, sec.1, pp. 122–123.

[9] S. A. Maier, "Electromagnetics of Metals," *Plasmonics Fundamentals and Applications*, 1st Edition, New York, Springer, 2007, ch. 1, sec. 1, pp. 6.

[10] M. Rodriguez, C. Furse, J. S. Shumaker-Parry, and S. Blair, "Scaling the response of nanocrescent antennas into the ultraviolet," *ACS Photon.*, pp. 496–506, May, 2014.

[11] C. T. Cooper, M. Rodriguez, S. Blair, and J. S. Shumaker-Parry, "Polarization anisotropy of multiple localized plasmon resonance modes in noble metal

nanocrescents," *J. Phys. Chem.*, pp. 1167–1173, 2014.

[12] M. Rodriguez, R. Franklin, and C. Furse, "Manufacturing considerations for implantable antennas," presented at 2013 IEEE Int. Symp. Antennas and Propagation and North American Radio Science Meeting, Florida, USA, Jul 2013.

[13] M. Rodriguez, J. S. Shumaker-Parry, and S. Blair, "Scaling the plasmonic response of nanocrescents to the UV," presented at Surface Plasmon Photonics 6, Ontario, CA, 2013.

[14] M. Rodriguez, C. Furse, J. S. Shumaker-Parry, and S. Blair, "Scaling the response of nanocrescent antennas into the ultraviolet," presented at 2014 IEEE Int. Symp. Antennas and Propagation and North American Radio Science Meeting, Tennessee, 2014.

[15] M. Rodriguez, J. S. Shumaker-Parry, and S. Blair, "Scaling the plasmonic response of nanocrescents to the UV," presented at Near-Field Optics, Nanophotonics, and Related Techniques 13, Salt Lake City, UT, 2014.

[16] P. Soontornpipit, C.M. Furse, and Y.C. Chung, "Design of implantable microstrip antenna for communication with medical implants," *Special Issue of IEEE Trans. Microw. Theory Tech. on Medical Applications and Biological Effects of RF/Microwaves* , vol. 52, no. 8, part 2, pp. 1944–1951, Sep. 2004.

[17] R. Bukasov and J. S. Shumaker-Parry, "Highly tunable infrared extinction properties of gold nanocrescents," *Nano Lett.*, vol. 7, no. 5, pp. 1113–1118, May 2007.

[18] D. Sarid and W. Challenenr, "Electromagnetics of planar surface waves," *Modern Introdution to Surface Plasmons,* 1st Edition, New York, Cambridge, 2010, ch. 2, sec 2, pp. 7–10.

[19] F. T. Ulaby, "Plane-Wave Propagation," *Fundamentals of Applied Electromagnetics,* 5th Edition, New Jersey, Pearson Prentice Hall, 2007, ch. 7, sec. 4, pp. 304–307.

[20] D. J. Griffiths, "Electromagnetic Waves," *Introduction to Electrodynamics,* 3th Edition, New Jersey, Pearson Addison Wesley, 1999, ch. 9, sec. 4, pp. 394.

[21] C. A. Balanis, *Advanced Engineering Electromagnetics*, 1st Edition, New Jersey, Wiley, 1989, pp. 62, 150.

[22] W. Cai and V. Shalaev, "Optical Properties of Metal-Dielectric Composites," *Optical Metamaterials Fundamentals and Applications,* 1st Edition, New York, Springer, 2010, ch. 2, sec. 3, pp. 21.

[23] P. B. Johnson and R. W. Christy, "Optical constants of the noble metals," *Phys. Rev. B*, vol. 6, no. 12, pp. 4370–4379, 1972.

[24] U. Kreibig and M. Vollmer, "Theoretical Considerations," *Optical Properties of Metal Clusters*, 1st Edition, New York, Springer, 1995, ch. 2, sec. 1, pp. 22.

[25] L. Novotny and B. Hecht, "Surface Plasmons," *Principles of Nano-Optics*, 1st Edition, New York, Cambridge, 2006, ch. 12, pp. 378–383.

[26] P. R. West, S. Ishii, G. V. Naik, N. K. Emani, V. M. Shalaev, and A. Boltasseva, "Searching for better plasmonic materials," *Laser & Photon.*, Rev. 4, pp. 795–808, 2010.

[27] K. A. Willets and R. P. Van Duyne, "Localized surface plasmon resonance spectroscopy and sensing," *Ann. Rev. Phys. Chem.*, vol. 58, pp. 267–297, 2007.

[28] A. J. Johansson, "Simulation and verification of pacemaker antennas," in Proc. 25th Ann. Int. Conf. IEEE EMBS, Cancun, Mexico, 2003, pp. 3279–3281.

[29] K. Guillory and R. A. Normann, "A 100-channel system for real time detection and storage of extracellular spike waveforms," *J. Neurosci. Methods*, vol. 91, pp. 21–29, 1999.

[30] T. Buchegger et al., "An ultra-low power transcutaneous impulse radio link for cochlea implants," in Joint Ultra Wideband Systems and Technologies (UWBST) and Int. Workshop on UWBS 2004 (IEEE Cat. No. 04EX812) pp. 356–360, 2004.

[31] K. Gosalia, G. Lazzi, and M. Humayun, "Investigation of microwave data telemetry link for a retinal prosthesis," *IEEE Trans. MTT*, Vol. 52, No. 8, pp. 1925–1932, Aug. 2004.

[32] P. R. Troyk and M. A. K. Schwan, "Closed loop Class E transcutaneous power and data link for microimplants," *IEEE Trans. Biomed. Eng.*, vol. 39, pp. 589–598, June 1992.

[33] S. Soora, K. Gosalia, M. Humayun, and G. Lazzi, "A comparison of 2 and 3D dipole antennas for an implantable retinal prosthesis," *IEEE Trans. AP*, vol. 56, no. 3, pp. 622–629, Mar. 2008.

[34] M. D. Amundson et al., "Circumferential antenna for an implantable medical device," U.S. Patent 6,456,256, Sep. 24, 2002.

[35] C. Furse, H. K. Lai, C. Estes, A. Mahadik, and A. Duncan, "An implantable antenna for communication with implantable medical devices," presented at 1999 IEEE Antennas and Propagation/ URSI Int. Symp., Orlando, FL, July 1999.

[36] J. Kim and Y. Rahmat-Samii, "Implanted antennas inside a human body: simulations, designs, and characterizations," *IEEE Trans. Microwave Theory Tech.*, vol. 52, no. 8, pp. 1934–1943, Aug. 2004.

[37] P. Soontornpipit, C. M. Furse, and Y. C. Chung, "Miniaturized biocompatible

microstrip antenna using genetic algorithm," *IEEE Trans. Antennas Propag.*, Vol. 53, No. 6, pp. 1939–194, June 2005.

[38] IA. J. Bahl and P. Bhartia,S.Stuchly, "Design of microstrip antennas covered with a dielectric layer," *IEEE Trans. Antennas Propagation*, vol. AP-30, no. 2, pp. 314–318, Mar. 1982.

[39] T. Karacolak, R. Cooper, and E. Topsakal, "Electrical properties of rat skin and design of implantable antennas for medical wireless telemetry," *IEEE Trans. AP* vol. 57, no. 9, pp. 2806–2812, Sep. 2009.

[40] Medical Implant Communications Service (MICS) Federal Register, "Rules and Regulations," vol. 64, no. 240, pp. 69926–69934, Dec. 1999.

[41] "IEEE Standard for Safety Levels with Respect to Human Exposure to Radio Frequency Electromagnetic Fields, 3 kHz to 300 GHz - Amendment 1: Specifies Ceiling Limits for Induced and Contact Current, Clarifies Distinctions between Localized Exposure and Spatial Peak Power Density," IEEE Std C95.1a-2010 (Amendment to IEEE Std C95.1-2005) , pp.C1-9, Mar. 2010.

[42] ICNIRP, "Guidelines for limiting exposure to time-varying electric, magnetic, and electromagnetic fields (up to 300 GHz)," *Health Phys.*, vol. 74, pp. 494–522, 1998.

[43] NuSil Silicone Technology, "MED16-6606 RTV Silicone Dispersion," http://www.nusil.com/library/products/MED16-6606P.pdf

[44] Epoxy Technology, "EPO-TEK 301 Epoxy," http://www.epotek.com/sscdocs/datasheets/301.PDF

[45] Computer Simulation Technology (CST), http://www.cst.com/

[46] S. M. Smith and C. Furse, "Stochastic FDTD for analysis of statistical variation in electromagnetic fields," *IEEE Trans. Antennas Propagation*, vol. 60, no. 7, pp. 3343–3350, Jul. 2012.

[47] J. Johnson and C. Furse, "Statistical analysis of detuning effects for implantable microstrip antennas," presented at North American Radio Science Conf. URSI-CNC/USNC, Ottawa, Canada, Jul. 22-26, 2007.

[48] Thermo Scientific, "NERL blood bank saline," Part Number 8505, http://www.thermoscientific.com/ecomm/servlet/productsdetail?productId=11954844&groupType=PRODUCT&searchType=0&storeId=11152&from=search

[49] S. Gabriel, R.W. Lau, and C. Gabriel, "The dielectric properites of biological tissues: II. measurements in the frequency range 10Hz to 20 GHz," *Phys. Med. Biol.*, vol. 41, pp. 2251–2269, 1996.

[50] R. Bukasov and J. S. Shumaker-Parry, "Silver nanocrescents with infrared plasmonic properties as tunable substrates for surface enhanced infrared absorption spectroscopy," *Anal. Chem.*, vol. 81, no. 11, pp. 4531–4535, Jun. 2009.

[51] R. Bukasov, T. A. Ali, P. Nordlander, and J. S. Shumaker-Parry, "Probing the plasmonic near-field of gold nanocrescent antennas," *ACS Nano*, vol. 4, no. 11, pp. 6639–6650, 2010.

[52] J. S. Shumaker-Parry, H. Rochholz, and M. Kreiter, "Fabrication of crescent-shaped optical antennas," *Adv. Mat.*, pp. 2131–2134, 2005.

[53] H. Rochholz, N. Bocchio, and M Kreiter, "Tuning resonances on crescent-shaped noble-metal nanoparticles," *New J. Phys.*, vol. 9, pp. 53–70, Mar. 2007.

[54] A. Unger, U. Rietzler, R. Berger, and M. Kreiter, "Sensitivity of crescent-shaped metal nanoparticles to attachment of dielectric colloids," *Nano Lett.*, vol. 9, no. 6, pp. 2311–2315, 2009.

[55] M. Retsch, M. Tamm, N. Bocchio, N. Horn, R. Forch, U. Jonas, and M. Kreiter, "Parallel preparation of densely packed arrays of 150-nm gold-nanocrescent resonators in three dimensions," *Small*, vol. 5, no. 18, pp. 2105–2110, 2009.

[56] N. Vogel, J. Fischer, R. Mohammadi, M. Retsch, H. Butt, K. Landfester, C. K. Weiss, and M. Kreiter, "Plasmon hybridization in stacked double crescents arrays fabricated by colloidal lithography," *Nano Lett.*, vol. 11, pp. 446–454, Jan. 2011.

[57] J. Fischer, N. Vogel, R. Mohammadi, H. Butt, K. Landfester, C. K. Weiss, and M. Kreiter, "Plasmon hybridization and strong near-field enhancements in opposing nanocrescent dimers with tunable resonances," *Nanoscale*, vol. 3, pp. 4788–4797, 2011.

[58] L. Yang, C. Hu, P. Gao, and X. Luo, "Self-similar chain of nanocrescents with giant electric field enhancement as a novel plasmonic resonator," presented at IEEE Photonics Global, Singapore, 2008, pp. 1-4.

[59] V. Ovchinnikov and A. Shevchenko, "Large-area arrays of pillar-based metal nanostructures," presented at Third Int. Conf. Quantum, Nano and Micro Technologies, Cancun, Mexico, 2009, pp. 125-129.

[60] L. Feng, D. V. Orden, M. Abashin, Q. J. Wang, Y. R. Chen, V. Lomakin, and Y. Fainman, "Nanoscale optical field localization by resonantly focused plasmons," *Opt. Express*, vol. 17, no. 6, pp. 4824–4832, 2009.

[61] Z. A. Lewicka, Y. Li, A. Bohloul, W. W. Yu, and V. L. Colvin, "Nanorings and nanocrescents formed via shaped nanosphere lithography: a route toward large areas of infrared metamaterials," *Nanotechnology*, vol. 24, pp. 1–11, 2013.

[62] Z. Zhang, B. Zhou, Y. Huang, Z. Liao, Z. Li, S. Li, S. Wang, and W. Wen, "Gold crescent nanodisk array for nanoantenna-enhanced sensing in subwavelength areas," *Appl. Opt.*, vol. 53, no. 31, pp. 7236–7240, 2014.

[63] Y. Lu, G. L. Liu, J. Kim, Y. Mejia, and L. P. Lee, "Nanophotonic crescent moon structures with sharp edge for ultrasensitive biomolecular detection by local electromagnetic field enhancement effect," *Nano Lett.*, vol. 5, no. 1, pp. 119–124, Jan. 2005.

[64] G. L. Liu, Y. Lu, J. Kim, J. C. Doll, and L. P. Lee, "Magnetic nanocrescents as controllable surface-enhanced raman scattering nanoprobes for biomolecular imaging," *Adv. Mat.*, vol. 17, pp. 2683–2688, 2005.

[65] G. L. Liu, F. Chen, J. A. Ellman, and L. P. Lee, "Peptide-nanoparticle hybrid SERS probe for dynamic detection of active cancer biomarker enzymes," Proc. 28th IEEE EMBS Ann. Int. Conf. New York City, USA, 2006.

[66] J. Kim, G. L. Liu, Y. Lu, and L. P. Lee, "Spectral tuning of localised surface plasmon-polariton resonance in metallic nano-crescents," IEE Proc. Nanobiotechnology, vol. 153, no. 3, pp. 42–46, Jun. 2006

[67] B. M. Ross and L. P. Lee, "Plasmon tuning and local field enhancement maximization of the nanocrescent," *Nanotechonolgy*, vol. 19, pp. 1–6, Jul. 2008.

[68] I. E. Hashem, N. H. Rafat, and E. A. Soliman, "Nanocrescent antenna as a transceiver for optical communication systems," presented at IEEE Int. Symposium on Electromagnetic Compatibility (EMC), 2014, pp. 39–45.

[69] N. C. Azenui and H. Y. D. Yang, "A printed crescent patch antenna for ultrawideband applications," *IEEE Antennas Wireless Propag. Lett.*, vol. 6, pp. 113–116, 2007.

[70] M. E. Chen and J. H. Wang, "CPW-fed crescent patch antenna for UWB applications," *Electronics Lett.*, vol. 44, no. 10, pp. 613–615, May. 2008.

[71] A. K. H. Obsiye, H. E. Abdel-Raouf, and R. El-Islam, "Modified printed crescent patch antenna for ultrawideband RFID (UWB-RFID) Tag," presented at 2008 IEEE Int. RF and Microwave Conf. Proc., Kuala Lumpur, Malaysia, 2008, pp. 274–276.

[72] M. S. Chen, W. C. Weng, and S. T. Wang, "Design of the crescent-shape planar ultra-wideband antenna with a band-notch structure," presented at IEEE 2nd Int. Symp. on Next-Generation Electron. (ISNE), Kaohsiung, Taiwan, 2013, pp. 271–274.

[73] A. Aubry, D. Y. Lei, A. I. Fernandez-Dominguez, Y. Sonnefraud, S. A. Maier, and J. B. Pendry, "Plasmonic light-harvesting devices over the whole visible spectrum," *Nano Lett.*, vol. 10, no. 7, pp. 2574–2579, 2010.

[74] A. C. Atre, A. Garcia-Etxarri, H. Alaeian, and J. A. Dionne, "A broadband negative index metamaterial at optical frequencies," *Adv. Opt. Mat.*, pp. 327–333, 2013.

[75] J. D. Jackson, "Magnetostatics, Faraday's Law, Quasi-Static Fields," *Classical Electrodynamics*, 3rd Edition, New Jersey, Wiley, 1999, ch. 5, sec. 18, pp. 219–223.

[76] C. A. Balanis, "Integral Equations, Moment Method, and Self and Mutual Impedance," *Antenna Theory*, 3rd Edition, New Jersey, Wiley-Interscience, 2005, ch. 8, sec. 3, pp. 442–446.

[77] L. Novotny, "Effective wavelength scaling for optical antennas," *Phys. Rev. Lett.*, vol. 98, pp. 1–4, Jun. 2007.

[78] P. Biagioni, J. Huang, and B. Hecht, "Nanoantennas for visible and infrared radiation," *Rep. Prog. Phys.*, vol. 75, no. 2, pp. 1–40, Mar 2011.

[79] E. Palik, *Handbook of optical constants of solids*, Massachusetts, Academic Press, 2012.

[80] OptoCity, "CaF2 Crystal," http://www.optocity.com/CaF2.htm

[81] A. Aubry, D. Y. Lei, S. A. Maier, and J. B. Pendry, "Broadband plasmonic device concentrating the energy at the nanoscale: The crescent-shaped cylinder," *Phys. Rev. B*, vol. 82, pp. 1–9, Sep. 2010.

[82] V. E. Bochenkov and D. S. Sutherland, "From rings to crescents: a novel fabrication technique uncovers the transition details," *Nano Lett.*, vol. 13, pp. 1216–1220, Mar. 2013.

[83] K. Ray, M. H. Chowdhury, and J. R. Lakowicz, "Aluminum nanostructured films as substrates for enhanced fluorescence in the ultraviolet-blue spectral region," *Anal. Chem.*, vol. 79, pp. 6480–6487, 2007.

[84] T. Dörfer, M. Schmitt, and J. Popp, "Deep-UV surface-enhanced Raman scattering," *J. Raman Spectrosc.*, vol. 38, pp. 1379–1382, 2007.

[85] C. Langhammer, M. Schwind, and B. Kasemo, I. Zoric´, "Localized surface plasmon resonances in aluminum nanodisks," *Nano Lett.*, vol. 8, 1461–1471, 2008.

[86] G. H. Chan, J. Zhao, G. C. Schatz, and R. P. V. Duyne, "Localized surface plasmon resonance spectroscopy of triangular aluminum nanoparticles," *J. Phys. Chem. C*, vol. 112, pp. 13958–13963, 2008.

[87] F. Mahdavi and S. Blair, "Nanoaperture fluorescence enhancement in the ultraviolet," *Plasmonics*, vol. 5, pp. 169–174, 2010.

[88] X. Jiao and S. Blair, "Optical antenna design for fluorescence enhancement in the ultraviolet," *Opt. Express*, vol. 20, pp. 29909–29922, 2012.

[89] L. Li, S. Fang Lim, A. A. Puretzky, R. Riehn, and H. D. Hallen, "Near-field enhanced ultraviolet resonance Raman spectroscopy using aluminum bow-tie nano-antenna," *Appl. Phys. Lett.*, vol. 101, pp. 1–5, 2012.

[90] P. M. Schwab, C. Moosmann, M. D. Wissert, E. W. G. Schmidt, K. S. Ilin, M. Siegel, U. Lemmer, and H.-J. Eisler, "Linear and nonlinear optical characterization of sluminum nanoantennas," *Nano Lett.*, vol. 13, pp. 1535–1540, 2013.

[91] D. O. Sigle, E. Perkins, J. J. Baumberg, and S. Mahajan, "Reproducible Deep-UV SERRS on sluminum nanovoids," *J. Phys. Chem. Lett.*, vol. 4, pp. 1449–1452, 2013.

[92] G. Maidecchi, G. Gonella, R. Proietti Zaccaria, R. Moroni, L. Anghinolfi, A. Giglia, S. Nannarone, L. Mattera, H.-L. Dai, M. Canepa, and F. Bisio, "Deep ultraviolet plasmon resonance in aluminum nanoparticle arrays," *ACS Nano*, vol. 7, pp. 5834–5841, 2013.

[93] M. W. Knight, L. Liu, Y. Wang, L. Brown, S. Mukherjee, N. S. King, H. O. Everitt, P. Nordlander, and N. J. Halas, "Aluminum plasmonic nanoantennas," *Nano Lett.*, vol. 12, pp. 6000– 6004, 2012.

[94] L. Zhou, Q. Gan, F. J. Bartoli, and V. Dierolf, "Direct near-field optical imaging of UV bowtie nanoantennas," *Opt. Express*, vol. 17, pp. 20301–20306, 2009.

[95] P. Ghenuche, S. Cherukulappurath, T. H. Taminiau, N. F. van Hulst, and R. Quidant, "Spectroscopic mode mapping of resonant plasmon nanoantennas," *Phys. Rev. Lett.*, vol. 101, pp. 1–4, 2008.

[96] J. M. McMahon, G. C. Schatz, and S. K. Gray, "Plasmonics in the ultraviolet with the poor metals Al, Ga, In, Sn, Tl, Pb, and Bi," *Phys. Chem.*, vol. 15, pp. 5415–5423, 2013.

[97] K. Aslan, M. J. R. Previte, Y. Zhang, and C. D. Geddes, "Surface plasmon coupled fluorescencein the ultraviolet and visible spectral regions using Zinc thin films," Anal. Chem., vol. 80, pp. 7304–7312, 2008.

[98] M. G. Blaber, M. D. Arnold, and M. J. Ford, "A review of the optical properties of alloys and intermetallics for plasmonics," *J. Phys.: Condens. Matter*, vol. 22, pp. 1–15, 2010.

[99] P. C. Wu, T.-H. Kim, A. Suvorova, M. Giangregorio, M. Saunders, G. Bruno, A. S. Brown, and M. Losurdo, "GaMg alloy nanoparticles for broadly tunable plasmonics," *Small*, vol. 7, pp. 751–756, 2011.

[100] N. Akbay, F. Mahdavi, J. R. Lakowicz, and K. Ray, "Metal-enhanced intrinsic fluorescence of nucleic acids using platinum nanostructured substrates," *Chem. Phys. Lett.*, vol. 548, pp. 45–50, 2012.

[101] K. Appusamy, S. Blair, A. Nahata, and S. Guruswamy, "Low-loss magnesium films for plasmonics," *Mater. Sci. Eng. B*, vol. 181, pp. 77–85, 2014.

[102] FDTD Solutions Simulation Software, "Nanoparticle Scattering," https://www.lumerical.com/tcad-products/fdtd/applications/fdtd_nanoparticle_plasmon_cross_section.html.

[103] M. W. Knight, N. S. King, L. Liu, H. O. Everitt, P. Nordlander, and N. J. Halas, "Aluminum for plasmonics," *ACS Nano*, vol. 8, pp. 834–840, 2013.

[104] N. Cabrera and N. F. Mott, "Theory of the oxidation of metals," *Rep. Prog. Phys.*, vol. 12, pp. 163–184, 1949.

[105] T. Do and N. S. McIntyre, "Pressure effects on aluminium oxidation kinetics using X-ray photo-electron spectroscopy and parallel factor analysis," *Surf. Sci.*, vol. 440, pp. 438–450, 1999.

[106] H. Piao, M. Suominen Fuller, D. Miller, and N. S. McIntyre, "A study of thin film Au–Al alloy oxidation in ambient air by X-ray photoelectron spectroscopy (XPS), X-ray absorption near edge structure (XANES), and secondary ion mass spectrometry (SIMS)," *Appl. Surf. Sci.*, vol. 187, pp. 266–274, 2002.

[107] M. J. Meziani, C. E. Bunker, F. Lu, H. Li, W. Wang, E. A. Guliants, R. A. Quinn, and Y.-P. Sun, "Formation and properties of stabilized aluminum nanoparticles," *ACS Appl. Mater. Interfaces*, vol. 1, pp. 703–709, 2009.

[108] S. W. Chung, E. A. Guliants, C. E. Bunker, D. W. Hammerstroem, Y. Deng, M. A. Burgers, P. A. Jelliss, and S. W. Buckner, "Capping and passivation of aluminum nanoparticles using Alkyl-substituted epoxides," *Langmuir Lett.*, vol. 25, pp. 8883–8887, 2009.

[109] H. M. Lee and J.-Y. Yun, "Preparation of aluminum-oleic acid nano-composite for application to electrode for Si solar cells," *Mater. Trans.*, vol. 52, pp. 1222–1227, 2011.

[110] J. M. Sanz, D. Ortiz, R. Alcaraz de la Osa, J. M. Saiz, F. González, A. S. Brown, M. Losurdo, H. O. Everitt, and F. Moreno, "UV plasmonic behavior of various metal nanoparticles in the near- and far-field regimes: Geometry and Substrate Effects," *J. Phys. Chem. C*, vol. 117, pp. 19606–19615, 2013.

[111] M. H. Chowdhury, K. Ray, S. K. Gray, J. Pond, and J. R. Lakowicz, "Aluminum nanoparticles as substrates for metal-enhanced fluorescence in the ultraviolet for the label-free detection of biomolecules," *Anal. Chem.*, vol. 81, pp. 1397–1403, 2009.

[112] S. K. Jha, Z. Ahmed, M. Agio, Y. Ekinci, and J. F. Löffler, "Deep-UV surface-enhanced resonance raman scattering of adenine on aluminum nanoparticle arrays," *J. Am. Chem. Soc.*, vol. 134, pp. 1966–1969, 2012.

[113] M. H. Chowdhury, S. Chakraborty, J. R. Lakowicz, and K. Ray, "Feasibility of using bimetallic plasmonic nanostructures to enhance the intrinsic emission of biomolecules," *J. Phys. Chem. C*, vol. 115, pp. 16879–16891, 2011.